



ELSEVIER

Contents lists available at ScienceDirect

## Progress in Materials Science

journal homepage: [www.elsevier.com/locate/pmatsci](http://www.elsevier.com/locate/pmatsci)

CrossMark

# Dynamic and post-dynamic recrystallization under hot, cold and severe plastic deformation conditions

Taku Sakai<sup>a</sup>, Andrey Belyakov<sup>b,\*</sup>, Rustam Kaibyshev<sup>b</sup>, Hiromi Miura<sup>a</sup>, John J. Jonas<sup>c</sup>

<sup>a</sup> UEC Tokyo (The University of Electro-Communications), Chofu, Tokyo 182-8585, Japan

<sup>b</sup> Belgorod State University, Pobeda 85, Belgorod 308015, Russia

<sup>c</sup> McGill University, 3610 University Street, Montreal H3A 2B2, Canada

## ARTICLE INFO

### Article history:

Received 8 February 2013

Received in revised form 14 September 2013

Accepted 23 September 2013

Available online 1 October 2013

## ABSTRACT

The evolution of the new microstructures produced by two types of dynamic recrystallization is reviewed, including those brought about by severe plastic deformation (SPD). The microstructural changes taking place under these conditions and the associated mechanical behaviors are described. During the conventional discontinuous dynamic recrystallization (dDRX) that takes place at elevated temperatures, the new grains evolve by nucleation and growth in materials with low to medium stacking fault energies (SFE). On the other hand, new ultrafine grains can be produced in any material irrespective of the SFE by means of SPD at relatively low temperatures. These result from the gradual transformation of the dislocation sub-boundaries produced at low strains into ultrafine grains with high angle boundaries at large strains. This process, termed *in situ* or continuous dynamic recrystallization (cDRX), is still not perfectly understood. This is because many SPD methods provide data concerning the microstructural changes that take place but little information regarding the flow stress

**Abbreviations:** ARB, accumulative roll bonding; cDRX, continuous dynamic recrystallization; cSRX, continuous static recrystallization; EBSD, electron backscatter diffraction; ECAP, equal channel angular pressing; dDRX, discontinuous dynamic recrystallization; dSRX, discontinuous static recrystallization; DRV, dynamic recovery; DRX, dynamic recrystallization; DT, dynamic transformation; GBS, grain boundary sliding; HAB, high angle boundary; HPT, high pressure torsion; LAB, low angle boundary; MDF, multi-directional forging; mDRX, metadynamic recrystallization; MFS, mean flow stress; MSB, microshear band; OIM, orientation imaging microscopy; pDRX, post-dynamic recrystallization; RGS, relative grain size; SEM, scanning electron microscopy; SFE, stacking fault energy; SPD, severe plastic deformation; SRV, static recovery; SRX, static recrystallization; TEM, transmission electron microscopy; UFG, ultrafine grain.

\* Corresponding author. Tel.: +7 4722 585457; fax: +7 4722 585417.

E-mail address: [belyakov@bsu.edu.ru](mailto:belyakov@bsu.edu.ru) (A. Belyakov).

behavior. By contrast, multi-directional forging (MDF) provides both types of data concurrently. Recent studies of the deformation behavior of metals and alloys under SPD conditions, carried out using MDF as well as other SPD methods, are synthesized and the links between the microstructural and mechanical observations are examined carefully. Some models for grain formation under SPD conditions are discussed. Next, the post-dynamic recrystallization behavior, i.e. that of annealing after both dDRX and cDRX, is described. The differing annealing behaviors result from the differences in the natures of the deformed microstructures. Finally, an integrated recrystallization model for these phenomena, i.e. dynamic and static recrystallization of both the continuous and discontinuous types, is presented and discussed.

© 2013 Elsevier Ltd. All rights reserved.

## Contents

1.	Introduction	132
2.	Phenomenology of dynamic recrystallization	132
2.1.	Outline and terminology	132
2.2.	Flow stress behavior under hot working conditions	135
2.3.	Effect of structural factors and deformation conditions	136
3.	Conventional dynamic recrystallization	137
3.1.	Typical dynamic recrystallization flow curves	137
3.2.	The role of grain boundary bulging/sliding in nucleation of new dDRX grains	138
3.3.	Dislocation substructures in dDRX grains	141
3.4.	dDRX models	142
3.5.	Application to industry	146
3.5.1.	Rolling simulations	146
3.5.2.	Kinetics of dDRX and mDRX	149
3.5.3.	Effects of dDRX on ductility and texture	151
3.6.	Detection of the dDRX critical strain	151
3.6.1.	Dynamic transformation	152
4.	Continuous dynamic recrystallization and severe plastic deformation	153
4.1.	General characteristics of flow behavior and microstructures developed	153
4.1.1.	Historical development of severe plastic deformation	153
4.1.2.	Microstructural characteristics developed under SPD conditions	155
4.2.	Ultrafine grain microstructure development under SPD conditions	156
4.2.1.	Multi-directional forging	156
4.2.2.	UFG formation in low SFE materials	157
4.2.3.	UFG formation in high SFE materials	162
4.3.	Mechanisms of strain-induced UFG formation during SPD	169
4.3.1.	Models of strain-induced UFG formation	169
4.3.2.	A new model for the strain-induced formation of UFGs	173
4.4.	Effect of temperature and strain rate on the formation of strain-induced UFGs	175
4.4.1.	Low SFE materials	175
4.4.2.	High SFE materials	176
4.4.3.	Transient deformation behavior during changes in strain rate	179
4.5.	Mechanical properties of strain-induced UFG materials	179
5.	Post-dynamic recrystallization – Annealing behavior after dynamic recrystallization	183
5.1.	Post-cDRX	183
5.2.	Post-dDRX	188
5.3.	Concluding remarks	193
6.	Summary of dynamic and post-dynamic recrystallization	194
6.1.	Dynamic recrystallization	194
6.2.	Post – dynamic recrystallization	195

6.3. Concluding remarks .....	197
6.4. Topics for further investigation .....	198
Acknowledgements .....	198
References .....	199

---

## 1. Introduction

The control of microstructure as well as of grain refinement through thermomechanical processing has been developed extensively since around 1970 and has been recognized as being both of technical importance as well as of scientific interest. The most developed method of grain refinement is based on plastic deformation at ambient temperatures followed by annealing at elevated temperatures [1–5]. Another commonly employed approach involves the production of new grains directly during hot working by the process of dynamic recrystallization [3–5]. In both cases, the new microstructures result from the production of recrystallization nuclei, followed by the long-range migration of their boundaries. These processes occur in two steps and so are generally referred to as being discontinuous [4,5].

Over the past two decades, another method of new grain formation has been studied extensively; this takes place under conditions of severe plastic deformation. In this case, the ultrafine grained structures are developed at relatively low temperatures. This is one of the most promising topics in material science because it could lead to the production of submicron to nanometer sized crystallites in a wide variety of structural metals and alloys [4,5]. The mechanisms that produce grain refinement under these conditions, however, have not been as comprehensively studied as those of hot deformation. One of the limitations associated with the large strain methods is that data concerning the microstructural changes are readily obtained, whereas only limited data have been generated regarding the flow stress behavior under these conditions. This does not apply to multi-directional forging, which provides both types of data. The ultrafine grains formed in this way are considered to be produced in a single step and to develop uniformly over the entire volume. This mechanism of grain refinement is therefore referred to as *in situ* or continuous dynamic recrystallization (cDRX) [4,5] and is only imperfectly understood.

The purpose of this review is to synthesize the recent work on all these types of grain refinement process. Some operate under hot and others under cold working conditions. The links between the microstructural and mechanical observations that have been gathered will be considered carefully. The high temperature processes are covered in Section 3, which includes a discussion of the application of these phenomena to industry. The cold deformation processes are treated in Section 4. Particular attention is paid in this section to the data obtained by multi-directional forging because this procedure provides both microstructural and mechanical information regarding the grain refinement process. In Section 5, the annealing behaviors of the as-deformed materials produced at both elevated and ambient temperatures are considered and interpreted in terms of the natures of the deformed microstructures. Finally, in Section 6, an integrated recrystallization model of these phenomena is presented, which involves both the dynamic and static processes and in which both continuous and discontinuous reactions are covered.

## 2. Phenomenology of dynamic recrystallization

### 2.1. Outline and terminology

The term recrystallization is commonly used to describe the replacement of a deformation microstructure by new grains during annealing; this is referred to as static recrystallization (SRX) [1–5]. One of the most studied and widely used recrystallization processes is primary recrystallization, during which new grains are produced by the nucleation and growth of new grains (see Fig. 1). Static recovery (SRV) takes place during the early stages of annealing and is responsible for the development of

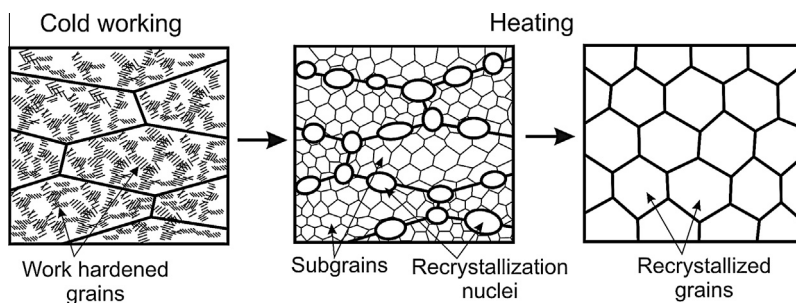


**Fig. 1.** Schematic representation of the discontinuous static recrystallization (dSRX) taking place during the annealing of strain hardened materials.

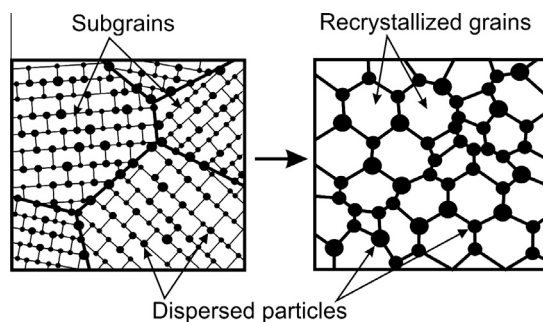


**Fig. 2.** Schematic representation of the continuous static recrystallization (cSRX) controlled by particle coarsening (after Hornbogen et al. [8,9]).

recrystallization nuclei as fine dislocation-free crystallites. These grow by means of the long-range migration of the boundaries, which consume the strain hardened microstructure [1–6]. The driving pressure for the growth of such new grains is the stored energy associated with the dislocations and sub-boundaries produced during prior straining. In the early stages of SRX, the nuclei are outlined by low-angle boundaries, the misorientations of which gradually increase until they attain values typical of high-angle boundaries (HABs) [4,5,7]. During annealing, the microstructure is characterized by a mixture of increasing amounts of recrystallized grains and decreasing amounts of strain hardened grains. Such a process is sometimes referred to as discontinuous static recrystallization (dSRX) [3–5].

In some strain hardened aluminum alloys containing dispersoids, on the other hand, the new microstructure develops homogeneously throughout the entire volume [8,9]. These new grains are the result of gradual subgrain growth accompanied by particle coarsening, as shown in Fig. 2. Concurrently the sub-boundary misorientations  $\theta$  increase progressively until all the low-angle boundaries (LABs) are transformed into HABs. This process is characterized by a microstructure that remains homogeneous throughout and is therefore referred to as *in situ* or continuous static recrystallization (cSRX) [4,5,8,9].

SRX takes place when strain hardened metals are heated above approximately half the melting point (in Kelvin), i.e.  $0.5T_m$ ; the temperature at which this can be accomplished in one hour is generally referred to as the recrystallization temperature  $T_{REX}$ . The latter depends on material factors such as the type of lattice, concentration of alloying elements, and size distribution of second phases [1–5,10]. By contrast, conventional dynamic recrystallization (i.e. dDRX) takes place *during* straining, as long as the temperature is above about  $0.5T_m$  [11–16]. The new grains appear at the nucleation strain and then replace the initial microstructure completely at high strains. As in the case of SRX, there is a gradual transformation of the subgrains formed mainly in the vicinity of the grain boundaries into nuclei delineated by HABs. These dynamic processes, which involve a nucleation stage, are analogous to

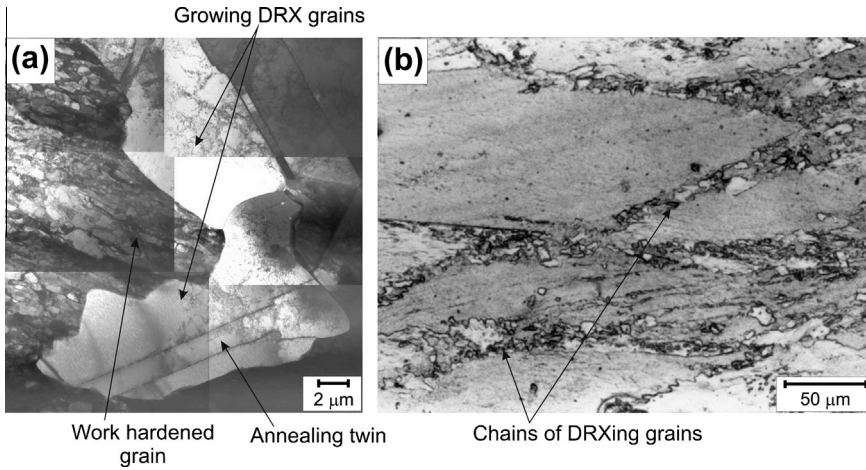


**Fig. 3.** Discontinuous dynamic recrystallization in pure Cu showing (a) growing grains during deformation at 623 K and (b) the necklace-like microstructure appearing during compression at 573 K [25].

those taking place during dSRX and are sometimes referred to as discontinuous dynamic recrystallization (dDRX) [4,5].

It has been recognized that the dynamic mechanism differs considerably from that operating during static recrystallization. The latter leads to the evolution of a uniform and dislocation-free grain structure after full annealing (see Fig. 1). High temperature plastic deformation, which promotes the bulging of corrugated grain boundaries, is described in more detail in Section 3. As a result, dDRX grains initially have wavy boundaries and contain dislocation substructures that vary from grain to grain [13–20]. Even after dDRX is fully developed, i.e. during steady state flow, regions containing substructures continue to be present, in sharp contrast to the materials that have undergone dSRX. A typical substructure developed during dDRX is shown in Fig. 3a, and the necklaces of new grains that form along the boundaries in Fig. 3b. The dynamic grain size produced depends sensitively on the deformation conditions [21–25].

The mechanism of cDRX, on the other hand, is quite different. Here, the new grains form as a result of the increase in sub-boundary misorientation brought about by continuous accumulation of the dislocations introduced by the deformation [25–36]. The formation of cDRX grains in an aluminum alloy during hot working is illustrated in Fig. 4 [37]. The changes in the microstructure are associated with

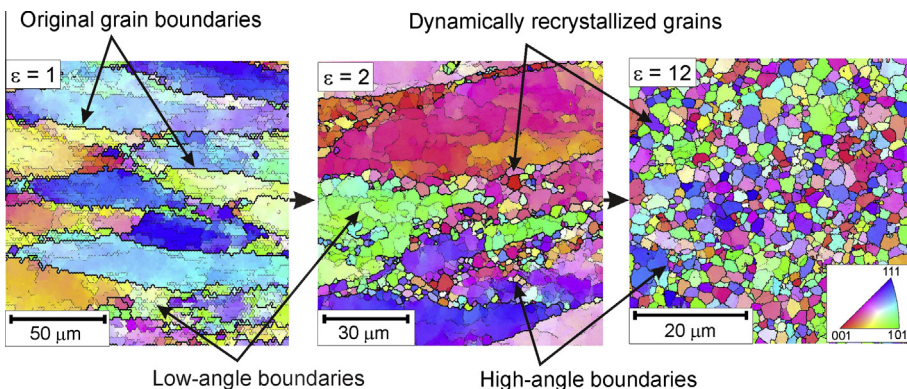


**Fig. 4.** Development of new grains due to continuous dynamic recrystallization (cDRX) observed by OIM. The AA1421 aluminum alloy was processed by ECAP repeatedly to a strain of 12 at 673 K [37].

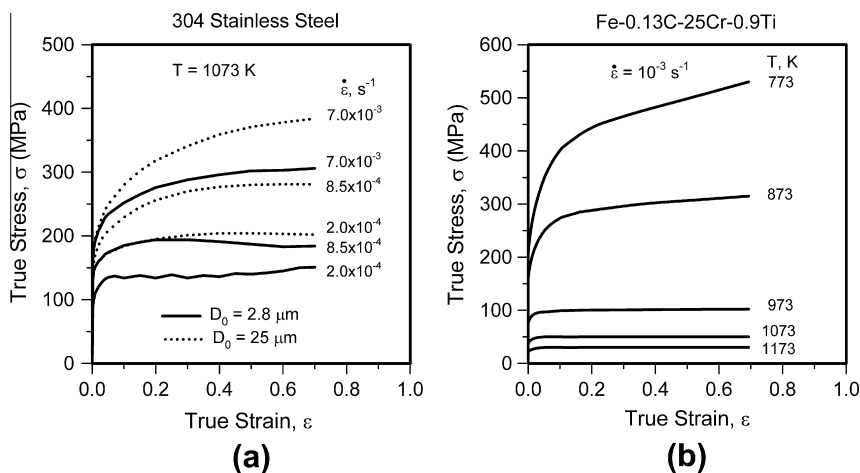


Fig. 5. Typical stress–strain curves obtained during the hot compression of steels accompanied by (a) discontinuous dynamic recrystallization (dDRX) in austenite [39] and (b) dynamic recovery (DRV) in ferrite [38].

the continuous formation of HABs due to the accumulation of dislocations. The fraction of such boundaries gradually increases during straining, until almost all the grains are bounded by HABs at  $\epsilon = 12$  for example.

It should be noted that cDRX is characterized by much slower kinetics than those associated with DRX. This is because the formation of a cDRX microstructure requires remarkably large strains (e.g.  $\epsilon = 12$ ). By contrast, those produced by dDRX are propagated an order of magnitude more quickly (e.g.  $\epsilon \approx 1$ ) [25–27,29,33,37]. Curiously, cDRX may also produce a necklace microstructure at an intermediate stage, see Fig. 4. This is because of the rapid development of strain gradients near grain boundaries. The latter lead to the presence of large misorientations in the vicinities of the boundaries. Finally, it should be noted that, depending on the material and processing conditions, different mechanisms of grain evolution can operate during SPD, as will be clarified in Section 4.

## 2.2. Flow stress behavior under hot working conditions

Two types of deformation behavior, resulting from dDRX and DRV, have been displayed by numerous metallic materials under hot working conditions, as can be seen in Fig. 5 [38,39]. In the case of dDRX, new grains appear during straining. The new grains produce softening, decreasing the work hardening rate until eventually there is a clear stress peak. The flow stress then decreases with increasing strain until the level associated with steady state deformation is attained (Fig. 5a). The steady state flow stress reflects the dynamic equilibrium between strain hardening and strain softening due to the formation of new grains and the associated grain boundary migration. In some cases, several peaks of decreasing heights can be seen before the steady state behavior is achieved. Further details of the structural changes taking place during dDRX will be described in Section 3.

The second type of high temperature behavior is characterized by a continuous increase in flow stresses during plastic working, during which the rate of strain hardening gradually decreases with deformation and approaches zero at high strains, leading to a steady state of flow (Fig. 5b). Such behavior is attributed to the operation of DRV as the main restoration process [4,12,13]. In this case, steady state flow is attained when the rate of DRV has increased sufficiently to balance the rate of strain hardening. Such recovery-controlled steady state flow is generally observed at modest strains ( $\epsilon < 1$ ) during hot deformation at relatively low strain rates.

Still a third kind of behavior is displayed during SPD experiments. Recent studies of the microstructural evolution under these conditions have shown that the substructures developed by DRV during the early stages of straining progressively change their natures, not only at high temperatures, but also

**Table 1**

The dynamic restoration process (dDRX and DRV) operating during hot deformation and the metallic materials in which they have been observed (state of understanding around 1980) [13,15,20].

Restoration mechanism	Materials	Stacking fault energy (SFE)
Dynamic recrystallization (dDRX)	Au, Cu, Ni, Pb, austenitic Fe, and their alloys	Low (to medium)
Dynamic recovery (DRV)	Al, Mg, ferritic iron, and their alloys	High

**Table 2**

Ranges of operation of dDRX and cDRX during plastic deformation to very large strains [4,25,30].

Processing conditions ( $T/T_m$ )	Stacking fault energy (SFE) of material	
	Low to medium	High
Hot working ( $T > 0.5T_m$ )	dDRX	cDRX
Warm/cold deformation ( $T < 0.5T_m$ )	cDRX	cDRX

at ambient temperatures [25,29,32,33,36,37]. In this case, the subgrain misorientations gradually increase until they attain HAB values at all homologous temperatures  $T/T_m$  from 0 to 1. This type of process is referred to as cDRX and will be considered in Section 4 in detail.

### 2.3. Effect of structural factors and deformation conditions

The occurrence of dDRX on the one hand or cDRX on the other depends on the relation between the rate of DRV and the migration velocity (mobility) of the grain boundaries. dDRX generally takes place during the hot working of metals and alloys of low to medium stacking fault energy (SFE); these exhibit relatively low rates of DRV. The relationship between dDRX and DRV during hot deformation for representative metallic materials as it was understood around 1980 is summarized in Table 1 [13,15,20]. The fcc metals that undergo dDRX here are Ag, Au, Cu, Ni, Pb, Pt, and the austenitic steels [11–20]. The critical strain for the operation of dDRX decreases with temperature increase and with decrease in strain rate as well as with decrease in the grain size [12–15,18–21,39,40]. On the other hand, the precipitation of second phase particles has the opposite effect on dDRX. When the pinning force due to the particles exceeds the driving force for boundary bulging, dDRX is suppressed and finer dDRX grains are formed at larger strains, if at all [41–43].

High SFE materials, in which DRV takes place with ease, are characterized, on the other hand, by the continuous transformation of subgrains into ultrafine grains; however, this requires the application of very large strains [29–33,36–38]. This takes place during SPD in metals such as Al,  $\beta$ -Ti, and ferritic steels. Enhanced dynamic recovery generally suppresses dDRX in high SFE materials, as the deformation substructures produced are characterized by rather low dislocation densities and therefore low driving forces for dDRX. Exceptionally, dDRX-like behavior has been reported in such materials, but only in extra-high purity  $\alpha$ -iron and aluminum [44,45]. At sufficiently large strains, which can only be applied by SPD, new fine grained structures form instead by the gradual transformation of subgrains with LABs into UFGs with HABs. This is the process that is referred to as cDRX [46–48].

During cDRX, geometrically necessary boundaries develop, which are gradually transformed into HABs [49]. The former separate microvolumes in which different combinations of slip systems are operating. As a result of the continuing deformation, these microcrystallites increase their misorientations and are gradually transformed into grains bounded by HABs. This process is observed during warm/cold SPD of both low and high SFE materials [25,46–48,50–53]. Also, cDRX takes place during SPD of high SFE materials at any value of  $T/T_m$  from 0 to 1, as shown in Table 2 [4,25,30]. In two-phase materials, the development of HABs takes place more rapidly than in single phase materials. This leads to significant refinement of the original microstructure, as has frequently been observed [54–58]. When SPD is carried out at cold and warm temperatures, strain localization occurs on a microscale and leads to the formation of microshear bands or MSBs. These play important roles in the development of UFG microstructures at large strains and their contributions will be discussed in Section 4 in detail.

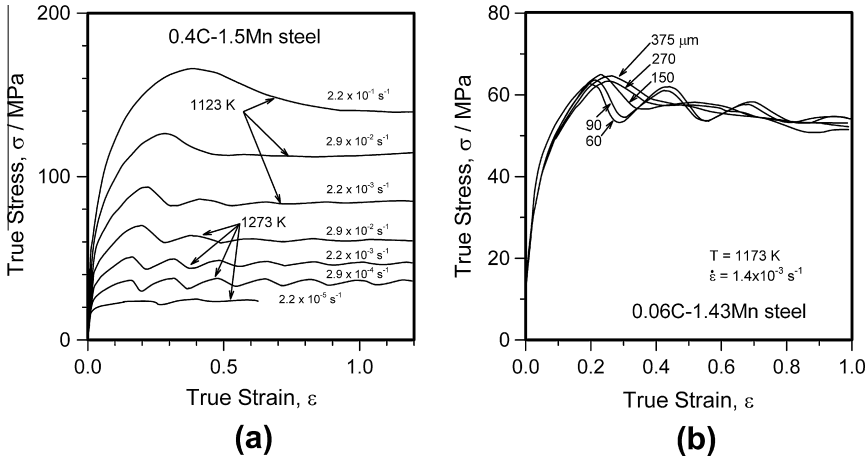


**Fig. 6.** Typical stress–strain curves characteristic of dDRX in the austenite of plain carbon steels [20]. (a) A 0.4C–1.5% Mn steel compressed at 1123 K and 1273 K at true strain rates between  $10^{-5}$  and  $10^{-1} \text{ s}^{-1}$ . (b) A 0.06C–1.42% Mn steel with initial grain sizes of 60–375  $\mu\text{m}$  compressed at 1173 K and  $1.4 \times 10^{-3} \text{ s}^{-1}$ .

### 3. Conventional dynamic recrystallization

#### 3.1. Typical dynamic recrystallization flow curves

In materials subject to dDRX and at temperatures above  $0.5T_m$ , the strain hardening produced by deformation is counteracted by this mechanism. It gradually reduces the work hardening rate until a flow stress maximum is reached after which there is strain softening (see Figs. 5 and 6). In these materials (see Table 1), the dislocation density increases to a high level and eventually some of the local differences in density reach a high enough level to permit the nucleation of new grains. This is followed by the long-range migration of HABs. As distinct nucleation and growth stages are induced, conventional dDRX is considered to be a two-step process.

In high SFE materials, by contrast, the rearrangement and annihilation of dislocations take place with ease, generally leading to the formation of equiaxed subgrains. Nevertheless, it has been shown recently that, even when only DRV is operating, new grain structures can be formed if very large strains are applied, for example by SPD processes [4,5,25,30]. The deformation microstructures appearing under the latter conditions differ appreciably from those produced by dDRX, as does the flow behavior. The DRV mechanisms operating under SPD conditions will be considered later and separately in Section 4.

The flow curves appearing under dDRX conditions exhibit the characteristic shapes shown in Fig. 6. The form of the curve changes from the multiple peak to the single peak type as the temperature  $T$  is decreased or the strain rate  $\dot{\epsilon}$  is increased, i.e. as the temperature compensated strain rate or the Zener–Hollomon parameter  $Z$  expressed by Eq. (1) is increased [11–15,20],

$$Z = \dot{\epsilon} \exp(Q/RT) \quad (1)$$

Here  $R$  is the gas constant (8.317 kJ/mole K) and the apparent activation energy for deformation  $Q$  is an experimental constant [4,11–20]. It generally takes values somewhat above those for self-diffusion, indicating that deformation under dDRX conditions is thermally activated and involves self-diffusion [12,13].

Under dDRX conditions, the shape of the flow curve is also sensitively affected by the initial grain size. Fig. 6b illustrates a series of flow curves in the austenite of a plain carbon steel hot compressed at 1173 K [20]. The flow curve shapes change from the multiple peak to the single peak form as the initial grain size  $D_0$  is increased. In other words, multiple stress peaks appear when the initial microstructure

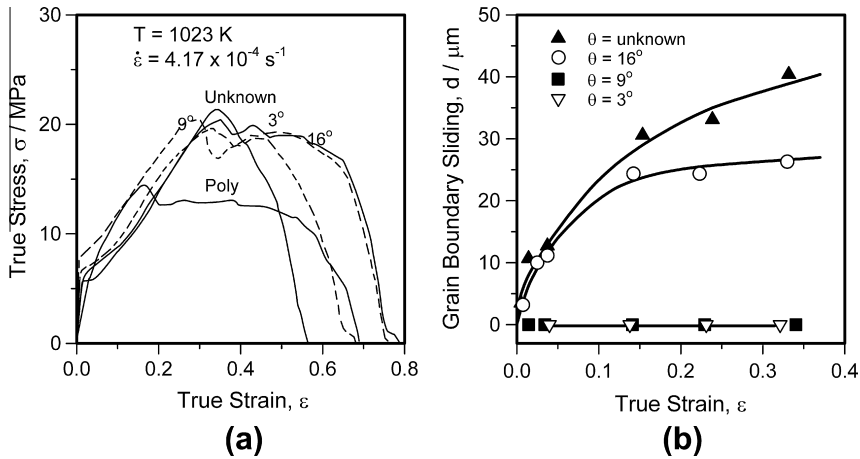


**Fig. 7.** Effect of grain boundary character on dDRX in copper bicrystals with differently misoriented [001] twist boundaries deformed in tension at 1023 K [59]. (a) True stress–true strain curves of the bicrystals and a polycrystal. (b) Relationship between grain-boundary sliding and tensile strain.

is fine grained; in this case, grain coarsening takes place until the stable grain size  $D_s$  is attained. By contrast, the single peak type of flow is associated with grain refinement in coarse grained starting materials. Thus whether the flow curve is of the multiple or single peak type is determined by the ratio  $D_o/D_s$  of the initial to the final grain size and does not depend solely on the value of  $Z$ , Eq. (1). These phenomena are discussed in more detail in Section 3.3.

### 3.2. The role of grain boundary bulging/sliding in nucleation of new dDRX grains

Miura et al. [59,60] have carried out a systematic study of the effect of grain boundary character on dDRX using copper bicrystals. This has provided a fundamental understanding of the nucleation processes taking place during dDRX. Some typical flow curves for Cu–0.4% Si

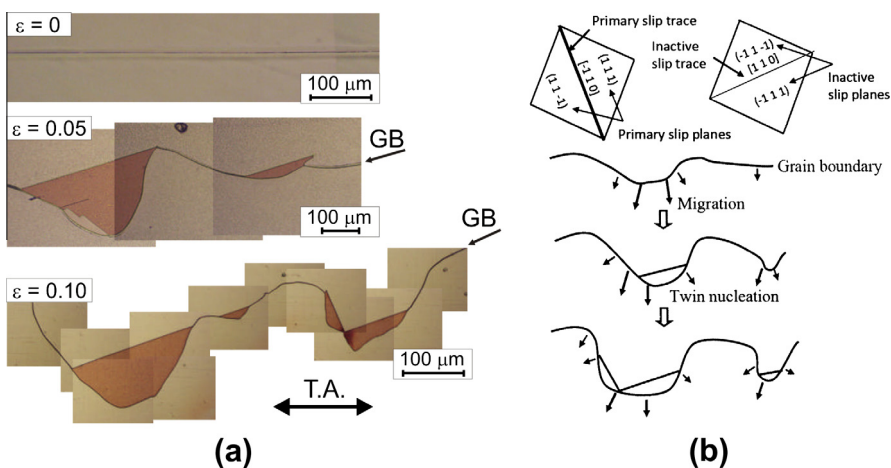


**Fig. 8.** (a) Dynamically nucleated grains at a  $64^\circ$  tilt boundary in copper bicrystals after deformation at 923 K and  $4.2 \times 10^{-4} \text{ s}^{-1}$  [60]. T.A. is the tensile axis. (b) Schematic illustration of the twin variant selection caused by grain boundary migration. The tetrahedron at the top identifies the orientations of the active and inactive slip traces of the upper grain.

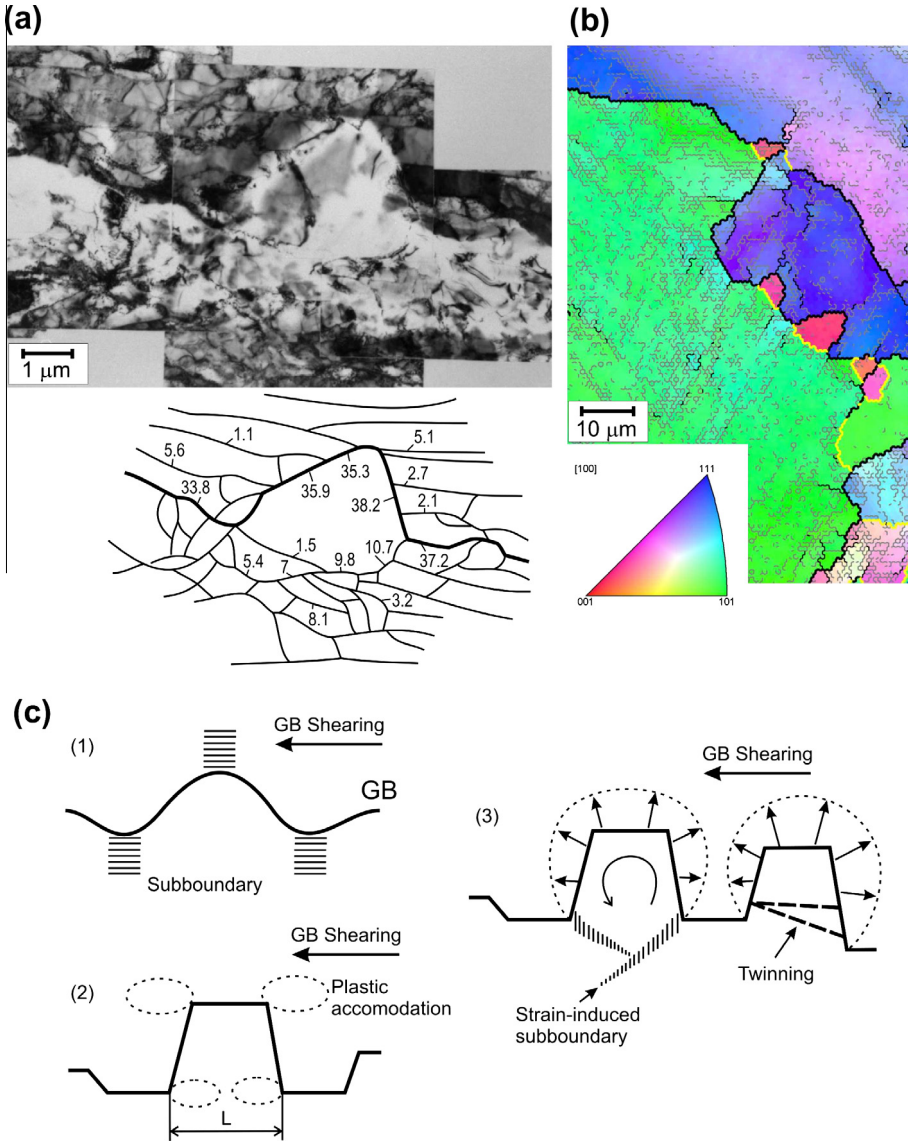


**Fig. 9.** Examples of dDRX grains nucleated at grain boundaries in polycrystalline copper compressed at  $10^{-3} \text{ s}^{-1}$  to (a)  $\varepsilon = 1.3$  at 573 K (i.e. a high Z) and (b)  $\varepsilon = 0.2$  at 723 K (i.e. a low Z) [61,62]. HABs with misorientations greater than  $15^\circ$  are delineated by thick black lines, LABs with misorientations in the range  $4\text{--}15^\circ$  by thin black lines and in the range  $2\text{--}4^\circ$  by thin grey lines. Twin boundaries are marked in yellow. The colors in the OIM micrographs correspond to the crystallographic orientations indicated in the inverse pole figure. (c) Schematic representation of the process of new grain formation during dDRX; here (1) boundary corrugation is accompanied by the evolution of dislocation sub-boundaries at low strains, (2) some grain boundary sliding is taking place, leading to the development of local strain gradients during further straining, and (3) the bulging out of parts of the serrated grain boundaries is accompanied by the formation of sub-boundaries at high Z or twin boundaries at low Z [59,61–63].

bicrystals, deformed in tension at 1023 K and  $4 \times 10^{-4} \text{ s}^{-1}$ , are reproduced here in Fig. 7. The bicrystal boundaries were initially inclined at  $45^\circ$  to the tensile axis; the boundary types investigated included [001] twist boundaries with misorientation angles of  $3^\circ$ ,  $9^\circ$ ,  $16^\circ$  and one that was unknown. The grain boundary character can be seen to affect the shape of the flow curve

as well as the overall behavior. The stress peak  $\sigma_p$  and the strain at which  $\sigma_p$  appears,  $\varepsilon_p$ , are considerably higher than those in polycrystals. This indicates that dDRX propagates more rapidly in polycrystals than in bicrystals.

It can be seen from Fig. 7b that grain boundary sliding (GBS) took place in the 16° and ‘unknown’ bicrystals, while it hardly played a role in the low misorientation specimens. It is of interest to note that, in the latter bicrystals, dDRX was initiated in the grain interiors far from the usual sites at the boundaries. By contrast, nucleation took place at  $\varepsilon \approx 0.15$  at serrated boundaries in the 16° and unknown bicrystals. In this case, the development of serrations prevented further GBS, resulting in the development of high strain gradients at the boundary. It should be added in passing that metal forming operations are generally carried out at strain rates many orders of magnitude higher than those of Fig. 7. For this reason, GBS or shearing does not play a role under these conditions and nucleation takes place entirely as a result of the transformation of the bulges into nuclei. Miura et al. [60] also investigated nucleation in bicrystals in which [001] tilt boundaries were aligned parallel to the tensile axis. Under these conditions, GBS cannot take place. It can be seen from Fig. 8 [60] that bulging followed by local boundary migration occurred and that this was accompanied by twinning. As a result, the new grains were twin-related ( $\Sigma 3$ ) to the matrix. Furthermore, as shown in Fig. 8b, the primary twin traces were parallel to some of the inactive slip planes in the parent grains, indicating that these were annealing twins.

We turn now to nucleation in polycrystalline materials, which have been more frequently investigated. Here, nucleation occurs as a result of the fluctuations in boundary shape produced by straining, which develop into the serrations that are the actual nucleation sites [12–20,61–63]. Some typical microstructures of grains undergoing nucleation at the grain boundaries are illustrated in Fig. 9. These experiments were carried out on polycrystalline copper that had been compressed at  $\dot{\varepsilon} \approx 10^{-3} \text{ s}^{-1}$  to (a)  $\varepsilon = 1.3$  at 573 K (i.e. at a high  $Z$ ) [61] and (b)  $\varepsilon = 0.2$  at 723 K (i.e. at a low  $Z$ ) [61,62]. It should be noted in Fig. 9a that boundary bulging took place accompanied by the formation of sub-boundaries. In this case the strain was 1.3 and so appreciable strain and orientation gradients had developed at the boundaries. During compression at a lower value of  $Z$ , by contrast, new grains had already appeared at the lower strain of 0.2. In this case, as in that of the bicrystals of Fig. 8, a  $\Sigma 3$  twin boundary can be seen, as indicated by the yellow line in Fig. 9b. The latter are frequently developed at higher temperatures because of the higher mobility of the grain boundaries.

Based on the observations described above, a nucleation model for dDRX can now be drawn up, as represented schematically in Fig. 9c [59–63]. First, dislocation density gradients are developed near the original grain boundaries because of the incompatibilities between grains. This is accompanied by subgrain formation, leading eventually to the development of boundary corrugations or serrations. At the lower strain rates, GBS can take place along the boundaries, leading to the development of additional inhomogeneous strains, further increasing the driving force for recrystallization. The condition for bulging to occur under dynamic conditions is expressed as follows [59]:

$$\Delta E > 4K_1\gamma_B/L \quad (2)$$

Here  $\Delta E$  is the strain energy difference per unit volume across the boundary,  $\gamma_B$  the grain boundary energy per unit surface area, and  $L$  the length of the boundary prior to bulging. The proportionality factor  $K_1$  is generally less than one under dDRX conditions. This is because the grain boundaries are always serrated before growth by bulging takes place. In the case of static recrystallization,  $K_1$  is usually one, as originally proposed by Bailey and Hirsch [6].

It is of interest that nucleation takes place at triple junctions at much lower strains than along the boundaries [64]. Even when GBS is occurring, it is impeded at triple junctions, again adding to the strain gradients. In the case of polycrystalline copper, for example, nucleation at a triple junction took place at the remarkably low strain of about 0.01, which is only 1/10 to 1/20 of the peak strain [64]. On further straining to 0.04, nuclei were observed to be present at about 10% of the triple junctions. Irrespective of the testing conditions, more than 80% of the grains nucleated at triple junctions were annealing twins in that investigation [64].

### 3.3. Dislocation substructures in dDRX grains

As in the case of ambient temperature deformation, the average cell size of high temperature dislocation substructures decreases during straining and the subgrain boundaries are sharpened. Finally, the nucleation of dDRX grains begins to take place at around  $0.5\varepsilon_p$  with the rate increasing to a maximum at around  $\varepsilon_p$ . At large strains, where dDRX has been propagated through the entire volume, the substructure density varies from grain to grain. Such microstructures can be subdivided into the three categories illustrated schematically on the upper half of Fig. 10 [17]. Here the dislocation density  $\rho_0$  is the initial fully annealed value,  $\rho_c$  is the critical value for nucleation, and  $D$  the local dynamic grain size;  $\rho_c$  and  $D$  depend sensitively on temperature and strain rate via  $Z$  in Eq. (1). The current state is represented by the solid lines and earlier states by the dashed lines. The three types of grain in this model correspond to; (a) a dDRX nucleus, (b) a growing dDRX grain containing a dislocation density gradient, and (c) a critically strain-hardened grain after impingement.

Some typical TEM micrographs of dynamic microstructures are represented in the lower half of Fig. 10. Here (d), (e) and (f) correspond to the respective grain types introduced above. In this case, nickel was deformed in tension at 1073 K and  $1.5 \times 10^{-1} \text{ s}^{-1}$  and hydrogen quenched [17]. In an actual

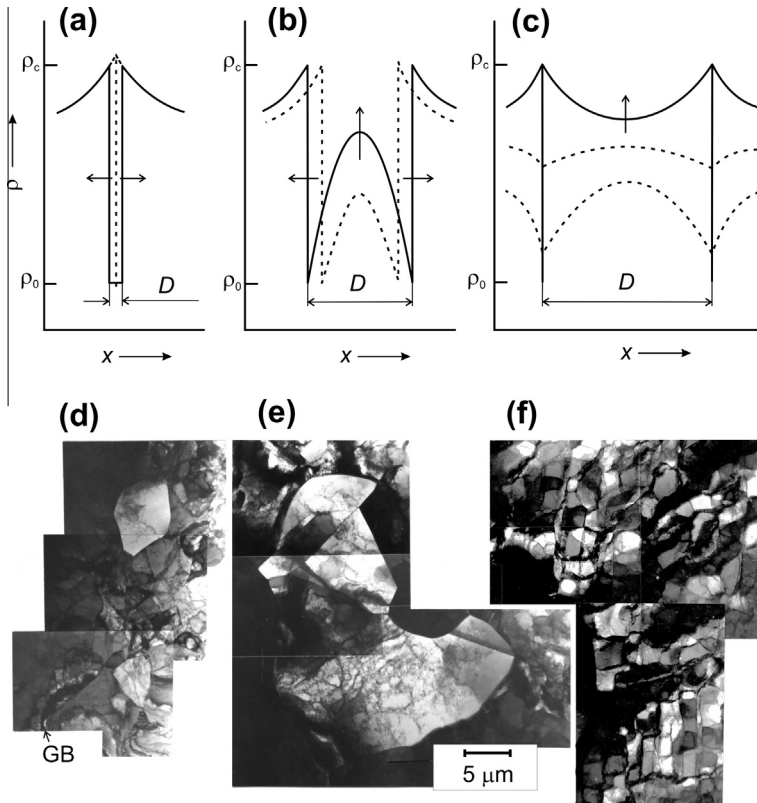


**Fig. 10.** Three types of dDRX grains and corresponding TEM micrographs [17]. Three types of dislocation density distribution develop in the microstructure: (a) a dDRX nucleus, (b) a growing dDRX grain, and (c) a critically strain hardened dDRX grain. Here  $\rho_0$  is the initial (annealed) dislocation density,  $\rho_c$  is the critical value required for dynamic nucleation, and  $D$  is the current dDRX grain size. The current state is represented by the full lines and one or more earlier states by broken lines. In the TEM micrographs at the bottom, the dislocation substructures identified as (d), (e) and (f) correspond to grains (a), (b) and (c), respectively. Here nickel was deformed in tension at 1073 K and  $1.5 \times 10^{-1} \text{ s}^{-1}$  and hydrogen quenched.

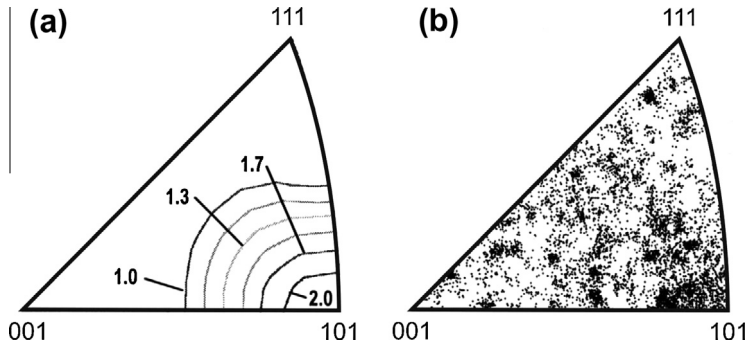


**Fig. 11.** Inverse pole figures of the deformation microtexture developed in pure Cu determined using EBSD. The sample was compressed to a strain of 1.3 at 723 K at a strain rate of  $10^{-1} \text{ s}^{-1}$  [62]. The contour plots are on the left (a) and the discrete plots on the right (b).

recrystallizing microstructure, regions belonging to each of these three types are distributed fairly uniformly throughout.

The heterogeneous microstructures formed during dDRX display an annealing behavior that differs from that pertaining to cold worked materials. This topic is treated separately in Section 5. Here the microtextures that develop during dDRX will be considered in terms of the microstructure model of Fig. 10. A sample of pure copper was compressed to a strain of 1.3 at 723 K and  $10^{-1} \text{ s}^{-1}$ . Under these conditions, a fully developed dDRX microstructure is generated [62]. Inverse pole figures (IPFs) were determined on the recrystallizing grains by the electron backscatter diffraction (EBSD) method; these are displayed in Fig. 11 in the form of both contour (Fig. 11a) and discrete (Fig. 11b) plots. Here the compression direction is shown. The  $\langle 101 \rangle$  fiber can be seen in the left hand IPF of Fig. 11a; this is the conventional deformation fiber developed during cold compression, although it is very weak. However, the right hand IPF of Fig. 11b indicates that randomly oriented grains are also present. These result from the orientation randomizing effects of dDRX. According to the model of Fig. 10, strain-hardened grains (c) of various orientations only exist stably for a limited period of time until the next cycle of dDRX begins. During compression, although they develop the required deformation texture, which is the  $\langle 101 \rangle$  fiber, many grains are rotated out of this orientation by dDRX, which acts to weaken the fiber. When the temperature is increased, dDRX takes place more rapidly, so that the intensity of the  $\langle 101 \rangle$  component decreases with increasing temperature [62,65].

### 3.4. dDRX models

Typical dDRX flow curves exhibit regular oscillations in stress at low values of  $Z$  or a single stress peak followed by strain softening at high  $Z$  values. At large strains, a steady state of flow is attained in both cases (Fig. 6). In the original descriptions of dDRX, much attention was paid to this changeover behavior [12–15,20,40]. For example, Luton and Sellars [40] took the view that the transition is associated with the different strain rate and temperature dependences of the peak strain  $\varepsilon_p$  on the one hand and the strain  $\varepsilon_x$  for the completion of flow softening after the flow stress peak has been attained, i.e. of the first cycle of dDRX, on the other. The critical condition for this “critical strain-based” model can be expressed as:

$$\varepsilon_p = \varepsilon_x \quad (3)$$

At low values of  $Z$ , when  $\varepsilon_p > \varepsilon_x$ , dDRX is cyclic; conversely at higher  $Z$  values, when  $\varepsilon_p < \varepsilon_x$ , dDRX operates continuously throughout the material.

Although the critical strain-based model is in reasonable agreement with the data obtained in solid bar torsion investigations, it does not apply to tension or compression results or even to torsion tests result carried out on tubular samples [20]. More recently, a more physically based model was

proposed linking the shape of the flow curve to the initial grain size [14,18,20]. One of the results obtained was illustrated in Fig. 6b above. Here it was shown that multiple stress peaks are observed when the initial grain size  $D_o$  is fine and conversely single peak curves are associated with the deformation of coarse grained material. Whether the flow curve is of the multiple or single peak type depends not only on the initial grain size, but is determined by the relative grain size ( $D_o/D_s$ ), where  $D_s$  is the stable dynamic grain size established at large strains. This leads to the “relative grain size (RGS)” condition for the transition, which is expressed by [20,66].

$$D_o = 2D_s \quad (4)$$

When  $D_o > 2D_s$ , grain refinement and single peak flow take place. Conversely, when  $D_o < 2D_s$ , multiple peak flow is accompanied by grain coarsening. As  $D_s$  is sensitively affected by  $Z$ ,  $D_o > 2D_s$  and single peak flow correspond to deformation under high  $Z$  conditions; conversely,  $D_o < 2D_s$  and cyclic flow correspond to lower  $Z$  conditions [12–15,20,66]. These two contrasting cases are closely related to the nature of dDRX and will be discussed in more detail below.

As outlined above, the changeover from multiple to single peak behavior occurs when  $D_o = 2D_s$ , so that the transition is also associated with a critical value of  $Z$ , labeled  $Z_c$ . In other words, there is a  $Z_c$  vs.  $D_o$  relation that approximately overlaps the  $Z$  vs.  $2D_s$  dependence. The similarity between the  $Z_c$ - $D_o$  and  $Z$ - $2D_s$  relations can be seen to better effect in Fig. 12, where the cross-hatching distinguishes the grain refinement from the grain coarsening region and the solid line represents the experimentally determined locus  $D_o = 2D_s$ . According to this diagram, three different types of tests can be carried out in the laboratory, which have been referred to as vertical (V), horizontal (H) and combined V/H experiments.

V tests are carried out with a fixed initial grain size  $D_o$  but at a series of different values of  $Z$ . These correspond to the classical experiments depicted in Fig. 6a. Testing carried out on samples with a range of initial grain sizes at a fixed value of  $Z$  (see Fig. 6b), correspond to the H tests illustrated in Fig. 12. The two types of behavior, i.e. multiple peak and grain coarsening or single peak and grain refinement, are readily represented on such diagrams. In Fig. 6b, a 0.06% C–1.43% Mn steel was austenitized at temperatures from 1173 to 1533 K selected to produce initial austenite grain sizes of 60–375  $\mu\text{m}$ , respectively, and then compressed to  $\varepsilon = 1.0$  at 1173 K and  $1.4 \times 10^{-3} \text{ s}^{-1}$ , for which  $2D_s \approx 150 \mu\text{m}$ . Cyclic  $\sigma/\varepsilon$  behavior was observed when  $D_o < 2D_s$ ; by contrast, single peak behavior was obtained when  $D_o > 2D_s$  [20].

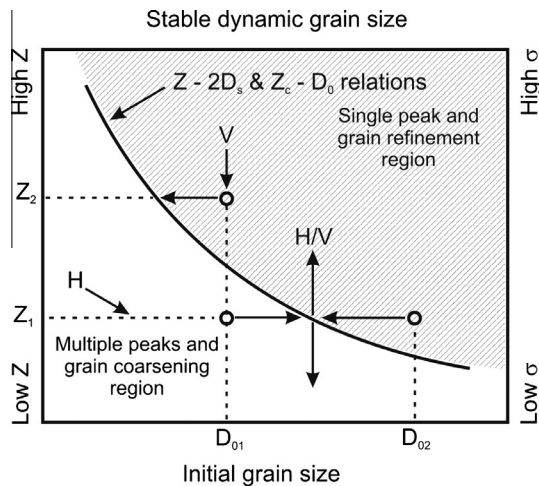
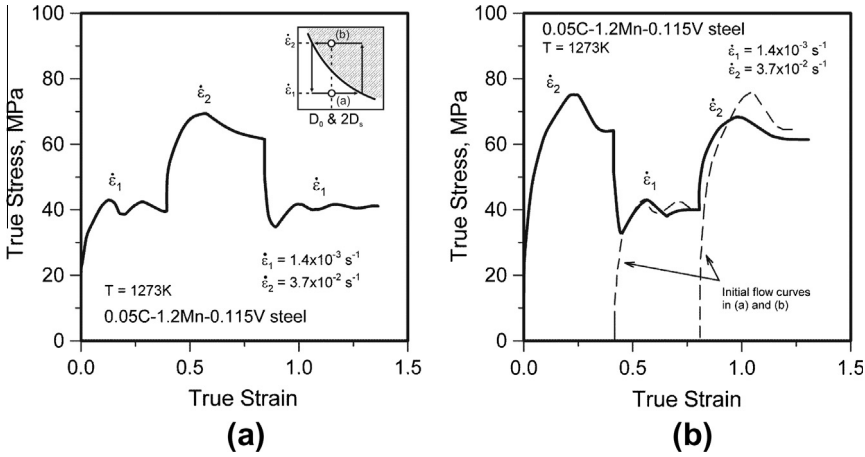
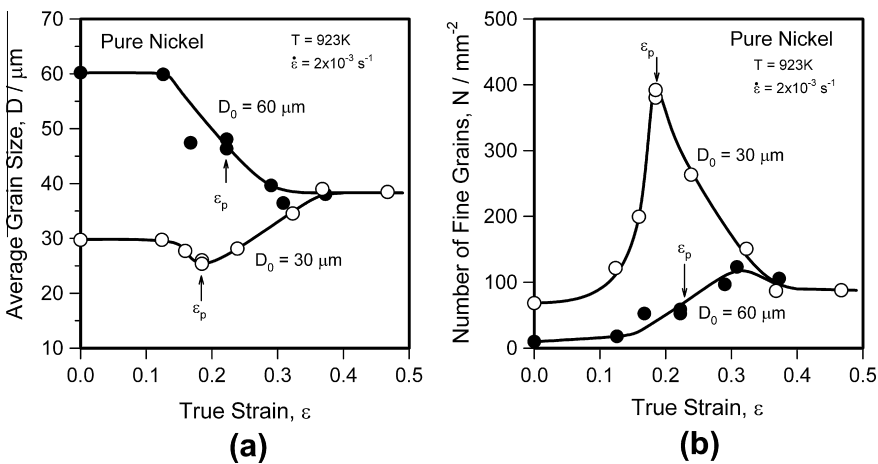


Fig. 12. Microstructure mechanism map for distinguishing between the two types of dDRX. The curves describing the  $Z$ - $2D_s$  and  $Z_c$ - $D_o$  relations separate the single peak (grain refinement) and multiple peak (grain coarsening) regions. Three distinct types of experiments are represented here known as vertical (V), horizontal (H), and combined (H/V) tests [20,67].



**Fig. 13.** Examples of H/V tests involving strain rate changes carried out on a 0.115% V steel deformed at 1273 K; (a) the strain rate was cycled from  $1.4 \times 10^{-3}$  to  $3.7 \times 10^{-2} \text{ s}^{-1}$  and back to  $1.4 \times 10^{-3} \text{ s}^{-1}$  at strain intervals of about 0.45; (b) the strain rate was cycled from the higher to the lower value and then back again [67].

The third type of RGS experiment consists of H/V tests that involve strain rate changes during straining. An example is provided in Fig. 13, which depicts the stress–strain curves determined on a 0.115% V steel deformed at 1273 K. In Fig. 13a, the strain rate was increased from  $1.4 \times 10^{-3}$  to  $3.7 \times 10^{-2} \text{ s}^{-1}$ ; in Fig. 13b, the reverse change was performed [67]. When the strain rate was suddenly increased to  $\dot{\epsilon}_2$  after attainment of the stable microstructure at  $\dot{\epsilon}_1$ , grain refinement and single peak flow were expected to occur according to the RGS model. These predictions were confirmed by the results displayed in Fig. 13a. It is important to note that the transition behaviors produced in this way were completely reversible and so are consistent with dDRX being controlled by a thermally activated mechanism [66–68]. It should be underlined that the reversible dDRX phenomena just described stand in sharp contrast to those taking place under cDRX conditions. These phenomena will be considered in detail in Section 4, whether the irreversible and athermal aspects of cDRX behavior will be described.



**Fig. 14.** Effect of initial grain size  $D_0$  on (a) average grain size  $D$  and (b) number of fine grains  $N$  per unit area less than  $10 \mu\text{m}$  in diameter. Here nickel samples were deformed in tension at 923 K at a strain rate of  $2 \times 10^{-3} \text{ s}^{-1}$  and then hydrogen quenched [66].

Finally, the development of dDRX microstructures will be examined in the light of the RGS model. Some changes in grain size  $D$  taking place during the high temperature deformation of Ni are illustrated in Fig. 14a [66]. Here, samples with two different initial grain sizes (30 and 60  $\mu\text{m}$ ) were deformed in tension to several strains at 923 K and a strain rate of  $2 \times 10^{-3} \text{ s}^{-1}$  and then hydrogen gas quenched. It is evident from Fig. 14a that the 60  $\mu\text{m}$  sample displays continuous grain refinement until the stable grain size of 38  $\mu\text{m}$  is attained. This experiment was associated with single peak flow (not shown here). Conversely, the 30  $\mu\text{m}$  specimen underwent coarsening to the same final stable size. In this case, the flow curve was of the multiple peak type (not illustrated).

The dependence of the density of fine grains ( $<10 \mu\text{m}$  in diameter) per unit volume  $N$  on strain in this experiment is illustrated in Fig. 14b. It can be seen that the nucleus density  $N_o$  at  $\epsilon_p$  in the 30  $\mu\text{m}$  sample is much higher than the stable value ( $N_s$ ) at high strains. These results indicate that the relative nucleus density  $N_o/N_s$  determines the shape of the dDRX flow curve. When the ratio is greater than one, the curve is of the multiple peak type. Conversely, when it is less than one, single peak behavior will be observed. Here  $N_o$  and  $N_s$  correspond to the nucleus density at the start of dDRX (i.e. prior to  $\epsilon_p$ ) and the stable value at high strain, respectively. The relationship between  $D$  and  $N$  is given approximately by  $N = 2P/D$  (where  $P$  is the probability of activation of a grain boundary site per unit surface area) [20,66,67]. In the fine grained material ( $D_o < 2D_s$ ),  $N_o > N_s$ , and the growth of each new dDRX grain is terminated by boundary impingement. This leads to the development of an intermediate grain size  $D'_s$ , where  $D'_s < D_s$  because of the initial excess density of nucleation sites. The value of  $D'_s$  increases with each cycle of recrystallization until it attains the stable value  $D_s$ . In the coarse grained material ( $D_o > 2D_s$ ),  $N_o < N_s$ , and grain refinement occurs until the appropriate density  $N_s$  is attained.

Before terminating this section, the relation between the deformation conditions (i.e.  $Z$ ) and the stable dynamic grain size  $D_s$  will be discussed briefly because of its importance in understanding dDRX behavior. It was mentioned above that  $D_s$  depends sensitively on  $T$  and  $\dot{\epsilon}$ , where the dependence can be expressed as a function of  $Z$ ; there is a similar link between  $D_s$  and the steady state stress  $\sigma$  [12–23,40,61–63]. Some typical relationships between the normalized steady state flow stress and the normalized grain size are illustrated in Fig. 15 for various metallic materials. The original figure prepared by Derby [21] included minerals such as pyrite, halite, and olivine as well as metals. Derby found that all the data fell in a remarkably narrow range bounded by loci of the form

$$(\sigma/G)(D_s/b)^{2/3} = K_2, \quad 1 < K_2 < 10 \tag{5}$$

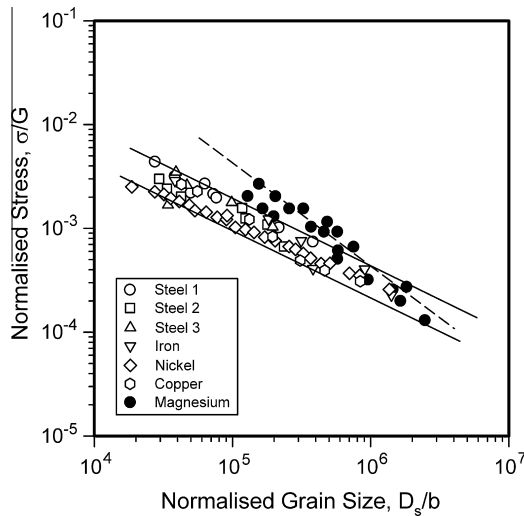


Fig. 15. Relationship between flow stress normalized by the shear modulus and dDRX grain size normalized by the Burgers vector for metallic materials. (In the original figure prepared by Derby [21], the data included a number of minerals as well.) The solid line represents fcc metals undergoing dDRX and the broken line Mg undergoing cDRX.

He showed that such a relation can be derived by considering that a dynamic balance is achieved between the rate of formation of the dislocation substructure on the one hand and its removal on the other, as determined by the mean velocity of the dDRX grain boundaries. It can clearly be seen in Fig. 15 that when only the fcc metals are taken into consideration, the data fall in a much narrower range, as indicated by the solid lines. This is bounded by loci of the form:

$$\sigma/G = K_3(D_s/b)^{-2/3}, \quad 1 < K_3 < 2 \quad (6)$$

Such a relationship between  $\sigma$  and  $D_s$  has been reported by many researchers [12–23,40,61–63,66].

Finally it is of interest to note that the data for Mg in Fig. 15 are not well expressed by Eq. (6), but may be approximated by a dashed line with a slope of 0.9–1.0. Similar results have been reported for the AZ31 Mg alloy [69]. This indicates that new grain formation in Mg alloys probably does not result from the dDRX model discussed above. Some insight into the factors responsible for this atypical behavior can be gained from the work of Yang et al. [69,70]. They showed that new grain formation in Mg alloys is affected by a series of strain-induced reactions, such as grain fragmentation due to the formation of kink bands. As this type of process bears some resemblance to cDRX, it will be taken up again in Section 4.

### 3.5. Application to industry

#### 3.5.1. Rolling simulations

Because of the link between structure and properties, it is essential to produce desirable microstructures during industrial rolling, particularly in the case of steel. For this reason, there have been numerous studies in which rolling simulations have been carried out in order to characterize and optimize the types of structures that are likely to be produced in the plant. These simulations also provide estimates of the rolling load, separation force, and torque via the mean flow stress (MFS). Although dDRX is not always initiated during hot rolling, simulations can be used to predict the cases when it is expected to take place.

The effect of interpass time on the conditions for the initiation of dDRX is described first. This is because the length of the interpass interval plays a huge role during industrial processing. When interpass times are very short, as in the finishing stages of rod rolling, there is insufficient time for static recrystallization (SRX) or for carbonitride precipitation. Under these conditions, strain accumulation takes place, leading to the initiation and propagation of dDRX. Conversely, when interpass times are long, as in plate rolling and when reversing mills are being used, there is ample time for SRX or, in microalloyed steels containing Nb, for carbonitride precipitation. The latter prevents the initiation of dDRX. In the case of strip rolling, the interpass times fall between those of rod and plate rolling. In this case, there is no or only limited SRX, leading to strain accumulation and the initiation of dDRX in the general case. The effect of interpass time on the nature of the softening processes taking place and, in particular, on whether dDRX has been initiated or not, has received considerable attention. Discussions of this topic can be found in [71–75].

The finishing stages of seamless tube rolling have been studied in laboratory simulations and the results published in Refs. [76–78]. These have shown that strain accumulation takes place, leading to the initiation of dDRX. This is because of the short ( $\approx 0.5$  s) interpass times in the finishing stages. The occurrence of dDRX under these conditions can be deduced from the shape of the envelope of the set of flow curves, as shown in Fig. 16. In such cases, dDRX plays a large role in establishing the final austenite microstructure and grain size (prior to transformation). Descriptions of rod rolling simulations are available in Refs. [79–84] and an example of a torsion simulation is provided in Fig. 17. Here it can be seen that, as in the case of seamless tube rolling, SRX does not take place during the short interpass intervals (as short as 20 ms) applicable to the finishing stages of rolling. Instead, there is strain accumulation during the six finishing passes, leading to the initiation of dDRX. In the presence of Nb, there is an absence of SRX even at the relatively high temperature of 1100 °C such that strain accumulation takes place, again leading to dDRX. As dDRX can be followed by rapid metadynamic recrystallization (mDRX) this may lead to sudden load drops, although this is not of particular concern in rod rolling as the process does not require careful control of reduction and rolling load.

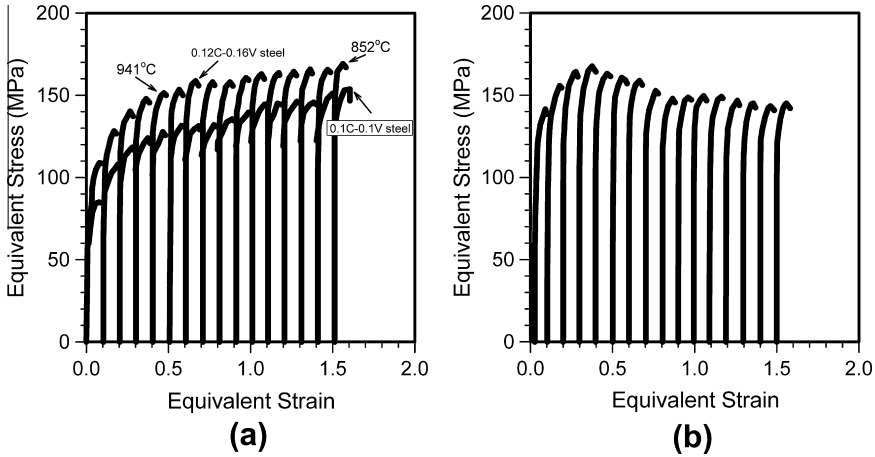


**Fig. 16.** Torsion simulations of a sixteen pass rolling schedule applied to two V steels in a stretch reducing mill (SRM) [76]. (a) The experimental data; (b) after correction to a constant temperature of 905 °C. Note that the flow curve envelope displays the characteristic ‘single peak’ curve indicative of dDRX.

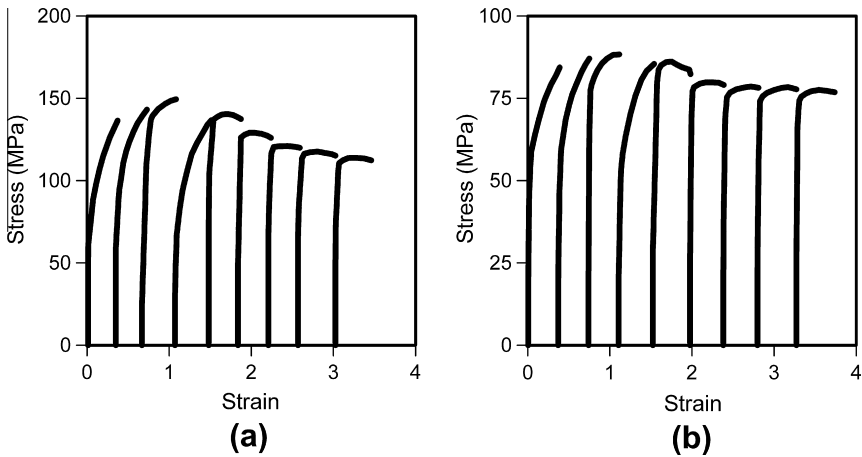


**Fig. 17.** (a) Torsion flow curves determined on a plain C steel at 900 °C [84]. The last six passes, which collectively exhibit the characteristics of dDRX, make up the finishing schedule. (b) Flow behavior of a Nb microalloyed steel at 1100 °C; the envelope of the finishing passes is again indicative of dDRX.

Plate rolling simulations are generally concerned with determining the  $T_{nr}$ , the temperature at which full SRX is no longer able to take place during rolling. This defines the point in the schedule at which strain accumulation begins, leading to the ‘pancaking’ of austenite (important for the production of fine grain sizes in high-toughness steels). A full description of the most common (‘Boratto’) method of determining the  $T_{nr}$  is given in [85,86]. Examples of plate rolling studies can be found in [87,88]. The results of a typical multi-pass simulation on a torsion machine are presented in Fig. 18a, on which the change in the shape of the pass flow curve after pass 7 can be readily seen. The shape change indicates that static recrystallization is no longer taking place between passes. An example of a mean flow stress (MFS) vs. inverse absolute temperature ( $1/T$ ) plot determined in such simulations is presented in Fig. 18b. Here it can be seen that the  $T_{nr}$  can be readily identified from the

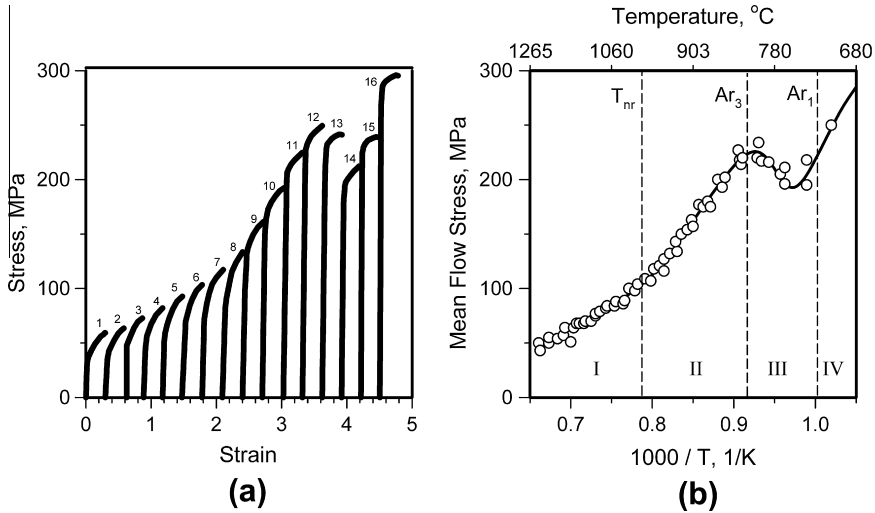


**Fig. 18.** (a) Torsion simulation of an average schedule on a Steckel mill; microalloyed steel, 30 s interpass times, cooling rate – 1 °C/s [85]. (b) MFS vs.  $1/T$  plot based on four sets of simulation flow curves. The change in slope identifies the  $T_{nr}$  temperature, departures from linearity, the upper ( $Ar_3$ ) and lower ( $Ar_1$ ) critical temperatures [86].

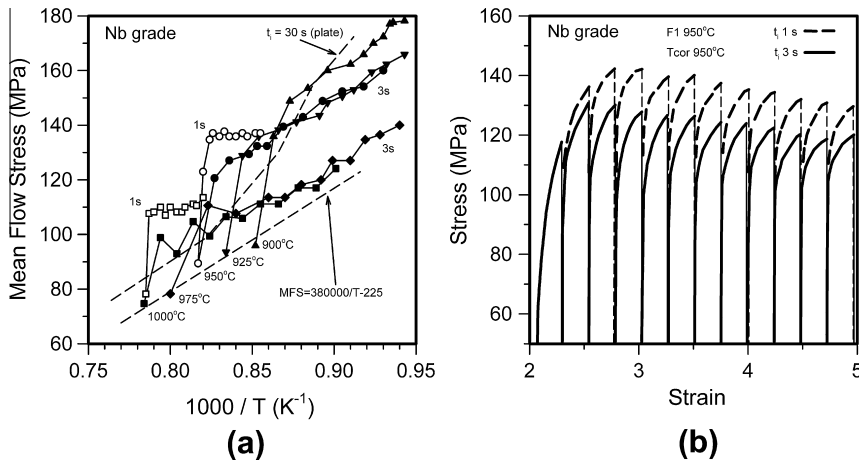


**Fig. 19.** (a) Simulations of plate (30 s interpass times) and strip (1 s and 3 s interpass times) rolling [95]. The cooling rate in the strip rolling cases was 10 °C/s. Note the low rates of increase in MFS with decreasing temperature in the four strip mill simulations. (b) The two sets of flow curves determined in the strip mill simulations with entry temperatures of 950 °C; these have been corrected to a constant temperature of 950 °C to show how increasing deformation produces increasing “softness” in the test specimens.

change in slope, which defines the temperature below which SRX is no longer able to take place or go to completion. From this point onwards, there is strain accumulation, although it is important to note that this does not lead to dDRX in microalloyed steels because of the carbonitride precipitation that takes place during the interpass intervals.

Accounts of the physical simulation of strip rolling can be found in Refs. [89–95]. An example of the results obtained in torsion simulations is presented in Fig. 19a. Here, interpass times of 1 and 3 s were employed and it can be seen that the rate of increase in MFS with  $1/T$  is much lower than in the case of

the plate rolling (30 s) simulations. The 950 °C ‘entry temperature’ continuous-cooling flow curves of Fig. 19a are shown replotted in Fig. 19b after correction to a constant deformation temperature of 950 °C. Here it can be seen that the corrected flow stress decreases continuously during continued straining. This is due, not only to the initiation of dDRX during rolling, but also to that of dynamic transformation (DT), a topic that is treated in Section 3.6. The occurrence of dDRX followed by mDRX in combination with DT can lead to unexpected flow stress drops or reductions in rolling load. Some general reviews of the occurrence of dDRX under hot rolling conditions can be found in publications such as [96–99] while briefer accounts of the conditions under which dDRX is expected to take place are available in [100–108]. The phenomenon of dDRX in Cu-30Ni has been discussed in [109], in Mg alloys in [110], and in 304 stainless steel in [111–113]. Constitutive relations applicable to dDRX have been proposed in [114], while the application of self-consistent models to the development of torsion textures when dDRX is taking place is described in [115].

### 3.5.2. Kinetics of dDRX and mDRX

The Avrami formalism is generally used to quantify the kinetics of SRX [e.g. 4]. Nevertheless, it can also be employed to describe those of dDRX and mDRX. Examples of such studies can be found in [116–122]. A recent improvement in Avrami models involves expressing the softening produced with respect to the austenite that has not yet been subjected to recrystallization, but is continuing to strain harden [123]. Here the work hardening behavior of the unrecrystallized component of the microstructure is deduced from the initial part of the flow curve, which has not yet been affected by the initiation of dDRX; this behavior is then extrapolated beyond the critical strain [123–127]. Some examples of Avrami plots describing the progress of dDRX are presented in Fig. 20 [126]. In this diagram, the extent to which coarse microstructures retard dDRX can be readily seen as well as the effects of deformation temperature and composition. The addition of alloying elements to steels and other metals is well known to retard recrystallization as a result of solute drag. Such solutes can modify the transformation behavior as well as retard recrystallization. In the case of boron addition, the latter effect is discussed in Ref. [128]. The influence of substitutional alloying elements on the rate of softening in nickel is treated in [129–131] and solute retardation more generally in [132].

Once dDRX has been initiated, it is generally followed by mDRX. This is much more rapid than the conventional type of SRX that follows deformation in the absence of dDRX. The rapid kinetics are generally explained in terms of the elimination of the time required to nucleate new grains (because of the prior occurrence of dDRX) so that only *growth* of the new grains is involved. This topic is treated in detail in Section 5. The occurrence of mDRX has been studied under simulated hot rolling conditions

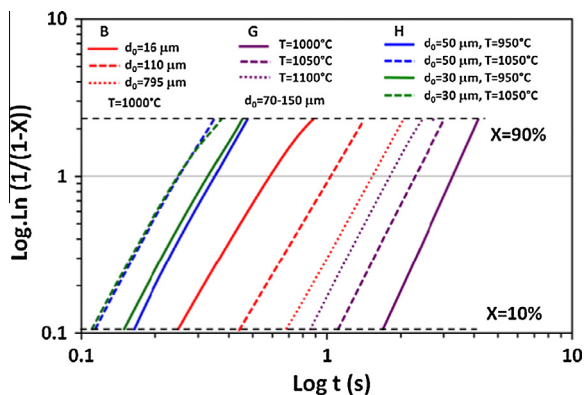
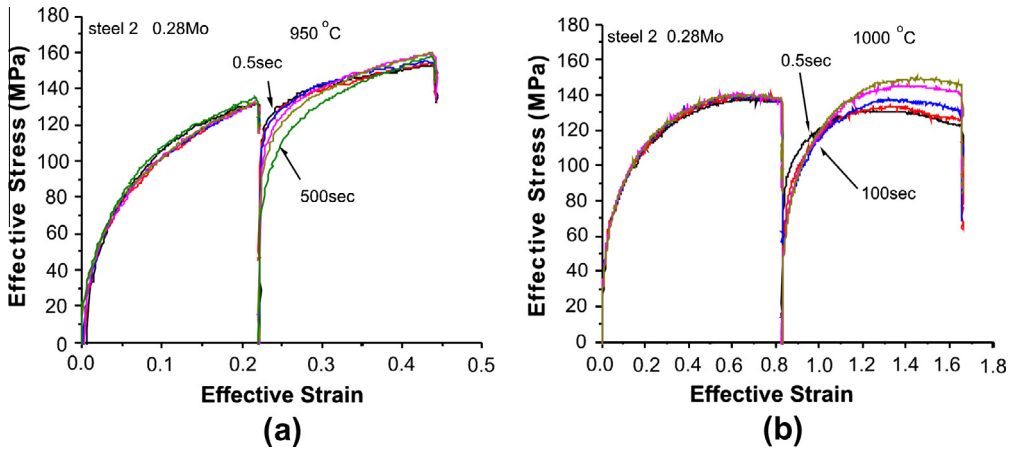
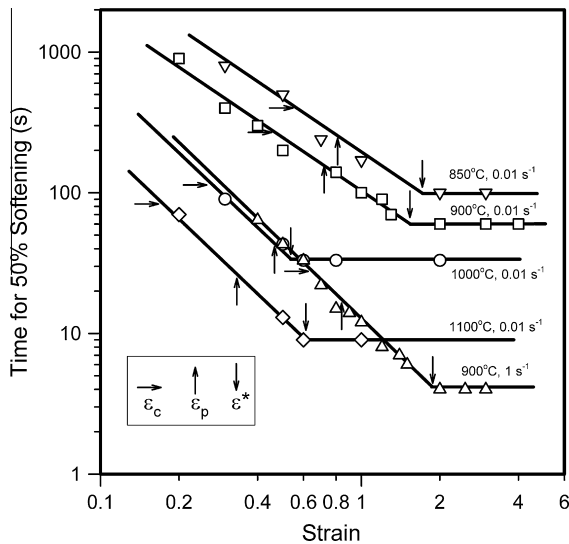


Fig. 20. Avrami plots of the softening produced by dDRX during compression testing. The data were obtained on the following steels: B (C: 0.07, Mn: 0.62, Si: 0.01, Ti: 0.067, Nb: 0.034); G (C: 0.23, Mn: 0.74, Si: 0.22, Cr: 0.90, Mo: 0.08) and H (C: 0.03, Mn: 0.3) and show the effects of test temperature and initial grain size [125].



**Fig. 21.** (a) Interrupted compression flow curves determined on a Nb microalloyed steel containing 0.28% Mo at 950 °C [139]. After a prestrain of 0.22, the only softening observed on reloading after a 0.5 s unloading interval is due to static recovery (no SRX). (b) After a prestrain of 0.82 at 1000 °C (where dDRX is well under way), there is very rapid and almost complete softening after only 0.5 s.



**Fig. 22.** Time of half-softening as a function of strain after deformation under a variety of conditions determined in torsion on a 304 stainless steel. dDRX is initiated at  $\epsilon_c$ , mDRX takes place on unloading at strains beyond  $\epsilon_c$ , and the time of half-softening becomes strain independent at  $\epsilon^*$  [142].

and described in Refs. [80,84,133–139]. The large differences in the rates of softening produced by SRX as opposed to mDRX are illustrated in Fig. 21a (static) and b (metadynamic).

An interesting sidelight concerning mDRX is that the kinetics of this softening mechanism become strain independent once a certain prestrain is attained [140]. This topic has been explored in several publications [138,141] and a possible explanation has been put forward in Ref. [142]. An illustration of the strain at which the kinetics of softening become strain independent is given in Fig. 22. This inves-

tigation was carried out on a 304 stainless steel, which permitted measurement of the volume fraction recrystallized as well as of the kinetics of softening. It can be seen from the diagram that strain-independence of the time of half-softening  $t_{50}$  is attained well after the peak in the flow curve ( $\epsilon_p$ ). It corresponds instead to the moment ( $\epsilon^*$ ) when the volume fraction recrystallized dynamically (determined metallographically) has attained 50% [142]. Thus, even if dDRX has progressed beyond the point where 50% of the volume of the material has been ‘transformed’, the rate of mDRX is not affected or increased.

### 3.5.3. Effects of dDRX on ductility and texture

Because dDRX removes dislocations and refines the grain size, it can improve the ductility as well as the toughness if it is initiated during deformation. This can also be of particular importance during continuous casting, when slab straightening is taking place and tensile stresses are induced locally. The effect of dDRX on ductility has been described in [143,144].

Texture control in industrial materials is of great importance because of the significant effect of texture on properties. In principle, it should be possible to use the occurrence of dDRX to produce improved textures. Conversely, in the case where its effect on the texture is harmful, it is essential to prevent dDRX from being nucleated. Unfortunately, there is a significant lack of suitable models that can be used to predict the effect of dDRX on texture, although a promising approach has been presented in [115]. Furthermore, there is not a great deal of experimental evidence demonstrating its effect along the different industrial strain paths, such as extension, compression, plane strain deformation (i.e. rolling) or shear. Generally speaking, dDRX, when initiated, has the effect of somewhat randomizing the texture or at least rendering the deformation texture less intense, as was seen above in Fig. 11. The results of an investigation of the effect of dDRX on torsion (shear) textures can be found in [145,146] and on textures more generally in [147–151]. A model for the operation of oriented nucleation and selective growth during dDRX has been published as Refs. [115,152,153].

### 3.6. Detection of the dDRX critical strain

It is important to determine the critical strain for the nucleation of dDRX. Unfortunately, it is difficult to employ metallography to establish the precise moment when dDRX is initiated, because of the instability of conventional austenite at room temperature. Fortunately, a very accurate method, known as the double-differentiation technique, was developed in 1996 [154] and is now in wide use. It involves measuring the slope  $\theta = \partial\sigma/\partial\epsilon$  of a stress–strain curve, taking the derivative of this

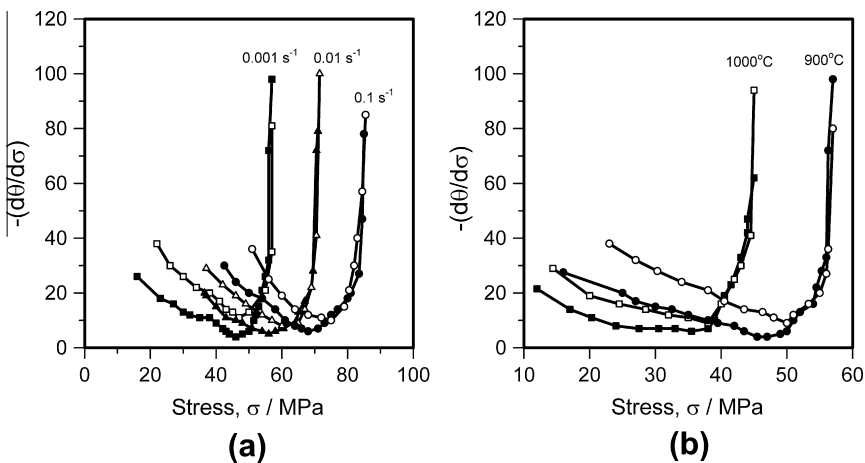


**Fig. 23.** Effects of (a) strain rate and (b) temperature on the flow stress dependence of  $-d\theta/d\sigma$  in nickel [154]. The stresses that correspond to the minima in these plots must then be located on the original flow curves in order for the critical strains to be identified.

slope with respect to stress, i.e. calculating the value of  $\partial\theta/\partial\sigma$ , and then plotting the negative of the latter value against stress. A local minimum in this parameter identifies a point of inflection in the curve of slope vs. stress and therefore specifies the moment when a new softening process is initiated (in addition to dynamic recovery). Because “noise” in experimental stress/strain curves renders differentiation difficult, measured flow curves must first be smoothed using appropriate polynomials, usually of order 8 or higher [154–157]. It is of interest that this technique does not require the test to be run at constant strain rate, but is also applicable to variable rate deformation [158] and to any testing mode, i.e. tension, compression, plane strain tension or compression, and shear (torsion) [155,157].

Typical plots of the second derivative against stress taken from the original publication are shown in Fig. 23 [154]. A modification of the double derivative method that leads to considerable simplification has been proposed in Ref. [159]. The minima illustrated in Fig. 23 pertain to the high temperature deformation of nickel; similar plots were derived from flow curves measured on a type 304 stainless steel and were also reported in Ref. [154] but are not reproduced here. These two metals do not undergo phase changes on cooling and so are not susceptible to dynamic transformation. The same conditions apply to fcc metals such as Ag, Au, Cu, Pb, and Pt. However, conventional austenite *does* transform into ferrite and cementite on cooling or into other metastable phases. Furthermore, as shown by Yada and co-workers in the 1980s [160,161], the transformation to ferrite can be induced at temperatures well above the  $Ae_3$  when austenite is being deformed, whether in the laboratory or in a rolling mill. The effect of dynamic transformation (DT) on dDRX-type flow curves will now be discussed.

### 3.6.1. Dynamic transformation

Because ferrite is softer than austenite at a given temperature, this property leads to a reduction in flow stress compared to that applicable to untransformed austenite. Such softening makes it also possible to detect the initiation of the transformation by the double differentiation method [162,163]. However, care must be taken for the two critical strains (one for DT and one for dDRX) to be distinguished from one another. When there are two possible minima, the use of polynomial orders (for smoothing) as high as 12 are required if the *entire* flow curve is being fitted; otherwise seventh or eighth order polynomials are usually sufficient [164].

Examples of two sets of double derivative minima are presented in Fig. 24a. These curves were derived from compression tests carried out on a 0.038% Nb microalloyed steel with an ortho-equilibrium

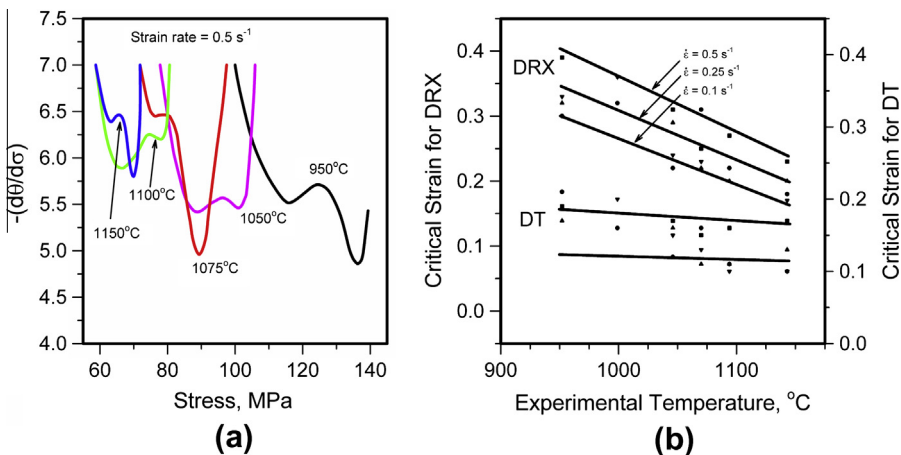


**Fig. 24.** (a) Dependences of the second derivative of the stress on stress in a 0.11% C–0.038% Nb steel derived from compression testing flow curves. (b) Dependences of the dDRX and dynamic transformation (DT) critical strains on deformation temperature. The DT critical strains decrease slightly with temperature, while the dDRX critical strains decrease more rapidly with temperature and decreasing strain rate in the usual way [164].

$Ae_3$  temperature of 848 °C [164]. As can be seen, DT minima were observed right up to 1150 °C, i.e. to 300° above the conventional upper critical transformation temperature. The critical strains determined in this way are illustrated in Fig. 24b, from which it can be seen that DT is initiated well before dDRX at strains of about 0.05–0.1. Under the high strain rate conditions applicable to industrial rolling, the dDRX critical strains are considerably higher than those shown here and the gap between the two strains is therefore greater than indicated in the diagram.

Similar results have been reported for four other steels deformed in torsion, where again the critical strains for the initiation of DT preceded those for dDRX [165]. These observations have two important implications. One is that the ubiquitous “single peak” austenite flow curve is a product of two softening mechanisms (in addition to dynamic recovery), DT as well as dDRX. (This conclusion does not apply to the other fcc metals mentioned above.) The other is that the unexpected drops in rolling load observed at temperatures above the  $Ae_3$  actually have their origins in the operation of both the above softening mechanisms (i.e. DT and dDRX) and not just dDRX followed by mDRX. The interested reader is referred to Ref. [166], where this topic is treated in more detail.

## 4. Continuous dynamic recrystallization and severe plastic deformation

### 4.1. General characteristics of flow behavior and microstructures developed

#### 4.1.1. Historical development of severe plastic deformation

The development of severe plastic deformation (SPD) techniques was motivated by an interest in producing ultrafine grained (UFG) metallic materials. These were expected to possess beneficial combinations of physical, chemical, and mechanical properties. It should be noted that plastic deformation accompanied by dDRX is a unique method for producing grain refinement in metals that do not undergo phase transformation. Since the dynamic grain size that is produced during working depends sensitively on the deformation conditions and in particular decreases as the temperature is decreased, as described in detail in Section 3, superior grain refinement can be expected to involve the use of relatively low deformation temperatures. Unfortunately, the critical strain for the initiation of dDRX increases drastically as the deformation temperature is reduced. Methods for producing UFG

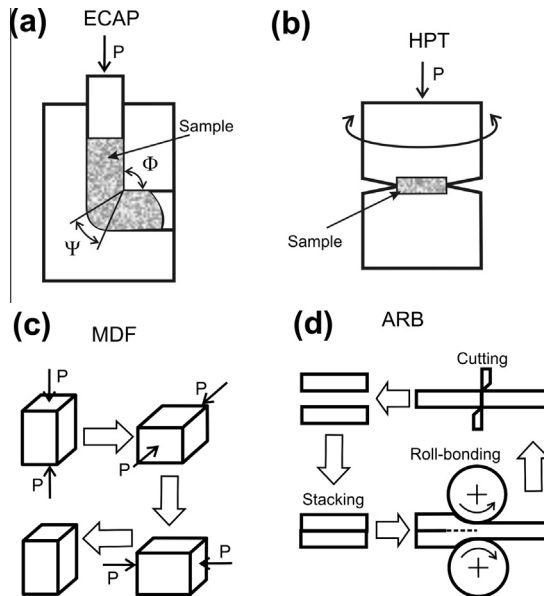


**Fig. 25.** Principles of (a) equal channel angular pressing (ECAP), (b) high pressure torsion (HPT), (c) multi-directional forging (MDF) and (d) accumulative roll bonding (ARB).

materials must therefore be based on a different mechanism, which must still involve relatively low temperatures, and will necessarily require the application of very large strains. Examples of representative SPD techniques are illustrated in Fig. 25 and will now be described briefly in turn.

Following the principles outlined by Segal et al. [167], the equal channel angular pressing (ECAP) method was developed and has been used successfully for over three decades. It is particularly well studied for processing soft materials and has become quite popular [30,168–170]. The sample is pressed through two intersecting channels of the same shape and cross section and the equivalent strain is evaluated as follows [30]:

$$\varepsilon = \{2 \cot[0.5(\phi + \psi)] + \psi \operatorname{cosec}[0.5(\phi + \psi)]\} / \sqrt{3} \quad (7)$$

Here  $\phi$  is the inner angle between the channels and  $\psi$  is the outer or shear zone included angle of channel intersection (see Fig. 25a). Because the cross-section of the sample is kept constant, it can be passed repeatedly through the die, leading to the accumulation of large strains. The specimen can be pressed repeatedly in the same manner or it can be rotated between passes by 90° or 180° [30,170].

Another frequently used technique is torsion under high axial pressure, known as high pressure torsion (HPT) [171,172] (Fig. 25b). The strain that is imposed on a disc-shaped sample depends on the thickness ( $t$ ), radius ( $R$ ) of the specimen, and rotation angle ( $\theta$ ) in radians [171]:

$$\varepsilon = (\theta R) / (t\sqrt{3}) \quad (8)$$

Note here that Eq. (8) above does not agree with Eq. (1) in [30] nor with Eq. (6) in [172], which are both in error, as explained in some detail in [171]. When the specimen thickness is reduced during HPT, an additional component of compressive strain must be added to the imposed shear strain. In comparison with ECAP, HPT does not require costly equipment and can be employed on a wide variety of metals and alloys, including hard-to-deform materials. One limitation is that it cannot be used on large samples.

In the early 1990s, multi-directional forging (MDF) was developed as a simple method for applying large strains that is particularly useful for the processing of bulk products [173]. True stress–true strain diagrams are readily obtained when this technique is used [46,48]. According to this method, a prismatic specimen is compressed sequentially along its three principal axes, as shown in Fig. 25c. As long as the strain in each forging pass (determined by the ratio of the initial to the final dimension of the specimen, i.e.  $\varepsilon = \ln(H_i/H_f)$ ), is well below 1, the shape of the specimen does not change appreciably as a result of multiple deformations.

At the end of the last century, another promising SPD technique known as accumulative roll-bonding (ARB) was developed to produce large bulk semi-products using a conventional rolling mill (Fig. 25d) [174,175]. According to this process, a sheet of material is rolled to 50% reduction and then cut into two portions; these are stacked together and rolled again. This procedure can be repeated many times so as to achieve the final total strain required. The latter is given by  $\varepsilon = (2/\sqrt{3})n \ln(1 - r)$ , where  $n$  and  $r$  are the number of ARB cycles and the fractional reduction in thickness per cycle, respectively. The ARB technique does not require any special equipment and can be used to apply very large strains as the initial dimensions of the sample do not change. A disadvantage of the ARB technique is that it necessitates careful surface treatment, e.g. degreasing and wire brushing, before stacking so as to achieve good bonding and avoid delamination.

The SPD methods described above are now widely used to study deformation behavior and microstructure evolution during SPD as well as to produce samples for property determination. There are a number of additional techniques that also qualify as methods of SPD, such as mechanical milling, cyclic extrusion/compression, continuous cyclic bending, repetitive corrugation and straightening, and high pressure tube twisting [176–182]. Among these, mechanical milling has been the most extensively studied. During mechanical milling, individual powder particles receive very large strains, although the actual amount cannot be estimated. Another difficulty is that the samples require additional consolidation. Thus mechanical milling is not well suited for the investigation of stress–strain behavior and microstructure development. The other techniques mentioned above are not frequently

used, although data are available on cyclic extrusion/compression [176] and/or other newly introduced methods [179–182].

#### 4.1.2. Microstructural characteristics developed under SPD conditions

The plastic working of metals and alloys at relatively low temperatures produces a hierarchy of dislocation substructures [183–188]. The initial stages of straining introduce high dislocation densities, which are arranged in cellular substructures. An increase in strain is attended with localizations of plastic flow on a microscopic scale. The dislocation cells evolve into cell blocks that are subdivided by dense dislocation walls; these are essentially dislocation sub-boundaries whose misorientations are appreciably larger than those of common cell walls. Then, various deformation bands begin to appear at medium strains that introduce still larger misorientations. This leads to the subdivision of the original grains into small, heavily misoriented fragments. This process of grain subdivision during deformation is fundamental to the process of grain refinement by SPD.

In addition to the deformation bands, other structural elements are introduced during strain localization that depend on the material being processed and on the deformation conditions. These have been called microbands of the first and subsequent generations, S-bands, microshear bands, etc. [49,187]. The formation of such large misorientation dislocation boundaries is associated with differences in the strain states across the boundaries [49]. Such strain-induced sub-boundaries are, therefore, referred to collectively as geometrically-necessary boundaries. This is in contrast to incidental boundaries, which are essentially low-angle boundaries consisting of statistically stored dislocations. During a unidirectional deformation process such as cold rolling, an increase in the total strain leads to the formation of layered microstructures and the alignment of the transition bands, grain boundaries and sub-boundaries. This has the result that the normals to the flattened units are rotated until they are approximately parallel to the normal direction of rolling. Thus, the microstructures present at large strains are characterized by ribbon-like subgrains and grains that are highly elongated in the direction of metal flow [168,185].

The normal dimensions of the elongated structural elements decrease with increasing strain and gradually approach some constant value at large strains. These directional features of the microstructure have been observed and described in detail for such SPD methods as ECAP, HPT, and ARB. The employment of these techniques has shown that uniform microstructures composed of equiaxed grains well below a micrometer in diameter can be readily produced in this way [30,168–170]. The most impressive grain refinement results have been obtained using the HPT technique [172,189,190]. Typical nanocrystalline structures developed using HPT methods are shown in Fig. 26a [189]. The severely strained microstructure is composed of heavily misoriented nearly equiaxed crystallites ten to one hundred nanometers in diameter and characterized by large internal stresses estimated from the streaks in the diffraction data. Similar microstructures have only been observed after high energy mechanical milling, as seen in Fig. 26b [191].

The mechanical behavior during SPD is usually evaluated by measuring the hardness of samples processed to various total strains. This is because the most frequently used SPD methods, such as

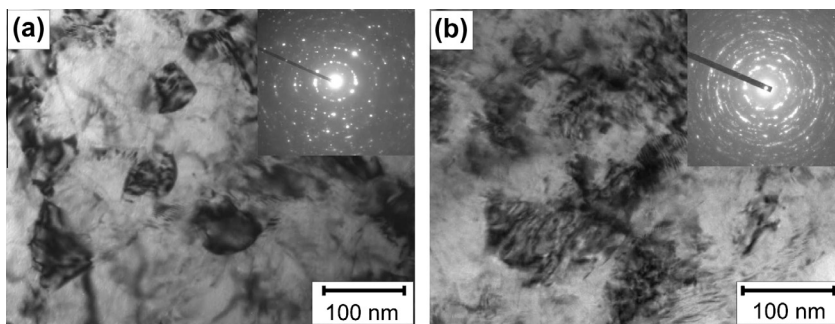


**Fig. 26.** Severely deformed microstructures developed in (a) a 15% Cr ferritic stainless steel subjected to HPT to a strain of 4 [189] and (b) an Fe-0.6% O steel powder prepared by mechanical milling for 300 h [191].

HPT and ECAP, do not allow recording of the stress–strain diagram, although the recently developed technique of high pressure tube twisting [192] does provide the stress–strain data and, therefore, has considerable potential for further comprehensive investigations of SPD and related phenomena. The development of nano-crystalline and submicron-sized structures during SPD has generally been shown to be accompanied by an increase in hardness, which exhibits a tendency to saturate at large total strains [193]. The formation of UFGs during SPD is accompanied by a drastic increase in total grain boundary area. Moreover, the nature of the boundaries in severely strained materials differs somewhat from that evolved by conventional thermomechanical treatments. The boundaries in nano-crystalline materials subjected to SPD exhibit a specific diffusive diffraction contrast on TEM images that appears to be indicative of their non-equilibrium state [194].

It is worth noting that the development of nanocrystalline structures during SPD is accompanied by a decrease in dislocation density at large strains. Indeed, severely deformed materials commonly contain fine grains that are completely free of dislocations. Nevertheless, the crystal lattices of the fine grains are frequently characterized by large elastic distortions, as can be seen in Fig. 27a [195]. The numbers indicate the orientation differences (in degrees) between pinpointed regions within the grains as revealed by the convergent beam Kikuchi line technique. The high-resolution TEM micrograph of Fig. 27b again indicates the presence of large internal distortions in the submicrocrystalline structures developed by SPD [193]. Since the grains selected for the distortion analysis do not contain dislocations, such elastic distortions and the related internal stresses are attributed to the non-equilibrium state of the strain-induced boundaries introduced by SPD. The high internal stresses can act as back stresses opposed to dislocation movement and, therefore, may be responsible for both the decrease in dislocation density and the high hardness of SPD materials. Some of the links between the microstructural and mechanical observations described above will now be considered in the sections that follow.

#### 4.2. Ultrafine grain microstructure development under SPD conditions

##### 4.2.1. Multi-directional forging

Many of the SPD techniques described in Section 4.1.1 have provided valuable information regarding the UFG microstructures produced by SPD. However they have provided little insight into the flow stress behavior or the relation between the flow stress and the microstructures developed. Among the various SPD methods illustrated in Fig. 25, multi-directional forging (MDF) has the following advantages:

- (1) When increments of compression are carried out accompanied by sequential changes of loading direction along the three perpendicular axes, the flow stress vs. strain relationship can be systematically investigated. The development of the microstructure can be followed concurrently.

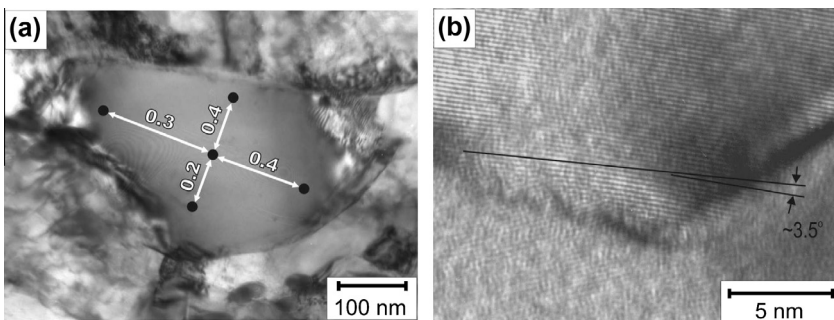


**Fig. 27.** Large distortions developed in (a) a 304 stainless steel subjected to MDF to a strain of 6.4 [195] and (b) an 18% Cr–7% Ni stainless steel processed by swaging to a strain of 3.2 [193]. The numbers in (a) indicate the lattice orientation differences between the identified areas in degrees.

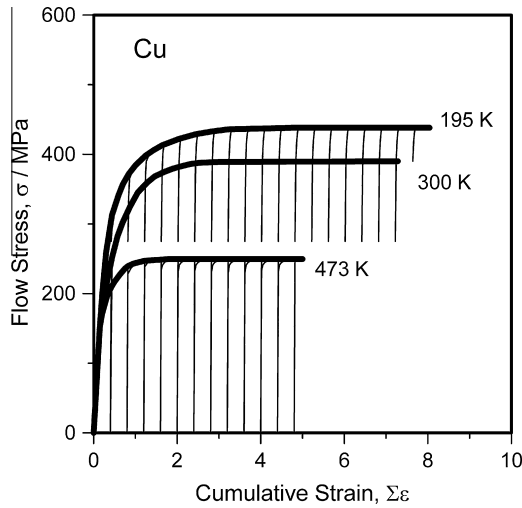


**Fig. 28.** A series of flow stress–cumulative strain curves for pure copper processed by MDF with pass strains of 0.4 to various cumulative strains  $\Sigma\varepsilon$  at a strain rate of  $3 \times 10^{-3} \text{ s}^{-1}$  at temperatures of 195 K, 300 K and 473 K [46,48,196]. The flow curve envelope at 195 K extends to a strain of  $\Sigma\varepsilon = 18$  (not shown).

- (2) As a consequence, the progress of microstructure formation and of work hardening can be followed simultaneously and their interrelationship established in detail.
- (3) The shapes of the original grains do not change during MDF and so the deformation substructures can be analyzed in a simple manner. This is in clear contrast to the layered microstructures developed when some of the other SPD methods mentioned above are employed.
- (4) MDF is simply repeated compression and so can be carried out using any conventional testing machine. In this way, a wide range of strain rates and homologous temperatures can be investigated systematically.
- (5) MDF can be applied to large-scale workpieces using a conventional forging machine and without installing any special equipment. It thus has the potential for industrial application.

The relationships between microstructure development and flow stress behavior during MDF have been studied in some detail, principally by the present authors as well as by co-workers in Japan, Russia, China and Canada. The recent studies of metal behavior under SPD conditions will be synthesized in the next section, where special attention will be paid to the links between the microstructural and mechanical observations. Comparisons will also be made with the results obtained using other SPD methods where appropriate.

#### 4.2.2. UFG formation in low SFE materials

Some MDF tests were carried out on pure copper, with pass strains of  $\varepsilon = 0.4$  at 195 K, 300 K and 473 K and a strain rate of  $3 \times 10^{-3} \text{ s}^{-1}$ . The flow stress vs. cumulative strain ( $\sigma$ – $\Sigma\varepsilon$ ) curves obtained in this way are reproduced here in Fig. 28 [46,48,196]. The differences between the flow stresses immediately before unloading and the yield stresses on reloading are relatively small for all the passes applied at 195 K and 300 K. These become distinctly visible in the 473 K tests. This indicates that little static recovery takes place during interrupted compression at and below 300 K [48]. Under these conditions, complete strain accumulation is taking place. Conversely, there is clear evidence for static softening and yield stress reductions when MDF is carried out at 473 K [46]. The general shapes of the flow curve envelopes for the three testing temperatures are indicated by the solid lines in Fig. 28. These show that a steady state of deformation is attained at large strains. Thus it appears that saturation

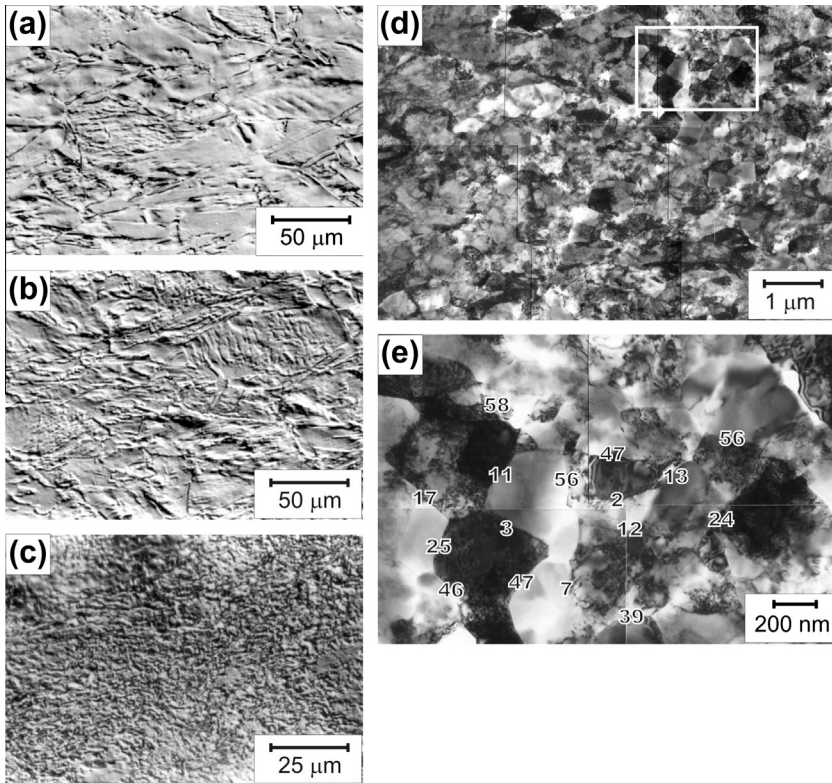


**Fig. 29.** Optical microstructures developed in pure copper during MDF with a pass strain of  $\varepsilon = 0.4$  at 300 K. Cumulative strains are: (a)  $\Sigma\varepsilon = 0.4$ , (b)  $\Sigma\varepsilon = 0.8$  and (c)  $\Sigma\varepsilon = 5.6$ . (d) TEM micrograph of the strain-induced microstructure developed at  $\Sigma\varepsilon = 5.6$ . (e) Enlargement corresponding to the region identified in (d). Numbers indicate the boundary misorientations in degrees [48].

of the flow stress can take place even at cryogenic temperatures as long as deformation is carried out to sufficiently large strains.

Some typical microstructures developed in the copper during MDF at 300 K are displayed in Fig. 29 [48]. It is apparent from this figure that even relatively low strains are sufficient to introduce high densities of microshear bands (MSBs) in the grain interiors. The latter can be seen clearly in Fig. 31. Because of the changes in loading axis, many intersecting MSBs are introduced. When  $\Sigma\varepsilon$  reaches 5.6, very fine roughly equiaxed substructural elements have formed inside the initial grains; these have the appearance of a powdered aggregate (Fig. 29c). The corresponding microstructure observed by transmission electron microscopy (TEM) is represented in Fig. 29d and an enlarged view of Fig. 29d in Fig. 29e. The newly formed grains are enclosed by high angle boundaries (HABs), as shown by the misorientations indicated in Fig. 29e. Some of the grains contain relatively low dislocation densities in their interiors.

In what follows, we use the term microshear band (MSB) to describe a microstructural component that many previous authors have referred to as “deformation bands”. However, the latter sometimes describes a three dimensional *volume* or “band” and sometimes a two dimensional *surface* or boundary. To avoid ambiguity, we employ the expression MSB below to refer to the “boundary” or two dimensional type of deformation band.

It can thus be concluded that the cells and subgrains initially enclosed by low angle boundaries (LABs) and formed at low to moderate strains are gradually transformed into UFGs with HABs at large strains. The changes in some of the copper microstructural parameters after MDF at 300 K are summa-

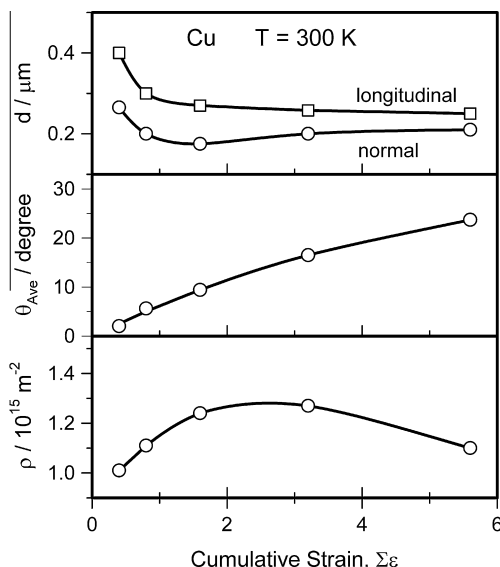


**Fig. 30.** Effect of MDF cumulative strain  $\Sigma\varepsilon$  at 300 K in pure (4N) copper on (i) subgrain and grain size  $d$ , (ii) average sub-boundary misorientation  $\theta_{\text{AV}}$ , and (iii) dislocation density  $\rho$  in the subgrain interiors [48].

rized in Fig. 30 [48]. This shows the dependences of subgrain size,  $d$ , average sub-boundary misorientation,  $\theta_{\text{AV}}$ , and dislocation density,  $\rho$ , in the subgrain interiors on cumulative strain,  $\Sigma\varepsilon$ . The sizes of the elongated subgrains were measured along two directions, i.e., along the long and short intercept directions. Both measures of the subgrain sizes drop rapidly at the start of straining and approach a constant value of about 0.2  $\mu\text{m}$  at high strains. It can also be seen that  $\theta_{\text{AV}}$  increases progressively with strain until it attains values that correspond to high angle boundaries. By contrast,  $\rho$  decreases following a brief rise at moderate strains. It thus appears that the steady state of flow of Fig. 28 is actually the result of two competing processes, namely: (i) strengthening due to the increase in boundary misorientation, and (ii) softening due to the decrease in dislocation density [48].

We turn now to the microstructural observations obtained on the copper MDFed at 195 K. Some typical deformation microstructures are shown in Fig. 31 [196]. After a cumulative strain of 6 (Fig. 31a), the structural changes are characterized by the formation of a network of intersecting MSBs. These are sheared at their points of intersection, leading to the appearance of the so-called S-bands [187]. These features can be considered to be a type of microshear band (MSB), which have been reported to develop in many studies of both cold and hot deformation [196–199]. The concentration of MSBs increases and their width decreases continuously with cumulative strain. After MDF to  $\Sigma\varepsilon = 18$  at 195 K (Fig. 31b), intersecting MSBs have essentially formed in all of the sample, which begins to look like a submicrocrystalline material.

A typical TEM micrograph of the copper MDF to a strain of 6 at 195 K, is shown in Fig. 31c [196]. This microstructure consists of intersecting MSBs, which further intersect the cell substructure, the latter containing a high density of dislocations. The deformation substructures that form far from the MSBs in region (1) in Fig. 31c are not equiaxed but are characterized instead by their elongated shapes. The single spot character of the selected area diffraction pattern of region (1) indicates that the misorientations across the sub-boundaries are relatively small. In region (2) of Fig. 31c, by contrast, the microcrystallites that develop in the intersecting MSB regions are characterized by considerable orientation scatter, as indicated by the ring-like diffraction pattern associated with it.

From the above observations, it can be concluded that strain-induced UFGs develop primarily in association with intersecting MSBs; these are preferential sites for the formation of new grains [196]. The volume fraction of such UFGs increases significantly on further straining to 10, as shown in Fig. 31d. This increase results from an increase in both the number of intersecting MSBs and the

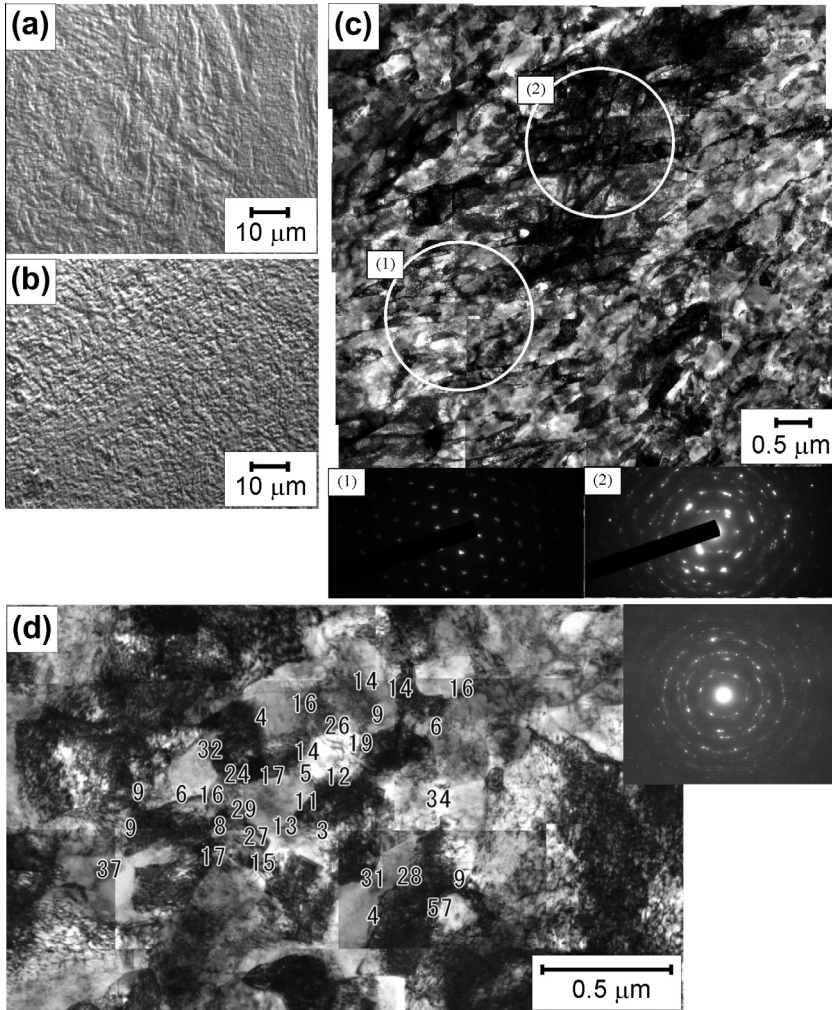


**Fig. 31.** Optical microstructures developed in pure copper during MDF at 195 K to cumulative strains of (a)  $\Sigma\varepsilon = 6$  and (b)  $\Sigma\varepsilon = 18$ . (c) TEM micrograph of the  $\Sigma\varepsilon = 6$  material showing intersecting microshear bands and high dislocation density substructures. Diffraction patterns (1) and (2) were obtained from the selected areas indicated by circles (1) and (2). (d) TEM micrograph of the  $\Sigma\varepsilon = 12$  material showing the absence of substructures outside the UFG regions and the diffraction pattern taken from a 2  $\mu\text{m}$  diameter selected area. The numbers indicate the boundary misorientations in degrees [196].

increase in volume of individual UFGs. The misorientations across the new boundaries also increase continuously with strain. It is of interest to note in Fig. 31d that, at  $\Sigma\varepsilon = 12$ , dislocation-free subgrains are not to be found outside the UFG regions.

The misorientation distributions developed in the copper after repeated MDF at 195 K are presented in Fig. 32a. The distribution at a strain of 1.2 is characterized by a large LAB fraction and by a significant number of HABs with misorientations of about  $60^\circ$ . The latter indicate that deformation twinning took place in the early stages of straining at 195 K [196,200]. The sharp LAB peak decreases in height as the distribution moves towards larger misorientations during deformation; the HAB fractions thus increase with strain. The relations between the average misorientation and the cumulative strain ( $\theta_{AV} - \Sigma\varepsilon$ ) determined at temperatures of 195–473 K are illustrated in Fig. 32b. It should be noted that on processing to relatively small strains of about 2, the average misorientation increases rapidly

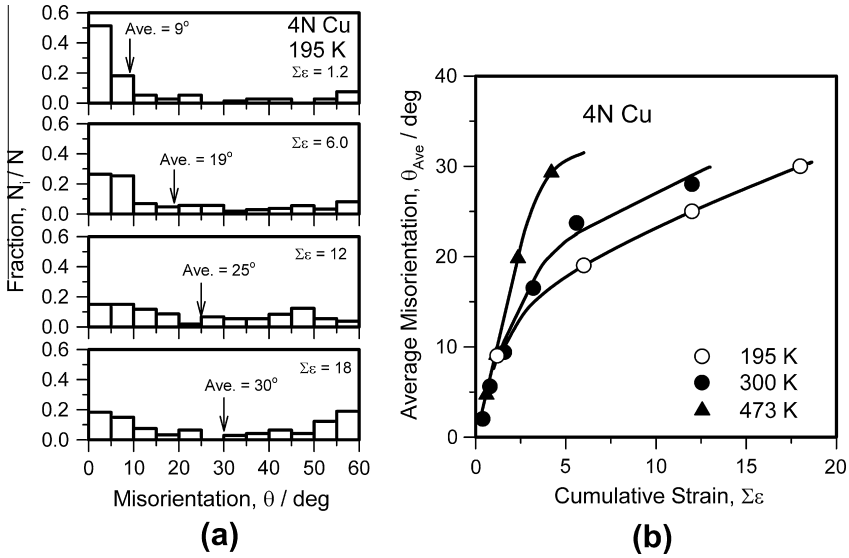


**Fig. 32.** (a) Dependence of the sub-boundary misorientation distribution on cumulative strain in pure copper during MDF at 195 K. (b) Dependence of the average sub-boundary misorientation on cumulative strain in pure copper at 195, 300 and 473 K [196].

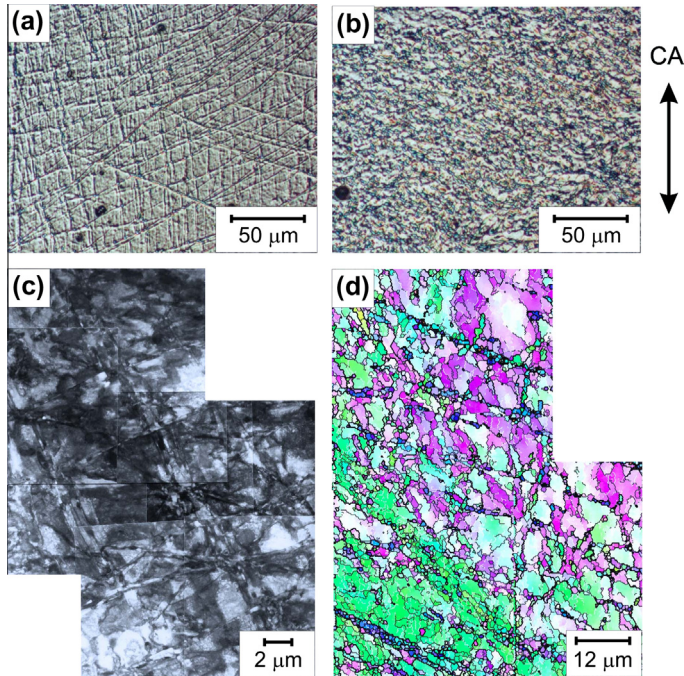


**Fig. 33.** Optical microstructures developed at (a)  $\Sigma\varepsilon = 1.6$  and (b)  $\Sigma\varepsilon = 8.0$  in an Fe–20%Cr alloy during MDF at 773 K. TEM and OIM micrographs of the alloy strained to (c)  $\Sigma\varepsilon = 1.6$  and (d)  $\Sigma\varepsilon = 3.6$  illustrating the intersecting microshear bands and ultrafine grains formed along the bands. HABs with misorientations greater than  $15^\circ$  are delineated by thick black lines, LABs with misorientations in the range  $4\text{--}15^\circ$  by thin black lines and in the range  $2\text{--}4^\circ$  by white lines. The colors in the OIM micrograph have the same definitions as in Fig. 9. The final compression axis in (a) to (d) is vertical [202].

to above  $10^\circ$ , irrespective of the processing temperature. This is a purely strain-induced phenomenon that is associated with the rapid development of MSBs by cold working [48,187,196–199]. The average misorientations that develop at strains above 2, on the other hand, are significantly affected by the processing temperature. Increasing the temperature promotes release of the internal stresses developed during working as well as some dislocation rearrangement next to the intersecting MSBs [201]. It can be concluded that the development of UFG structures is mechanically induced at  $\Sigma\varepsilon < 2$ , whereas it is assisted by thermally activated processes at high cumulative strains. Such thermal activation seems to be effective even when  $T/T_m$  is as low as  $0.14 \sim 0.35$ .

#### 4.2.3. UFG formation in high SFE materials

Some typical deformation microstructures that develop in a Fe–20% Cr alloy at 773 K ( $0.43T_m$ ) are presented in Fig. 33 [202]. The general shape of the flow curve envelope at 773 K is similar to that of the pure copper illustrated in Fig. 28. Many sets of intersecting MSBs have formed in the grain interiors at medium strains and they appear as wavy lines that are sheared by other families of MSBs, as seen in Fig. 33a. The bands are a sign that localized shearing has occurred; in this review, they are considered to be MSBs, as in the case of copper (Fig. 31). The number of MSB families increases with the number of MDF steps; this eventually attains saturation at large strains. A uniform UFG microstructure is present at  $\Sigma\varepsilon = 8$  (Fig. 33b). A typical TEM micrograph of the material at  $\Sigma\varepsilon = 1.6$  is shown in Fig. 33c. This corresponds to the optical one of Fig. 33a. Multiple shearing results in a spatial network of MSBs that separates the microvolumes containing the high density dislocation substructures. At this strain, the UFG microstructure is nearly equiaxed and is characterized by relatively sharp HABs [202]. This is clearly seen in the OIM micrograph of Fig. 33d for  $\Sigma\varepsilon = 3.6$ , which confirms that the intersecting MSBs (as well as the bands themselves) are preferred sites for development of the highly misoriented sub-microcrystalline microstructure. This description is consistent with the observations on the 195 K copper (Fig. 31) presented in the previous section, even though higher SFEs are involved.

It is essential to note here that there is a significant difference between MSBs and conventional (macroscopic) shear bands. The essential features of these two types of bands are illustrated in Fig. 34, where the macroscopic scale of (a) conventional shear bands (schematic) is compared to the microscopic scale of (b) the MSBs developed in the grain interiors of the Fe–20% Cr alloy.

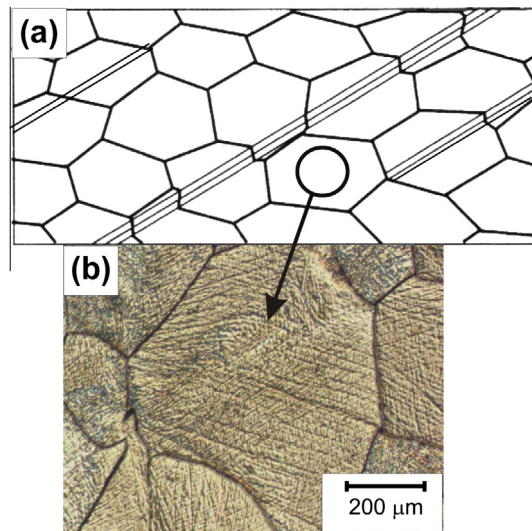


**Fig. 34.** Comparison of (a) schematic drawing of conventional macroscopic shear bands with (b) the microshear bands developed in the grain interiors of the Fe–20% Cr alloy deformed to a cumulative strain of 1.6. The microstructure in (b) is a lower magnification version of Fig. 33a.

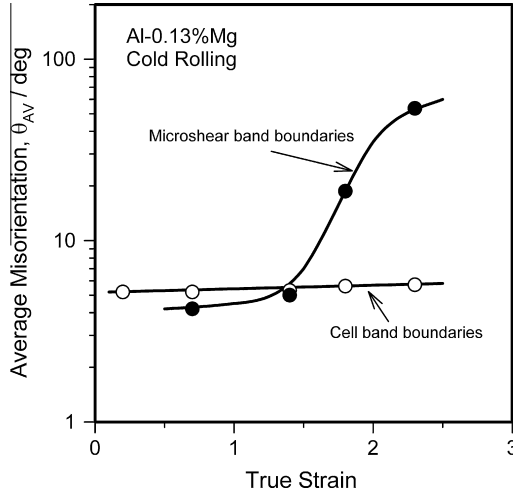


Fig. 35. Dependence of the boundary misorientations of cell bands and microshear bands on total strain in cold rolled Al–0.1% Mg [198].

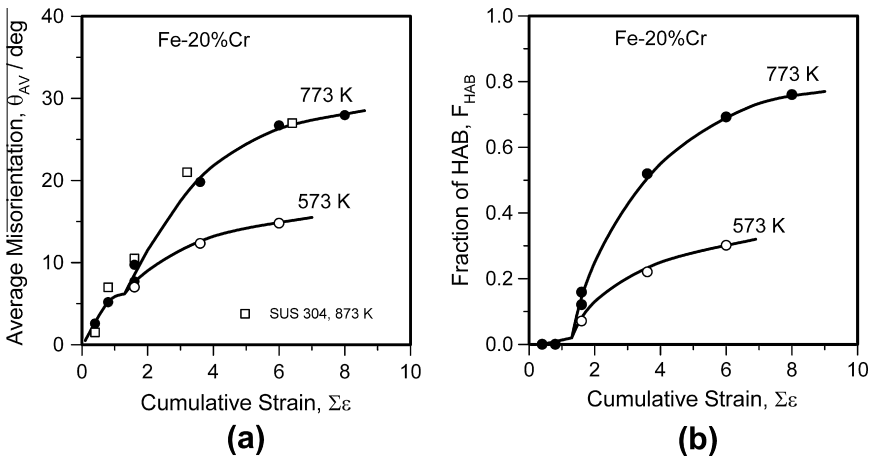
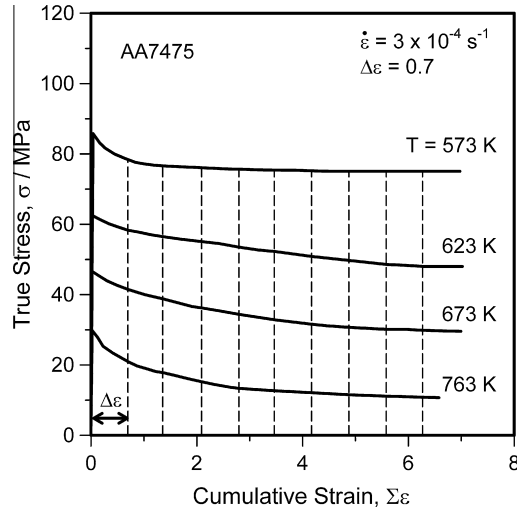


Fig. 36. Dependence of (a) the average sub-boundary and boundary misorientation  $\theta_{AV}$  and (b) fraction of high-angle boundaries (HABs) ( $F_{HAB}$ ) on cumulative strain  $\Sigma\varepsilon$  in the Fe–20% Cr alloy during MDF at 573 K and 773 K [202]. Data for an austenitic steel processed by MDF at 873 K [203] are included in (a) for comparison.

Macroscopic shear bands are usually formed under conditions of negative strain hardening or rate sensitivity. The resulting plastic instabilities and flow localizations pass through several grains and can even extend through the specimen thickness [185]. MSBs, on the other hand, develop *within* grains, although they can extend into neighboring grains as well, as seen in Fig. 34b.

Such microsheading makes available a deformation mode in addition to that of dislocation motion that is particularly useful when plastic deformation is carried out to very large strains. It is well known [203] that multiple slip is required to permit uniform deformation during plastic working. In a similar manner, the operation of multiple microsheading along various directions plays an important role in facilitating homogeneous macroscopic deformation at large strains. The MSBs also participate in the formation of the submicrocrystallites enclosed by the HABs. This view is supported by the



**Fig. 37.** True stress–true strain curves obtained during MDF of AA 7475 at a strain rate of  $3 \times 10^{-4} \text{ s}^{-1}$  in the temperature interval from 573 K to 763 K. Pass strain  $\Delta\epsilon$  is 0.7 [205].

microstructural observations summarized in Fig. 35 obtained on a cold rolled Al–0.1% Mg alloy [198]. The average sub-boundary misorientation and that across the microshear bands (MSBs) are plotted against total applied strain in this diagram. It should be noted that  $\theta_{AV}$  for the cell boundaries is around  $5^\circ$  and remains approximately constant up to strains of 2.5; by contrast, that for the MSB boundaries begins at about  $5^\circ$  at low strains and increases rapidly above strains of around 1.5, reaching values of over  $50^\circ$  at high strains. Thus the  $\theta_{AV}$ – $\epsilon$  relationship for the MSB boundaries very much resembles that for the UFG boundaries that form during the SPD of steels, aluminum alloys, copper, etc. (Figs. 36, 41, 47 and 51). This point will be considered in detail later.

The dependence of the average sub-boundary misorientation on cumulative strain in an Fe–20% Cr alloy subjected to MDF at 573 K and 773 K is presented in Fig. 36 [202]. Also included here is the dependence of the HAB fraction,  $F_{HAB}$ , on strain. Here the data for an austenitic steel processed by MDF at 873 K [204] are included for purposes of comparison. The increases in  $\theta_{AV}$  and  $F_{HAB}$  can be

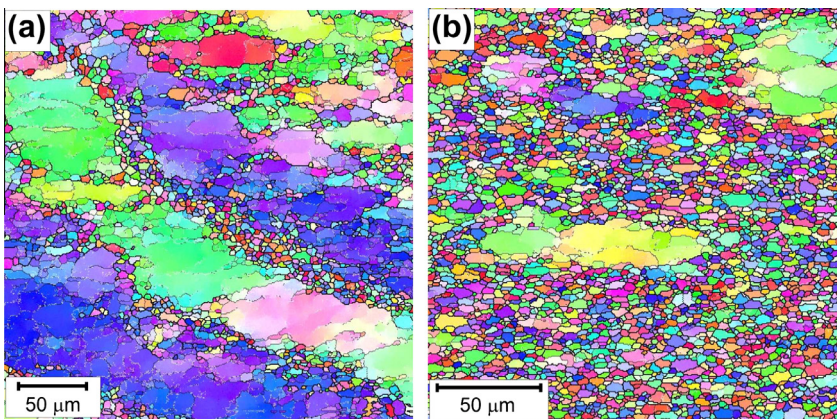


**Fig. 38.** OIM microstructures developed in AA7475 during MDF at 673 K and a strain rate of  $3 \times 10^{-4} \text{ s}^{-1}$ : (a)  $\Sigma\epsilon = 2.8$ ; (b)  $\Sigma\epsilon = 7.0$ . The final compression axis is vertical [205]. The lines and colors have the same definitions as in Fig. 33.

divided into three stages. The first low strain stage is characterized by a rapid rise in  $\theta_{AV}$  followed by a small plateau at about  $5^\circ$ , Fig. 36a. The second stage begins at a critical strain,  $\varepsilon_c$ , of around 1.5; at this point,  $\theta_{AV}$  begins to increase again, accompanied by the frequent development of MSBs. The third stage corresponds to large strains, where  $\theta_{AV}$  approaches its saturation level. Here the UFGs are essentially fully developed.

In Fig. 36b, strain induced HABs only begin to appear at  $\varepsilon > 1.5$ ; then  $F_{HAB}$  approaches its saturation value of about 75 pct at 773 K or 30 pct at 573 K at high strains. It can clearly be seen in Fig. 36 that temperature has little effect on the development kinetics of the UFG microstructure within the first and early second stages. Nevertheless, a decrease in temperature during the third stage of the process retards the rate of misorientation increase significantly.

We now consider the formation of UFG microstructures during the MDF of aluminum alloys. A series of flow stress–cumulative strain ( $\sigma$ – $\Sigma\varepsilon$ ) curves covering 10 consecutive passes is shown in Fig. 37. Here a coarse-grained 0.16% Zr modified aluminum alloy (AA7475) was compressed using pass strains of  $\varepsilon = 0.7$  at temperatures from 573 K to 763 K [205,53]. The flow curve envelope displays a sharp stress peak just after yielding, followed by work softening at all temperatures. This softening takes place up to  $\Sigma\varepsilon \approx 1.5$  at 573 K and  $\Sigma\varepsilon \approx 5$  at 623 K to 763 K, after which the flow curves attain a state of steady flow. When the MDF temperature is increased, the flow stresses decrease rapidly and flow softening becomes more prominent.

Such differences in the flow behavior appear to originate from the different deformation mechanisms operating at different temperatures. Some typical OIM microstructures developed in the AA7475 during MDF at 673 K are presented in Fig. 38 [53]. The UFGs often appear in colonies near sub-boundaries or along the original grain boundaries. Concurrently, banded arrays of sub-boundaries cross the grain interiors and isolated chains of new grains develop along these bands, resulting in grain subdivision. Such deformation bands are similar to the MSBs discussed in the previous sections. It should be noted in particular that the UFGs in Fig. 38 are initially quite heterogeneously distributed

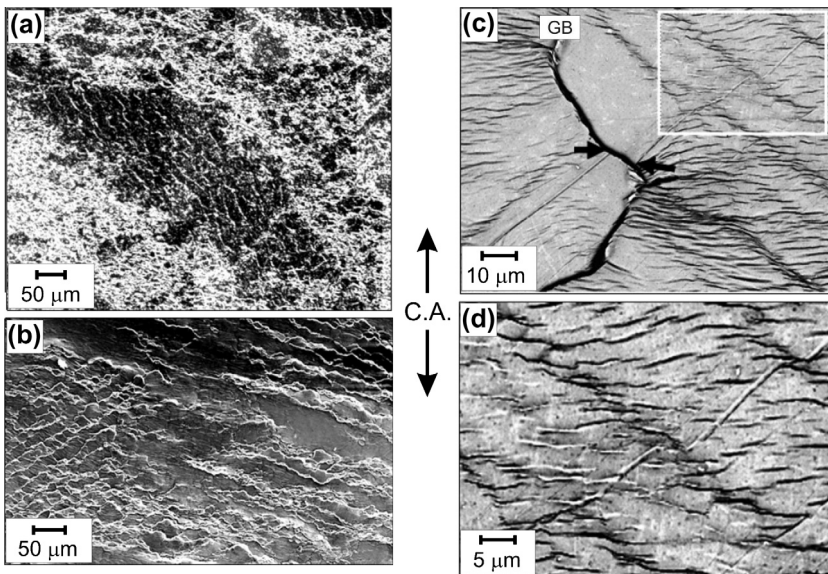


**Fig. 39.** Microstructures developed at a cumulative strain of 1.2 in AA7475 during MDF at 763 K and a strain rate of  $3 \times 10^{-4} \text{ s}^{-1}$ . (a) Polarized light microstructure and (b) SEM micrograph of the mixed region at the upper right in (a). (c) Deformation relief appearing at an additional strain of 0.16 in AA7475 pre-deformed to  $\varepsilon = 1.2$  at 763 K. Arrows indicate the displacement of a marker line along the grain boundary (GB). (d) Enlargement of the portion outlined in (c). The final compression axis (C.A.) is vertical [205].

and do not spread fully through the material even at large strains. Instead, subgrains containing a few MSBs of moderate angle are formed in the remaining parts of the original grains.

The microstructures developed in the AA7475 at a strain of 1.2 after MDF at 763 K are illustrated in Fig. 39. These were determined using polarized optical and SEM microscopy [205]. It is of interest that the MSBs in Fig. 39a are clearly visible using polarized optical microscopy and that the orientations of the deformation bands differ from grain to grain. The microstructures in Fig. 39a and b are composed of the following three components: (i) fully developed fine grains (lower left); (ii) the remainders of the original grains, containing several sets of MSBs (centre); and (iii) mixed structures (upper right). On further MDF, the volume fraction of new grains increases progressively until the initial coarse-grained microstructure is almost fully replaced, although a few relatively coarse grains are still retained [205].

The effects of the MSBs developed in the AA7475 will now be examined more closely. The surface relief produced in a sample initially deformed to  $\Sigma\varepsilon = 1.2$ , unloaded and then further deformed an additional 0.16 is illustrated in Fig. 39c and d. It can be seen in Fig. 39c that plastic deformation occurs heterogeneously and that deformation bands develop in the grain interiors. The shearing taking place along the bands inside the white square in Fig. 39c can be seen more clearly in the enlarged view of Fig. 39d. Here it can be seen that such deformation banding leads to rigid rotation of the scratched markers and so a process akin to kinking or folding can cause a reorientation of the material within these bands [205]. It can be concluded, therefore, that these bands are the equivalents of the MSBs mentioned above (different authors use different terminologies). In this way, the appearance of MSBs in copper, ferritic steel and aluminum alloys, i.e. in cubic metals and alloys, can be seen to lead directly to the formation of UFGs.

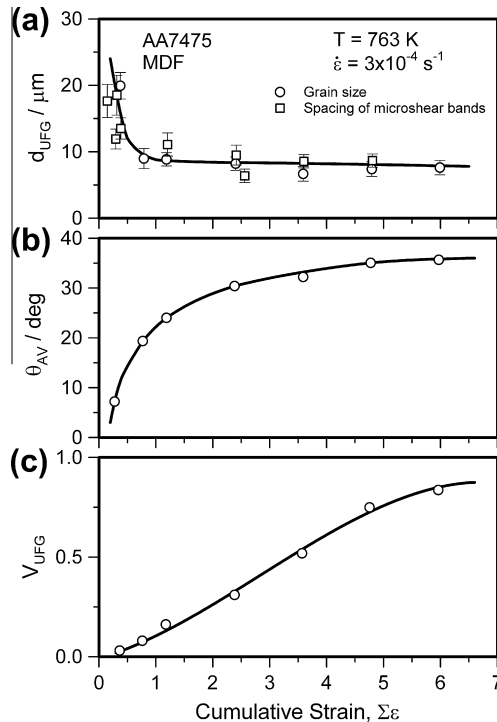


**Fig. 40.** Effect of MDF AA7475 at 763 K on (a) average grain size  $d_{UFG}$  of the new grains and minimum spacing of the microshear bands in the original grains, (b) average sub-boundary misorientation  $\theta_{AV}$  in the fine-grained regions and (c) UFG fraction  $V_{UFG}$  [205].

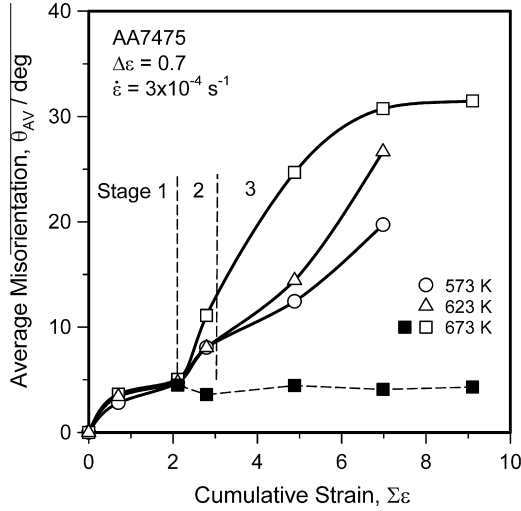


Fig. 41. Strain dependence of the average sub-boundary misorientation  $\theta_{AV}$  developed in AA7475 during MDF at temperatures of 573 K, 623 K and 673 K. Filled symbols at 673 K show the  $\theta_{AV}$  in the remnants of the original grains [53].

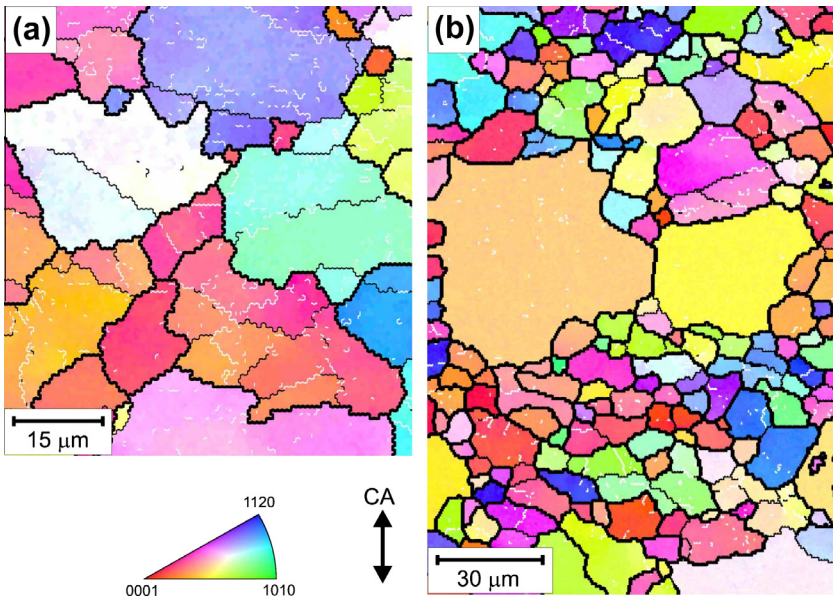
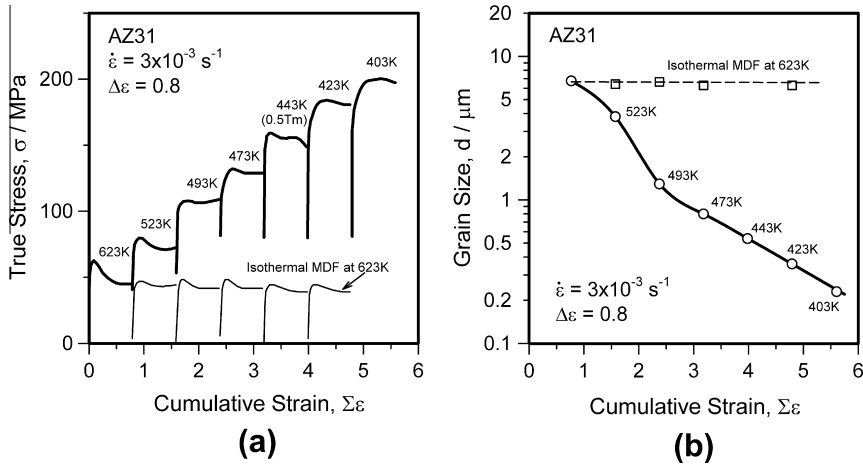


Fig. 42. OIM maps of Mg alloy AZ31 deformed to strains of (a) 0.10 and (b) 0.30 at 673 K and  $3 \times 10^{-3} \text{ s}^{-1}$  [70]. Thin white lines correspond to boundaries of misorientation  $>2^\circ$ , thin black lines  $>4^\circ$ , and thick black lines  $>15^\circ$ . Colors represent the crystallographic orientations indicated in the inverse pole figure.

The changes in some of the microstructural parameters on repeated MDF of the AA7475 at 763 K are summarized in Fig. 40. Here are illustrated the strain dependences of: (a) the average size of UFGs,  $d_{UFG}$ , along with the spacing of MSBs, (b) the average boundary misorientation,  $\theta_{AV}$ , in the UFG regions, and (c) the UFG volume fraction,  $V_{UFG}$  [205]. It is important to note that the sizes of the new grains appearing at medium to large strains are similar to the minimum spacing between MSBs and that this



**Fig. 43.** (a) True stress–true strain curves of Mg alloy AZ31 during MDF at 623 K (thin line) and MDF at temperatures decreasing from 623 K to 403 K (thick line). The pass strain  $\Delta\varepsilon$  was 0.8. (b) Changes in grain size during MDF at 623 K (broken line) and at temperatures decreasing from 623 K to 403 K (solid line) [209].

remains roughly constant at  $\Sigma\varepsilon > 1$ . The values of  $\theta_{AV}$  increase rapidly at low strains and more gradually at moderate and high strains. The volume fraction of new grains  $V_{UFG}$  increases gradually with deformation in the strain range investigated and approaches 0.85. The results of Fig. 40 indicate that the evolution of new grains is closely linked to the formation of MSBs. The gradual flow softening appearing at medium to large strains (see Fig. 37) takes place concurrently with the gradual development of UFG structures and is probably associated with the loss of dislocations in this strain range [205].

The effect of temperature on the  $\theta_{AV}$ – $\Sigma\varepsilon$  curves for the AA7475 is represented by the solid lines in Fig. 41 [53]. The values of  $\theta_{AV}$  in the remnants of the original grains present at high strains are indicated by the broken lines in the same figure. These  $\theta_{AV}$ – $\Sigma\varepsilon$  curves can be divided into three stages; i.e. an incubation period for the formation of new grains (stage 1), a rapid increase in  $\theta_{AV}$  accompanied by the development of MSBs and new grains (stage 2), and the continuous spreading of MSBs and UFGs over the whole volume (stage 3). It is important to note that the values of  $\theta_{AV}$  in stage 1 and the sudden increase in stage 2 are not affected by temperature. By contrast, in stage 3,  $\theta_{AV}$  increases at a higher and higher rate as the temperature is increased. Such results are similar to those described above for the Fe–20% Cr alloy (Fig. 36). Note that the values of  $\theta_{AV}$  developed in stage 1 are similar to those associated with the grain remnants at large strains; these hover around  $5^\circ$ , indicating that some conventional subgrains with LABs introduced in stage 1 remain stable during deformation. These do not transform into UFGs with HABs even at large strains, a phenomenon that has not been explained to date. The presence of low-misorientation dislocation substructures as well as fully formed grains after SPD unambiguously testifies to the heterogeneous development of UFGs. The formation of these grains thus necessarily involves the inhomogeneous distribution of dislocations, whether these are in MSBs or in the vicinity of grain boundaries, as will be discussed in detail in Section 4.3.2.

We turn now to UFG formation and the mechanisms operating in magnesium (Mg) alloys, that is, in hexagonal closed packed materials. Some typical OIM micrographs for Mg alloy AZ31 compressed to strains of 0.1 and 0.3 at 673 K are presented in Fig. 42 [70]. The  $\sigma$ – $\varepsilon$  curve displays strain softening, with a smooth stress peak at  $\varepsilon_p = 0.12$ , followed by steady-state flow at  $\varepsilon > 0.5$  (see Fig. 43a). It can be seen in Fig. 42a that several initial grains have become fragmented by kink bands and that substantial misorientations have already developed in the grain interiors at  $\varepsilon = 0.10$ ; fine grains have also formed along the corrugated grain boundaries. These new boundaries have evolved from kink bands as well as microbands [4,187,53,206].

A typical OIM micrograph for a strain of 0.3 is depicted in Fig. 42b. Here, in the strain range beyond  $\epsilon_p$ , the fraction of new grains increases rapidly until a new equiaxed microstructure finally forms throughout the material at  $\epsilon > 0.5$ . It can be seen that the crystal orientations are almost randomly distributed while some coarse grains are retained within the fine grained regions. It should be noted that the sizes of the new grains are similar to those of the regions fragmented by the kink bands in Fig. 42a and that they do not change during further deformation to high strains [70]. This indicates that each fragmented region initially surrounded by low to medium angle boundaries gradually transforms *in situ* into grains surrounded by HABs and that the latter do not grow during further deformation. Thus it can be seen that the evolution of new grains in Mg alloys results from a series of strain-induced reactions; that is, from kinking of the original grains followed by the *in situ* formation of UFGs even at  $\epsilon < 1$ .

The effect of decreasing temperature conditions on the process of grain refinement during MDF of the Mg alloy AZ31 is illustrated in Fig. 43 [207]. Some typical true stress–cumulative strain ( $\sigma$ – $\Sigma\epsilon$ ) curves are presented in Fig. 43a, while the corresponding grain size changes taking place are shown in Fig. 43b. During MDF under decreasing temperature conditions, the flow stress increases and concurrently the grain size decreases drastically, leading to the development of 0.23  $\mu\text{m}$  UFGs after 7 compression passes to  $\Sigma\epsilon = 5.6$  at 403 K (solid line). During isothermal MDF at 623 K, on the other hand, the flow stresses do not change and the average grain size remains almost constant at about 6.7  $\mu\text{m}$  at strains up to  $\Sigma\epsilon = 4.8$  (broken line). Such excellent grain refinement during decreasing temperature MDF has also been observed in Mg alloy AZ61 [208]. Such UFG Mg alloys, with much improved mechanical properties and workability, have been studied in detail [207–210].

#### 4.3. Mechanisms of strain-induced UFG formation during SPD

##### 4.3.1. Models of strain-induced UFG formation

Several mechanisms for the formation of UFGs during SPD have been proposed and discussed. One of the practical applications of UFGed metals and alloys is subsequent forming by superplastic methods, as a critical condition for superplasticity is the presence of an UFG microstructure. This can be achieved in almost all metallic materials [211]. A widely used superplastic forming method involves

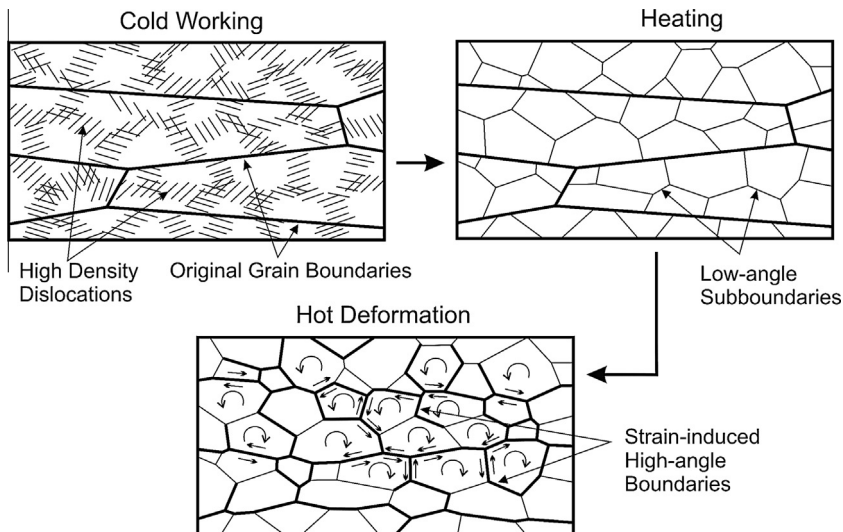


**Fig. 44.** Schematic illustration of UFG development during hot deformation of prior cold and warm worked alloys. The subgrain rotations taking place are accompanied by sliding along the grain boundaries during hot deformation at low strain rates [212,213].

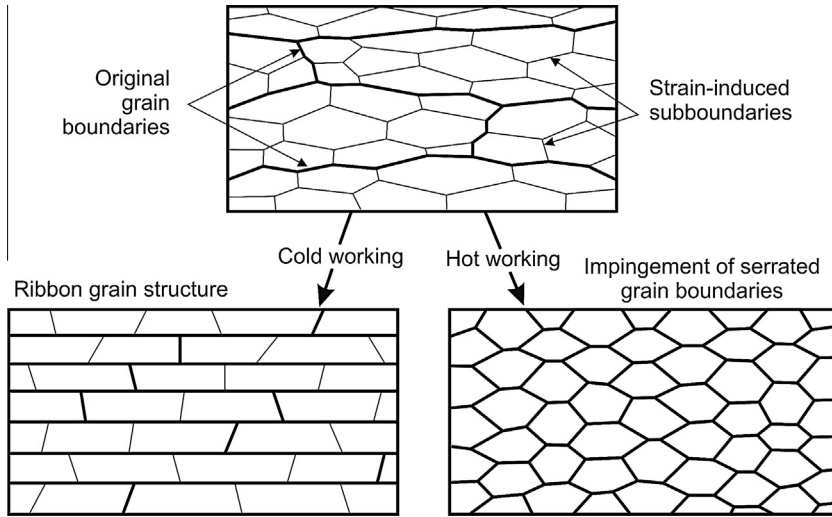


**Fig. 45.** Schematic illustration of UFG development during unidirectional plastic working to large strains. Directional ribbon grain structures form through a grain subdivision process at ambient temperature or through the pinch-off of serrations (i.e. geometric DRX) at elevated temperatures [168,214].

prior cold and/or warm working followed by hot deformation under appropriate conditions [212,213]. Such an approach has been successfully realized in high SFE materials such as the aluminum alloys. The mechanism of UFG formation in this case involves the gradual transformation of dislocation substructures into UFGs with HABs, as shown schematically in Fig. 44. The prior cold or warm working introduces a high density of dislocations, which transform into polygonized subgrains upon heating to the processing temperature. During subsequent hot deformation, progressive subgrain rotation takes place, followed by the transformation of subgrains with LABs into UFGs with HABs. Since these UFGs result from continuous reactions during deformation, such sequences of structural change have been referred to as continuous dynamic recrystallization, i.e. cDRX.

It should be noted that UFG structures in high SFE materials can be produced by warm to hot deformation under certain conditions without previous cold working. Following the formation of dislocation sub-boundaries with low misorientations, the new grains develop as a result of increasing the density of dislocations trapped by the sub-boundaries during deformation, leading to the gradual transformation of LABs into HABs; this is the essence of cDRX [25–29,32–37]. Gourdet and Montheillet have developed such a cDRX model [33,36] by first assuming the presence of a homogeneous distribution of dislocations, which then evolves as a result of DRV. During this process, the densities of both the interior as well as sub-boundary dislocations increase with continued straining. This model links the flow stress to some of the microstructural parameters and is able to predict the evolution of crystallite size and dislocation density with strain under various deformation conditions.

Another mechanism of structural change involves severe cold rolling at ambient temperature [168]. This produces pancake-shaped grains that have been elongated along the rolling direction; concurrently, high dislocation density substructures are formed that subsequently develop into new grains. These events culminate in the formation of UFGs that are finer at lower temperatures. Further deformation results in the development of lamellar microstructures, known as ribbon grain structures, where both the original as well as the strain-induced HABs are rotated into the rolling plane [168] (see Fig. 45). The HAB spacing decreases with strain, approaching the cell/subgrain size at large strains. This resembles the mechanism known as geometric DRX, which was originally proposed to account for the appearance of new grains in aluminum alloys during large strain rolling and torsion at elevated temperatures [168,214]. The closely spaced HABs of the pancake-shaped grains frequently become serrated during deformation and approach each other at high strains. Eventually, some serrations

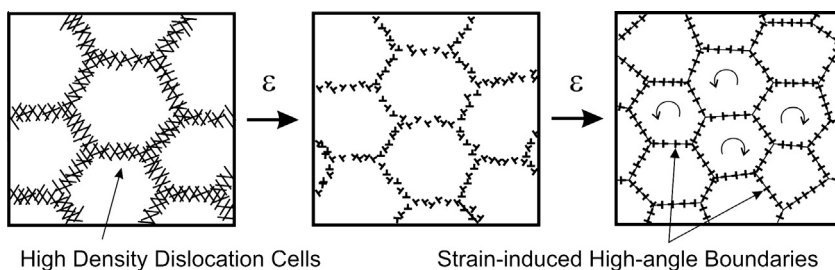


**Fig. 46.** Schematic model of UFG formation from cell structures based on TEM observations of the microstructures developed under SPD conditions. The misorientations between the sub-boundaries increase with strain and approach those of HABs at large strains [30,171,186,190].

meet and pinch off the elongated grains, resulting in an UFG microstructure composed of a mixture of HABs and LABs (Fig. 45).

The strain-induced HABs that develop during cold working can generally be characterized as geometrically necessary boundaries. The evolution of these boundaries is, by definition, associated with differences in the operating slip systems within individual regions of particular grains that result in subdivision of the grain into microvolumes. The various microvolumes then experience different rotations during plastic deformation. Hughes and Hansen have shown that different parts within an initial grain rotate towards different stable end orientations [215]. In this way, the spatial and misorientation distributions of the strain-induced HABs are determined by the orientations and rotations of the individual microvolumes. The rotation parameters of the individual microvolumes depend, in turn, on their orientations with respect to the current stress state together with the effects of the constraints imposed on them by their neighboring microvolumes.

The nucleation mechanism for strain-induced boundaries has also been treated in terms of junction disclinations [186,216,217]. A dislocation flux across any faceted grain boundary in the course of plastic deformation leads to accumulation of the grain boundary misfit dislocations that are required to accommodate the plastic shear and rotation associated with the strain incompatibilities. The distribution of these misfit dislocations is generally different at different boundary facets and depends on the crystallographic orientation of each grain with respect to the boundary plane. Thus, differences in the boundary misorientations at various facets create rotation type defects, i.e., junction disclinations, the magnitudes of which increase with strain. The internal stresses associated with the junction disclinations can be released by the formation of new interfaces. According to this view, when the internal stresses generated by the junction disclinations exceed a critical value, secondary slip systems are activated and the subsequent rearrangement of the stored dislocations results in the formation of new strain-induced sub-boundaries. In this way, the misorientations associated with strain-induced boundaries are in direct proportion to the strain applied.

Early studies of SPD carried out mainly by HPT indicate that the UFGs appearing at large strains have replaced the cells and subgrains formed at low to moderate strains [30,172,186,190]. The schematic drawing presented in Fig. 46 illustrates the sequence of microstructural changes leading to the presence of UFGs at large strains. The UFG structures are considered to result from the gradual transformation of the preceding cellular substructure. The dislocation density in the cell walls increases progressively under SPD conditions. Dislocations with Burgers vectors lying in the boundary plane are responsible for grain boundary sliding and shearing, while other dislocations provide the increase in boundary misorientation in accordance with their combined Burgers vectors. In this way, the sub-boundary misorientations increase with strain and approach values typical of conventional HABs at sufficiently large strains.

Numerous analyses of UFG formation have also been carried out based on dislocation density models [218–222]. Estrin and Vinogradov have recently reviewed these models [223]. Following Mughrabi's approach [224], which considers deformation substructures as composite crystals consisting of hard dislocation walls of high dislocation density and soft cell interiors of low dislocation density, flow

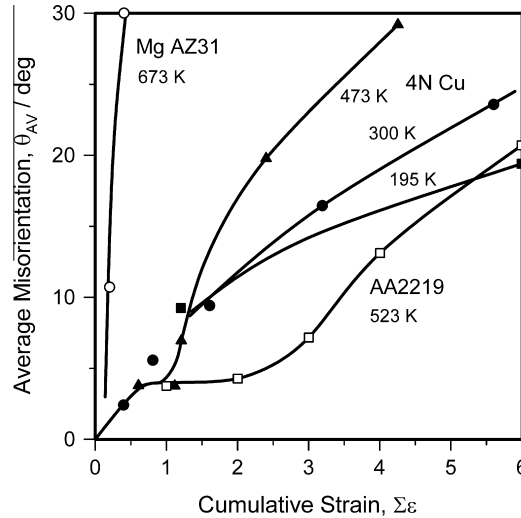


Fig. 47. Dependence of the average sub-boundary misorientation on cumulative strain in Al alloy 2219 ECAP at 523 K [226], pure Cu MDF at 195 K, 300 K and 473 K [46,48,196], and Mg alloy AZ31 compressed at 673 K [70].

curves can be predicted for large strain cold deformation. These models are based on the common assumption that strain hardening during cold working is associated with an increase in the dislocation density. The square root of the latter is, in turn, inversely proportional to the subgrain size. The models proposed to date adequately describe the generally observed decrease in hardening rate towards zero at large strains.

An interesting grain fragmentation model has recently been proposed by Toth et al. [225]. On the basis of numerous experimental observations, these authors have taken the large grain rotations occurring during SPD into account. These rotations are not uniform within the grains because of the influence of the grain boundaries and neighbors. As a result, the crystallographic orientations that develop in the regions near the boundaries differ from those associated with the grain interiors. This difference increases progressively with strain. According to these authors [225], the differences in crystallographic orientation between different regions within a grain are accommodated by the geometrically necessary dislocations that are introduced to provide the required lattice curvature. Then, increases in the density of the curvature-providing dislocations result in the appearance of new strain-induced boundaries.

This picture of grain fragmentation based on the introduction of lattice curvature is able to predict one of the most important features of microstructural evolution during SPD, namely the development of strain-induced boundaries, which are essentially the geometrically necessary ones. This bears some similarity to the earlier dislocation density-based models, in which the formation of UFG is described in terms of the gradual and homogeneous transformation of dislocation cell walls into HABs during SPD. Nevertheless, one difference between the two types of model is that, in that of Toth et al. [225], the new grains develop predominantly in the vicinity of grain boundaries, where the constraints are higher, while in that of Gourdet and Montheillet [33,36], the new grains are distributed relatively homogeneously. In spite of the simplified mechanism for new boundary formation and the adoption of arbitrarily selected parameters such as the boundary friction to quantify the effect of the boundaries on the lattice rotation, the lattice curvature-based model can provide a quantitative description of the deformation behavior during SPD, i.e., it can predict the stress–strain curve, the extent of grain refinement, the texture evolution, etc.

In summary, during SPD, the low misorientation sub-boundaries introduced at low strains transform into grain boundaries with HABs; this finally leads to a full UFG microstructure at large strains

[30,33,168,172,190]. In these subgrain/dislocation density-based models, particularly applicable to cubic materials, the new grains evolve homogeneously from the subgrains formed at low strains. This process is therefore considered to be a ‘single step’ reaction and not to involve nucleation and growth, a two-step process. Such models, however, are unable to account for all of the experimental results described in Section 4.2. For example, the following ‘sub-steps’ can be distinguished (see Figs. 36, 41, 47 and 51), which will be considered in more detail in the next section:

- (1) The UFGs develop partly heterogeneously, through the formation of deformation bands and kink bands (Figs. 29, 31, 33, 38, 39 and 42), and partly homogeneously; the latter process does not extend throughout the material even at large strains (Figs. 36, 38, 40 and 42).
- (2) Some of the subgrains developed at low strains and delineated by LABs exist stably and do not transform into UFGs with HABs in remnants of the original grains, even at large strains (Fig. 41).
- (3) The UFGs formed at low temperatures are often finer than the subgrains that first appear in the microstructure, as discussed in more detail later (Fig. 49).

#### 4.3.2. A new model for the strain-induced formation of UFGs

The continuous increase in misorientation between subgrains during SPD is an essential feature of the strain-induced formation of UFGs, as discussed above. The kinetics of this process can be described using the dependence of the sub-boundary misorientation  $\theta_{AV}$  on the total accumulated strain  $\Sigma\varepsilon$ . The  $\theta_{AV}$ - $\Sigma\varepsilon$  relationships determined on Al alloy 2219 ECAP at 523 K [226], pure Cu MDF at 195 K to 473 K [46,48,196], and Mg alloy AZ31 compressed at 673 K [70] are illustrated in Fig. 47. The important results that can be deduced from this figure can be summarized as follows:

- (1)  $\theta_{AV}$ - $\Sigma\varepsilon$  curves can be divided into three stages. The first is characterized by a rapid rise in  $\theta_{AV}$  followed by a small plateau at about  $5^\circ$ . In the second stage, the misorientations begin to increase rapidly again beyond a critical strain,  $\varepsilon_c$ . The third stage corresponds to large strains, at which  $\theta_{AV}$  approaches its saturation level (Figs. 32, 36, 40 and 41). The HAB fraction vs. cumulative strain ( $F_{HAB}$ - $\Sigma\varepsilon$ ) curves can also be subdivided into three stages, which correspond to those of the  $\theta_{AV}$ - $\Sigma\varepsilon$  curves (Fig. 36).
- (2) MSBs and kink bands begin to appear at  $\varepsilon_c$  and accompany the formation of UFGs along the bands during second stage deformation (Figs. 33 and 38). Finally, in the third stage, the UFG microstructure spreads through the whole volume accompanied by the further formation of MSBs. The average size of the UFGs remains essentially constant during this process.
- (3) The process of forming UFGs during SPD is similar, whether deformation takes place by MDF, ECAP, or other methods.

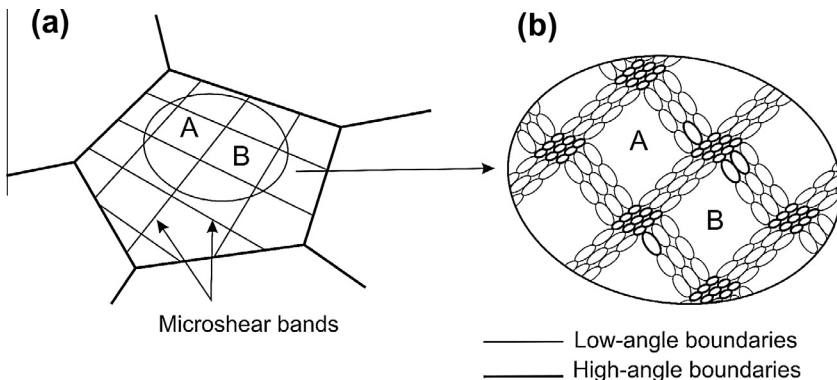


**Fig. 48.** Schematic drawing of the development of (a) microshear bands at low strains and (b) the subsequent formation of new grains at their intersections and along the bands at sufficiently large strains [202].

- (4) The critical strain  $\varepsilon_c$  and the kinetics of UFG formation clearly depend on the material tested. It can be seen from Fig. 47 that the values of  $\varepsilon_c$  are about 1 in Cu, 1.5 in ferritic steel (Fig. 36) and over 2 in an Al alloy. All these are cubic materials. The  $\varepsilon_c$  for Mg alloy AZ31, on the other hand, is far below 1, i.e. around 0.1, and the kinetics of UFG formation in this case are the most rapid among the materials shown in Fig. 47. This difference can be attributed to the hcp nature of these alloys.
- (5) The effect of temperature on the kinetics of grain refinement is negligible in the first and early second stages of this process. The third stage kinetics, on the other hand, are retarded when the deformation temperature is decreased. As a result, the saturation value of  $\theta_{AV}$  at large strains is lower for cold than for warm or hot deformation, as seen in Figs. 32 and 36.

In keeping with the results summarized above, the present authors have proposed a model for strain-induced UFG formation based on the evolution of MSBs followed by grain fragmentation. This is particularly applicable to cubic materials and can be referred to as the MSB model, illustrated in Fig. 48 [202]. In the first stage of the process, i.e.  $0 < \varepsilon < \varepsilon_c$ , the dislocations introduced by the deformation are arranged in cellular substructures. The formation of MSBs in the second stage of the process causes fragmentation of the original grains leading to a rapid increase in  $\theta_{AV}$ . The orientations of adjacent domains (e.g. A and B in Fig. 48), are not significantly changed by microshearing at this stage. However, on further deformation, the number of MSBs and the boundary misorientations increase rapidly, as shown in Fig. 35. Then, when the latter become large enough, UFGs develop first at the intersections and subsequently along the MSBs [50,202]. In this way, the multiple shearing along various directions introduced by MDF accelerates the formation of UFGs in the grain interiors, leading to the propagation of the equiaxed microstructure through the entire volume. It can be concluded, therefore, that the condition for the formation of UFG microstructures in cubic materials is the development of a high density of MSBs throughout the material (Figs. 24, 31 and 33). This can only be achieved by means of SPD to large strains.

In Mg alloys, on the other hand, MSBs are replaced by kink bands, which develop in the grain interiors at much lower strains, e.g. 0.1. These fragmented regions become new grains even at strains below 1 (Figs. 42 and 43). Here the MSBs in the diagram of Fig. 48a are replaced by kink bands and new grains appear even after light deformations. Thus grain formation results from the introduction of kink bands.

According to the model of Fig. 48, the dynamic formation of UFGs during SPD results from a series of continuous strain-induced reactions. First there is the development of MSBs (or kink bands in hcp materials); this is followed by grain fragmentation and the formation of new grains. The overall process corresponds to continuous DRX (cDRX) and is actually a one-step phenomenon. Although, new grains are first formed heterogeneously, they spread homogeneously through most of the remaining volume at large strains. The average size of the UFGs that appear in this way does not change during SPD. By contrast, conventional dDRX involves a two-step process, i.e. the nucleation of new grains surrounded by HABs followed by their growth by means of long-range migration, as described in Section 3. It should be noted that in cDRX the new grain structure does not completely replace the original microstructure even at very large strains (Figs. 36, 40 and 41). This appears to be because certain grain orientations are resistant to the development of MSBs and kink bands (Figs. 38 and 42).

The mechanism of UFG formation involves the generation of geometrically necessary boundaries in the early stages of SPD [44,187,188,197–199]. These appear between domains of the original grains where the combination of operative slip systems differs somewhat. On further deformation, the misorientations increase rapidly due to the continued occurrence of dislocation slip within the individual domains. In contrast to previous studies of grain subdivision, the mechanism of UFG formation presented here considers MSBs as planar regions of localized shearing that are formed in response to the concurrent operation of different sets of slip systems. The microshearing eventually results in the development of a number of HABs (see Fig. 31c). The effect of the constraints imposed by grain neighbors on the formation of GNBs may be similar to that in the lattice curvature model proposed by Toth and co-workers [225,227]. In the second stage of UFG formation, the latter appear primarily at MSBs intersections, where the intersecting boundaries form microcrystallites. This is accompanied by the transformation of the sub-boundaries into grain boundaries. Following UFG formation at MSB

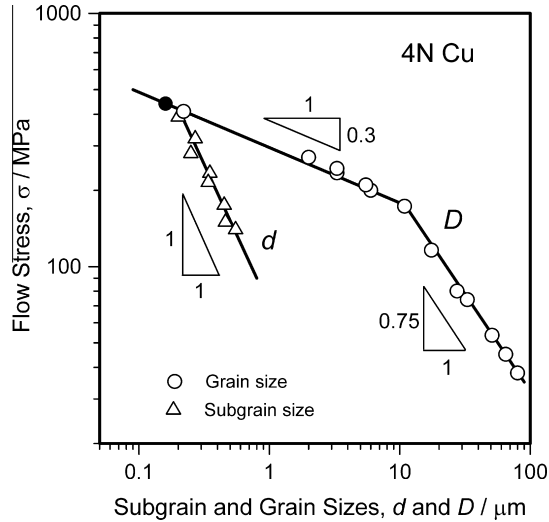


**Fig. 49.** Relationships between flow stress and dynamic grain or subgrain size in pure copper deformed to large strains over a wide temperature range [46,48]. The 195 K result [196] is indicated by a solid mark.

intersections, other UFGs develop along the MSBs and then spread throughout the sample on further straining. Since the development of UFGs in the third stage is closely associated with dynamic recovery, the kinetics of UFG formation are accelerated by an increase in deformation temperature.

#### 4.4. Effect of temperature and strain rate on the formation of strain-induced UFGs

##### 4.4.1. Low SFE materials

The relations between flow stress and dynamic grain and subgrain size,  $D$  and  $d$ , in pure Cu are summarized in Fig. 49 [46,48,196]. These are commonly expressed as power law functions of the flow stress  $\sigma$  with a grain size exponent of about  $-0.3$  in the region where  $\sigma > 200$  MPa and of  $-0.75$  when  $\sigma < 200$  MPa. Over both ranges, the subgrain size exponent is  $-1$ . When  $\sigma < 200$  MPa, conventional dDRX takes place during deformation above  $0.5T_m$  and new grains surrounded by HABS develop as a result of nucleation by grain boundary bulging followed by grain growth. The resulting grain size is determined by the dynamic equilibrium established between the nucleation rate and the HAB migration rate (see Fig. 15). Under such conditions, the grain size is much larger than the subgrain size because of the long-range migration of HABS until impingement.

By contrast, when  $\sigma > 200$  MPa, i.e. during deformation at temperatures below  $0.5T_m$ , the grain boundaries no longer have the ability to migrate. Under these conditions, the new grains are produced by a series of strain-induced reactions, that is as a result of cDRX, as discussed in detail in Section 4.2. As the grain size generally cannot be finer than the subgrain size, there is a limit to the amount of grain refinement that can be achieved during cold working. This limit is indicated by the full circle in Fig. 49, applicable to processing Cu at 195 K. It appears that sub-boundaries cannot form in grains less than 200 nm in diameter because of the strong elastic interactions between dislocations [39,195,196,228]. For example, there are no cells within the UFGs produced at  $\Sigma\varepsilon = 12$  at 195 K, while subgrains clearly develop at  $\Sigma\varepsilon = 6$ , as can be seen in Figs. 31c and 31d.

The relations between the normalized steady state stress  $\sigma/G$  ( $G$  is the shear modulus) and the grain size  $D$  and subgrain size  $d$  over a wide range of deformation conditions are summarized in Fig. 50. These results apply particularly to low SFE metals and alloys, i.e. copper [46,48,196] (Fig. 49), 304 stainless steel [50], Ni–20% Cr alloy [229] and Ni–30% Fe alloy [230]. It should be noted in Fig. 50 that the  $\sigma/G$  vs.  $D$  relationship can be expressed by a power law function with grain size exponents of about  $-0.3$  or  $-0.75$  depending on whether  $\sigma/G$  is greater or less than  $5(\pm 1) \times 10^{-3}$ .

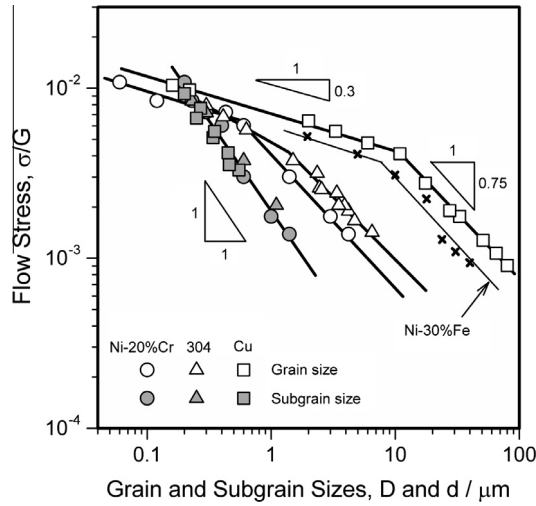


**Fig. 50.** Relationships between normalized flow stress  $\sigma/G$  and DRX grain size  $D$  or subgrain size  $d$  in 304 stainless steel [50], Ni–20% Cr alloy [229], Ni–30% Fe alloy [230] and pure Cu (Fig. 49).

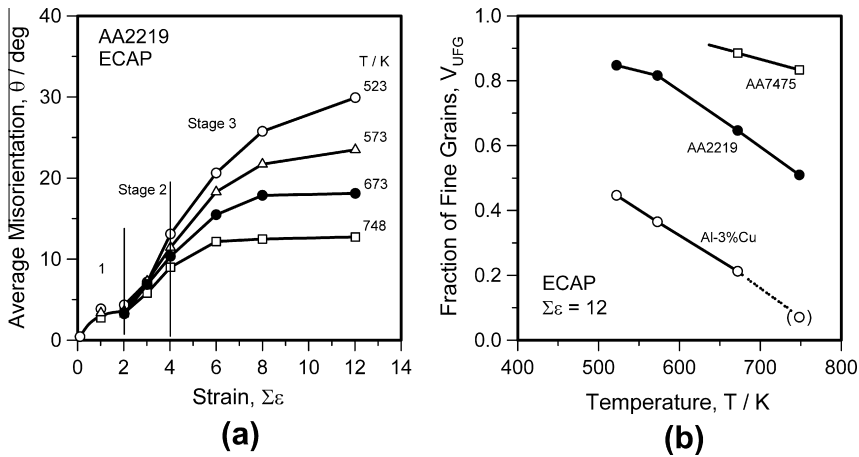


**Fig. 51.** (a) Dependence of average sub-boundary misorientation  $\theta_{AV}$  on accumulated strain in AA2219 after repeated ECAP at temperatures from 523 K to 748 K [52,226]. (b) Temperature dependence of the volume fraction of UFGs,  $V_{UFG}$ , in Al–3% Cu and AA2219 deformed to  $\Sigma\epsilon = 12$  by ECAP [52,231] and AA7475 deformed to  $\Sigma\epsilon = 9$  by MDF [53].

The  $\sigma/G$  vs.  $d$  relationship, on the other hand, has a unique exponent of about  $-1$  for all materials over the entire range tested. A point of interest is that in the transition region in the vicinity of  $\sigma/G \approx 5(\pm 1) \times 10^{-3}$ , mixed grain structures are observed; this is because both cDRX and dDRX are operating concurrently.

4.4.2. High SFE materials

In high SFE materials, only cDRX can take place, accompanied by dynamic recovery; this holds over the entire processing temperature range, from  $T/T_m$  near 0 to 1. Some misorientation angle vs. cumulative strain ( $\theta_{AV} - \Sigma\epsilon$ ) curves for strain-induced boundaries in an aluminum alloy are presented in Fig. 51a. Here a coarse-grained AA2219 was deformed by ECAP at temperatures from 523 to 748 K

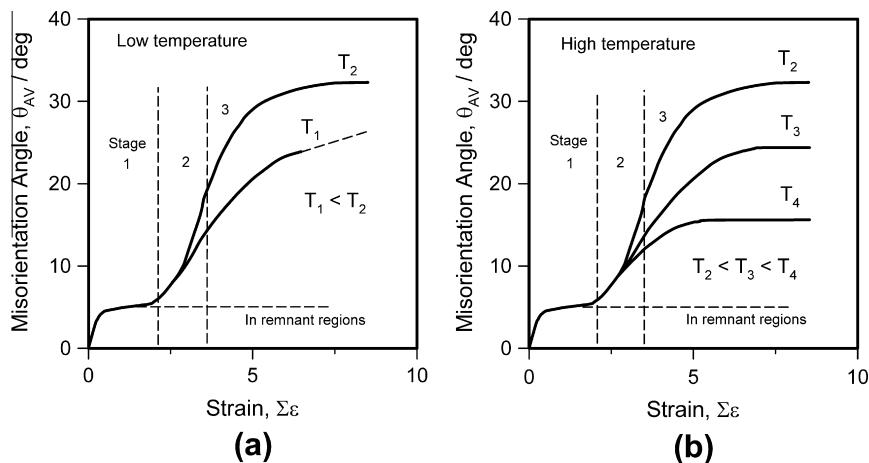


**Fig. 52.** Schematic drawings comparing the dependences on cumulative strain of the sub-boundary misorientation  $\theta_{AV}$ , developed during SPD under two conditions: (a) at relatively low temperatures in highly alloyed materials containing fine particles, and (b) at temperatures above  $0.5T_m$  in lightly alloyed materials. The values of  $\theta_{AV}$  in the interiors of the initial grains are indicated by the broken line [232].

[52,226]. The  $\theta_{AV}$ - $\Sigma\varepsilon$  curves can be divided into three stages in a manner somewhat similar to the MDF curves of the ferritic steel (Fig. 36), AA7475 (Fig. 41) and Cu (Fig. 47) presented above. Note, however, that the effect of temperature on the  $\theta_{AV}$ - $\Sigma\varepsilon$  relationship for the AA2219 differs from that described above for the latter materials, i.e. the ferritic steel, AA7475 and Cu. That is,  $\theta_{AV}$  increases with temperature in the latter materials, while it decreases with temperatures in the AA2219 in Fig. 51a. Such a different behavior in the process of UFG formation will be discussed in detail below.

As shown in Fig. 40 above, the volume fraction of UFGs,  $V_{UFG}$ , increases during SPD, approaching saturation in stage 3 at large strains. Here, the temperature dependences of  $V_{UFG}$  in stage 3 are illustrated in Fig. 51b for three aluminum alloys, i.e. AA2219 [52], AA7475 [53] and a binary alloy Al-3% Cu [231]. It can be seen that these  $V_{UFG}$  vs.  $T$  curves are clearly influenced by the chemical compositions of the alloys tested. The main compositions were as follows: (i) 6.4Cu, 0.3Mn, 0.18Cr, 0.19Zr, 0.06Fe in AA2219, (ii) 6.04Zn, 2.46Mg, 1.77Cu, 0.23Cr, 0.16Zr, 0.04Fe in AA7475, and (iii) a binary Al-3% Cu (all in wt.%). It can readily be understood that the fine particles in commercial alloys act to retard or even prevent any relaxation of the strain gradients introduced during SPD. This results in the rapid increase in misorientation of the sub-boundaries and MSBs and the formation of UFGs with HABs even at temperatures above  $0.5T_m$ . This also accounts for the higher misorientations and greater volume fractions of UFGs in the commercial aluminum alloys than in a pure Al-3% Cu alloy at the same deformation temperature, as seen in Fig. 51b.

The experimental results reviewed above indicate that there are two contrasting effects of temperature on the process of UFG formation during SPD; these are shown schematically in Fig. 52 [232]. The large strain value of  $\theta_{AV}$  may approach: (a) a saturation value at temperatures below  $0.5T_m$ , Fig. 52a; or (b) values that decrease with increasing temperature at temperatures above  $0.5T_m$ , Fig. 52b. We first consider the evolution of UFGs below  $0.5T_m$ , i.e. the results of Fig. 52a. An increase in processing temperature leads to a rapid increase in misorientation at large strains (i.e. in the third deformation stage). This can be attributed to the increasing ease of dynamic recovery, which accelerates the rearrangement of dislocations within the MSBs. Under such conditions, UFGs with HABs are developed more frequently at higher temperatures.

Nevertheless, the formation of MSBs also plays an important role in the development of UFGs. This process is, by contrast, also a mechanically-driven (athermal) one, as discussed in previous sections [168,185,198]. Thus, the structural heterogeneities introduced by SPD generally decrease with increase in temperature because of the following reasons: (i) the number of operating slip systems increases, leading to more homogeneous deformation; (ii) there is more annihilation of dislocation

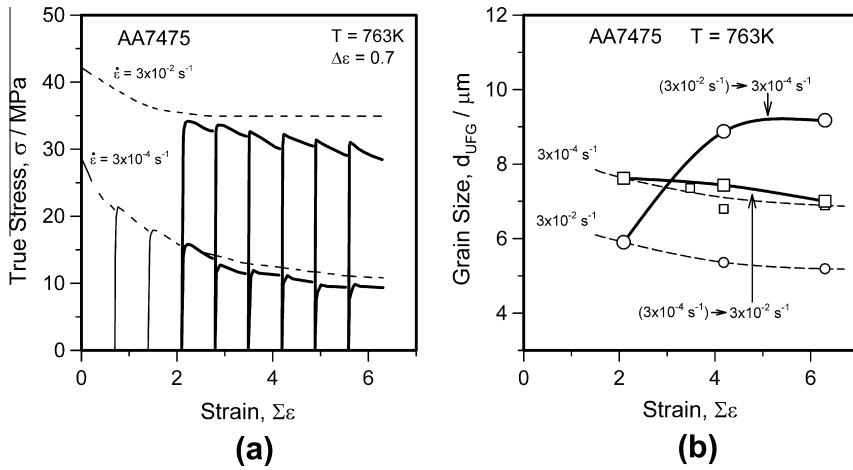


**Fig. 53.** Transient deformation behavior of AA7475 after MDF at 763 K on increasing or decreasing the strain rate: (a) true stress vs. cumulative strain, and (b) grain size vs. cumulative strain. The data for continuous deformation at constant strain rate are represented by dashed lines for comparison [235].

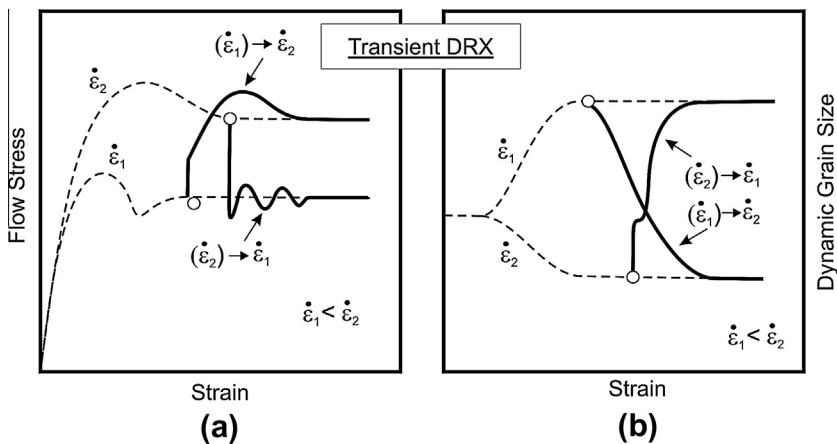


**Fig. 54.** Schematic representation of the transient behavior under dDRX conditions [67,235].

substructures due to the greater ease of dynamic recovery; and iii) precipitate particles dissolve more readily in the matrix. As a result, the number of grains containing MSBs decreases at elevated temperatures [52,168,231–234], making it more difficult for UFG formation. Conversely, at lower temperatures, finely dispersed particles restrict dislocation rearrangement, leading to stabilization of the substructure as well as the rapid formation of MSBs and UFGs.

It can therefore be concluded that the trends shown in Fig. 52a generally apply to all materials deformed at temperatures below  $0.5T_m$  (and even at relatively high temperatures in highly alloyed materials containing finely dispersed particles). Conversely, those in Fig. 52b appear in lightly alloyed materials deformed at temperatures above  $0.5T_m$ . The latter corresponds to the behavior of AA2219 in Fig. 51a. It can also be concluded [46,48,196] that grain formation is generally controlled by a combination of athermal processes at low to medium strains and thermally activated ones at large strains. These mechanisms are discussed in more detail in the next section.

#### 4.4.3. Transient deformation behavior during changes in strain rate

The microstructural behavior associated with changes in strain rate has been studied by MDF experiments carried out on an aluminum alloy. The effect of increasing or decreasing the strain rate was established by deforming samples of AA7475 at 763 K [235]. The resulting  $\sigma$ - $\Sigma\varepsilon$  curves and grain size evolution are displayed in Fig. 53. When the strain rate is increased or decreased at  $\Sigma\varepsilon = 2.1$ , the flow stress instantaneously increases or drops to approach the stress levels associated with continuous deformation. Nevertheless, after increasing the strain rate, the flow stress is *lower* than that developed at a constant strain rate of  $3 \times 10^{-2} \text{ s}^{-1}$ , see Fig. 53a. This difference increases with strain and is accompanied by an increase in  $V_{UFG}$ . From Fig. 53b, it can be seen that the stable grain sizes developed at large strains after a strain rate increase or decrease are noticeably greater than those produced during continuous deformation. These microstructural changes are consistent with the grain formation process being controlled by cDRX.

For comparison, the transient deformation behavior brought about by strain rate change testing under conventional dDRX conditions is described here briefly. The flow stresses and microstructural behaviors associated with constant and strain rate change tests are depicted schematically in Fig. 54 [67,236]. These results stand in clear contrast to those appearing in Fig. 53. Here the dashed lines represent continuous deformation at constant strain rate, while the solid lines show the results obtained after strain rate changes. The observations that have particular relevance to the current discussion can be described as follows:

- (1) When the strain rate is decreased, the flow curve exhibits multiple peaks, because grain coarsening occurs. Conversely, after an increase in strain rate, the flow curve displays a single peak accompanied by grain refinement. This behavior was discussed in more detail and illustrated in Fig. 13.
- (2) After a strain rate change, the two processes described in (1) above result in a new steady state after further strains of  $\varepsilon < 1$ . Both the flow stress and the dynamic grain size finally approach those attained during continuous deformation at the new strain rate [236].
- (3) It can thus be concluded that the transient phenomena described above are completely reversible and are therefore entirely controlled by thermally activated processes [67,236].

In the case of cDRX, by contrast, the strain-induced events involve irreversible phenomena, so that the flow stresses and grain sizes developed cannot be described by a unique function of the temperature-corrected strain rate [237]. Such mechanically-induced phenomena are strongly affected by the previous deformation history as well as by some material factors. The latter include the grain size, slip systems available, second phase particles, etc. All of these affect the formation of strain-induced UFGs and so should be studied systematically in more detail in the future.

#### 4.5. Mechanical properties of strain-induced UFG materials

Significant grain refinement down to the nanometer level is the most promising route for improvement of both the mechanical properties at ambient temperature and the workability at elevated temperatures [30]. The development of UFG sizes in metals and alloys increases their strength due to grain size strengthening. In the case of the UFG microstructures produced by plastic deformation, substructure strengthening due to the increased dislocation density and the presence of well developed subgrains also contributes to the strength. Furthermore, fine grain sizes are critical for good workability during hot deformation as they promote superplastic behavior. By refining the grain size, the optimal conditions for superplasticity can be extended to lower temperatures or higher strain rates, changes that are useful for industrial applications [211].

With regard to the mechanical properties at ambient temperature, an increase of strength is generally accompanied by a degradation in the ductility. Desirable combinations of mechanical properties, namely increased strength with sufficient ductility, can therefore be produced by refining the microstructure. The latter is in turn controlled by processing variables such as the temperature and strain as well as by post-deformation heat treatments. Highly impressive improvements in the mechanical properties produced by SPD have been reported for nanostructured titanium and copper

**Table 3**  
Tensile properties of titanium and its alloys subjected to MDF.

Material	Process	Grain size ( $\mu\text{m}$ )	Yield stress (MPa)	Ultimate tensile strength (MPa)	Total elongation (%)	Ref.
Ti, Grade 1	MDF	0.1	–	730	18	[239]
Ti, Grade 1	MDF + cold rolling	–	–	875	18	[239]
Ti, Grade 2	MDF	0.2	810	–	18	[242]
Ti, Grade 2	MDF + cold rolling	–	1210	–	9	[242]
Ti, Grade 2	Annealed at 800 °C	50	255	380	29	[239,242]
Ti–6Al–4V	MDF	0.5	1190	1220	9	[243]
Ti–6Al–4V	MDF	0.4	1180	1300	7	[243]
Ti–6Al–4V	MDF	0.3	1210	1350	7	[243]
Ti–6Al–4V	MDF	0.15	1280	1400	7	[243]
Ti–6Al–4V	MDF + cold rolling	–	1460	1500	8	[242]
Ti–6Al–4V	Annealed at 945 °C + aged at 500 °C	10	960	1050	9	[243]
Ti–6.7Al–4.7Mo	MDF	0.06	–	1400	20	[239]
Ti–6.7Al–4.7Mo	Forged at 950 °C	4–6	–	1050	22	[239]

**Table 4**  
Tensile properties of UFG aluminum alloys processed by ECAP.

Material	Process	Grain size ( $\mu\text{m}$ )	Yield stress (MPa)	Ultimate tensile strength (MPa)	Total elongation (%)	Ref.
AA1545	ECAP at 300 °C	0.55	370	410	17	[250]
AA1545	Hot rolled at 320–380 °C	~18	260	395	17	[250]
AA1570	ECAP at 300 °C	1.0	285	389	29	[250]
AA1570	ECAP + cold rolling	~0.5	495	550	15	[250]
AA2014	ECAP at 170 °C	–	460	520	6	[248]
AA2014	As-cast	140	225	280	3	[248]
Al–3% Mg	ECAP at room temperature	0.2	~480	~520	7	[247]
Al–3% Mg	ECAP at room temperature + annealed at 200 °C	0.58	~240	~310	23	[247]
Al–3% Mg	Annealed at 400 °C	300	~55	~230	32	[247]

alloys processed by HPT and ECAP at room temperature [238]. By using miniature tensile specimens, strengths of about 700 MPa and 400 MPa have been determined in Ti and Cu (more than twice their conventional strengths). Concurrently, the elongations to failure exceeded 35% and 50%, respectively. Thus, the mechanical properties of UFG materials processed by SPD are remarkable. Unfortunately, the corresponding properties of large scale UFG materials are not as outstanding, as the strengthening is usually accompanied by a deterioration in the ductility.

Among SPD methods, MDF is the simplest and can easily be scaled up for the processing of sizeable semi-products. The mechanical properties of bulk Ti and its alloys processed by MDF have been described in a series of papers by the group of Salishchev and co-workers [239–243]. Forging is usually begun at 700 °C to form a uniform fine grained microstructure, which leads to an increase in the workability. Then, the forging temperature is decreased by 50–100 °C per step so as to produce various UFG microstructures in the subsequent passes [243]. The grain sizes and tensile properties obtained in this way are presented in Table 3, along with a reference to the properties of coarse grained counterparts. The increase in tensile strength by a factor of three is quite remarkable for a commercially pure material, although it is accompanied by a twofold decrease in ductility. In two-phase titanium alloys, the production of UFG microstructures of 100 nm grain size strengthens the samples without any detrimental effect on the ductility [239,243]. It should be noted in Table 3 that the strength properties of UFG materials processed by SPD under warm deformation conditions can be further increased by an

additional cold working step (i.e. MDF + cold rolling). This appears to be a promising route for the commercial application of SPD-based thermomechanical processing.

The ECAP process is frequently used for the production of UFG structures in various aluminum alloys [244–251]. These materials can be processed at temperatures below 450 °C with the aid of tooling made of commercial heat resistant steels. Some examples of the strength improvements achieved in aluminum alloys by ECAP are presented in Table 4. A grain size decrease to well below 1 μm in a dilute aluminum alloy brings about a nearly tenfold increase in yield stress to about 500 MPa [247]. Such strengthening is accompanied by a significant decrease in ductility, although the latter can be somewhat improved by an appropriate heat treatment. For instance, the annealing of an Al–3% Mg alloy at 200 °C does not significantly change the grain size (which remains at the submicron level and provides strengthening), while the total elongation increases to 23%. The latter is comparable to that of a well annealed coarse grained alloy [247]. It should be noted that additional cold working, e.g. rolling, after ECAP can provide further increases in strength in UFG aluminum alloys in a manner similar to that described above for titanium alloys.

Unfortunately, ECAP is rather laborious and time consuming and can only produce samples of limited size. As a result, it is unlikely that commercial applications will be found in its original form. Nevertheless, attempts have been made to adapt the ECAP technique to industrial use [252–254]. One of these combines ECAP with the Conform process [255] so as to produce UFG metals and alloys for large scale commercial production in a continuous manner [253]. Another modification is aimed at producing plate shaped products [252,254] using a die designed to accommodate the width of pressed samples. These samples can subsequently be rolled into advanced sheet materials.

The effectiveness of SPD for the production of UFG materials depends on the kinetics of grain refinement during plastic working, i.e. on the critical strains for the initiation and completion of cDRX. Different metallic materials are characterized by differing kinetics of grain refinement during SPD, as seen in Fig. 47. The rapid achievement of nanocrystalline microstructures has been observed in materials that allow pronounced grain subdivision during plastic working. Typical examples of such materials are titanium (Ti), magnesium (Mg) alloys, and metastable austenitic steels [43,69,70,256–258]. In contrast to the behaviors of hexagonal Ti and Mg alloys, grain refinement in austenitic steels is accelerated by multiple mechanical twinning assisted by strain-induced phase transformation. This leads to the rapid development of nanocrystalline microstructures at relatively low strains, which can be readily attained using ordinary cold working methods. For example, UFG microstructures consisting of a mixture of austenite and ferrite grains with average sizes of about 50 nm can be produced in an austenitic stainless steel by MDF as well as by conventional cold rolling as long as total strains

**Table 5**

Tensile properties of UFG stainless steels subjected to various SPD procedures and subsequently annealed.

Material	Processing	Grain size (μm)	Yield stress (MPa)	Ultimate tensile strength (MPa)	Total elongation (%)	Ref.
SUS316	MDF at room temperature	0.05	2050	2075	10	[260]
SUS316	MDF at –200 °C	0.04	2100	2125	10	[260]
S304H	MDF at room temperature	0.03	1430	1540	7	[261]
S304H	MDF at room temperature + annealed at 500 °C	0.05	1420	1570	5	[261]
S304H	Cold rolling	0.05	2050	2065	2	[259]
S304H	Cold rolling + annealed at 600 °C	0.09	1345	1520	5	[259]
S304H	Cold rolling + annealed at 700 °C	0.17	1050	1160	9	[259]
Fe–27% Cr–9% Ni	Cold swaging	0.16	1760	1800	7	[262]
Fe–27% Cr–9% Ni	Cold swaging + annealed at 500 °C	0.21	1690	1710	9	[262]
Fe–27% Cr–9% Ni	Annealed at 1100 °C	–	600	740	–	[262]
Fe–15% Cr	Cold swaging	0.21	900	1090	11	[263]
Fe–15% Cr	Cold swaging + annealed at 500 °C	0.26	570	840	15	[263]
Fe–15% Cr	Cold swaging + annealed at 600 °C	0.40	465	640	24	[263]
UNS S32304	ECAP at room temperature	0.10	1460	1800	8	[264]
UNS S32304	ECAP at room temperature + annealed at 700 °C	0.17	1100	1433	17	[264]

**Table 6**  
Superplastic properties of UFG titanium and aluminum alloys.

Material	Grain size ( $\mu\text{m}$ )	Temperature ( $^{\circ}\text{C}$ )	Strain rate ( $\text{s}^{-1}$ )	Total elongation (%)	Strain rate sensitivity	Ref.
Ti, Grade 1	0.1	450	$10^{-4}$	115	0.30	[239]
Ti, Grade 1	0.2	550	$5 \times 10^{-4}$	190	0.32	[239]
Ti–6.7Al–4.7Mo	0.06	550	$2 \times 10^{-4}$	410	0.33	[239]
Ti–6.7Al–4.7Mo	0.06	575	$2 \times 10^{-4}$	1200	0.45	[239]
Ti–6Al–4V	0.3	600	$5 \times 10^{-4}$	500	0.34	[239]
Ti–11Mo–5.5Sn–4Zr	0.3	550	$5 \times 10^{-4}$	390	0.46	[239]
Ti–11Mo–5.5Sn–4Zr	0.5	625	$7 \times 10^{-4}$	580	0.47	[239]
AA7055	1.0	300	$3 \times 10^{-4}$	400	0.42	[254]
AA7055	1.0	450	$10^{-2}$	680	0.38	[254]
AA7075	1.3	525	$10^{-2}$	420	0.59	[265]
AA5024	0.8	250	$3 \times 10^{-3}$	885	0.42	[266]
AA5024	0.8	450	$6 \times 10^{-1}$	3300	0.20	[266]
AA1570	0.7	400–450	$3 \times 10^{-2}$ – $6 \times 10^{-1}$	>1000	~0.55	[267]
AA1421	0.8	300–450	$10^{-2}$ – $10^{-1}$	>1000	>0.3	[268]
AA1443	~4	350–500	$10^{-3}$ – $10^{-1}$	>150	>0.3	[269]

of about 4 are applied [258,259]. The production of such UFG microstructures in Cr–Ni stainless steels leads to significant strengthening as the yield stress can be increased to more than 2000 MPa [259].

The UFG structures developed during SPD are quite stable as they resist grain growth upon subsequent heating, as discussed in Section 5 below in detail. Dual-phase microstructures are particularly stable during annealing because the different phases limit grain growth. UFG materials of various grain sizes and levels of residual stresses can, therefore, be readily produced in multi-phase steels and alloys by appropriate combinations of SPD and annealing. Some examples of the mechanical properties of stainless steels containing UFG microstructures produced by various methods of SPD and post-deformation annealing are presented in Table 5 [259–264]. The data indicate that beneficial combinations of mechanical properties can be attained in metastable steels without requiring the application of large strains. The UFG microstructures developed in this way remain essentially unchanged during subsequent heat treatment. These findings open up fresh opportunities for the production of advanced stainless steels.

Another important property of UFG materials is their hot workability. Processing under superplastic conditions permits the production of complex parts from almost all structural metals and alloys [211]. The wider commercial application of superplastic forming, however, is limited by the necessity to use high temperature isothermal devices and low strain rates; the latter significantly affect the productivity. Grain size decreases down to the submicron level make it possible to utilize superplasticity at relatively low temperatures and high strain rates. Some impressive superplastic properties of UFG titanium and aluminum alloys processed by SPD are summarized in Table 6 [239,254,265–269]. Titanium and its alloys with nanocrystalline microstructures exhibit superplastic behavior at temperatures of 450–600  $^{\circ}\text{C}$ , which are well below  $0.5T_m$ . In the case of the aluminum alloys, superplastic forming can be carried out at strain rates as high as  $0.1 \text{ s}^{-1}$ . The results presented here indicate that the UFG metallic semi-products produced by SPD are the outcome of numerous technological advances.

The mechanical property and mechanistic aspects of grain refinement by SPD have recently been reviewed by Estrin and Vinogradov [223]. It should be noted that the development of UFG structures by SPD changes various properties of processed metals and alloys and these changes are beneficial for certain applications. Under appropriate conditions of SPD, structural strengthening can be achieved simultaneously with improvements in both the low- and high-cycle fatigue properties [270–272]. An unusual increase in impact toughness at low temperatures has been reported for UFG titanium and low-alloy steels [273,274]. Ultra-fast diffusion rates have been observed in UFG nickel and copper alloys; these were attributed to the non-equilibrium state of the strain-induced boundaries [275,276]. The high diffusion rates in UFG materials are favorable for surface treatments, e.g. by plasma ion

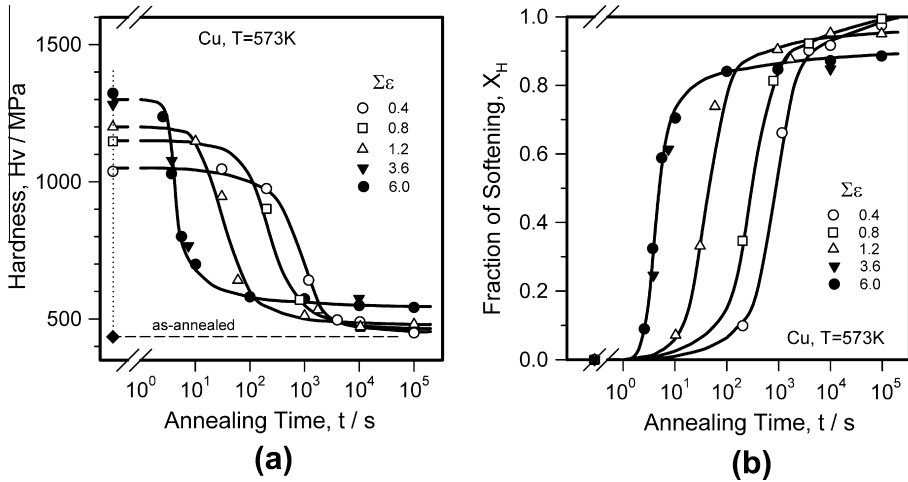


**Fig. 55.** (a) Effect of prior strain and time on Vickers hardness in copper after MDF to  $\Sigma\varepsilon$  of 0.4 to 6.0 at 300 K and annealing at 573 K. (b) Fractional softening–annealing time curves derived from the hardness data in (a) [279].

nitriding, which can further improve their properties [277,278]. Because of their unique combinations of properties, UFG metals and alloys can therefore be readily characterized as advanced materials and excellent candidates for novel technological and engineering applications.

## 5. Post-dynamic recrystallization – Annealing behavior after dynamic recrystallization

### 5.1. Post-cDRX

The annealing of metals has been frequently studied because of the importance of controlling the resulting microstructures and textures [1–5,12,13]. Because the microstructures produced by dDRX and cDRX are generally unstable at elevated temperatures, the effects of annealing them are reviewed here. This examination will include a discussion of the mechanisms operating during annealing in each type of recrystallizing matrix.

The annealing of copper deformed to large strains will be discussed first. A series of room temperature hardness vs. annealing time ( $H_v$ – $t$ ) curves is illustrated in Fig. 55a [279]. Here copper was deformed by multi-directional forging (MDF) at 300 K to various cumulative strains  $\Sigma\varepsilon$ . It is evident that the  $H_v$ – $t$  curves depend sensitively on the prior deformation up to strains of about 2.  $H_v$  decreases slowly at first and then more rapidly until it finally approaches the fully annealed value. In this strain range, conventional static recrystallization (SRX) takes place during annealing, i.e. new grains nucleate after which the long-range migration of grain boundaries takes place. These curves are of conventional sigmoidal shape and move to shorter times with increased strains.

At large cumulative strains, such as  $\Sigma\varepsilon = 3.6$  and 6.0, a steady state of flow is achieved (see Fig. 28), so that the  $H_v$ – $t$  curves are no longer dependent on the prior strain. In this case, there is a sharp drop in  $H_v$  at around 2–4 s, after which it decreases more gradually. It is important to note that, after large prestrains,  $H_v$  does not drop to the fully annealed value at long times. This indicates that the UFG structures developed at large strains are stable even during extended annealing. Also of interest are the fractional softening–annealing time ( $X_H$ – $t$ ) curves of Fig. 55b. These were derived from the  $H_v$ – $t$  curves of Fig. 55a using the equation:  $X_H = (H_\varepsilon - H_t)/(H_\varepsilon - H_0)$ . Here  $H_0$ ,  $H_\varepsilon$  and  $H_t$  are the hardness values corresponding to the fully annealed state, the deformed state at a strain of  $\varepsilon$ , and the intermediate state after annealing for time  $t$ , respectively. The data of Fig. 55b will be analyzed later together with the results of Figs. 56 and 57.

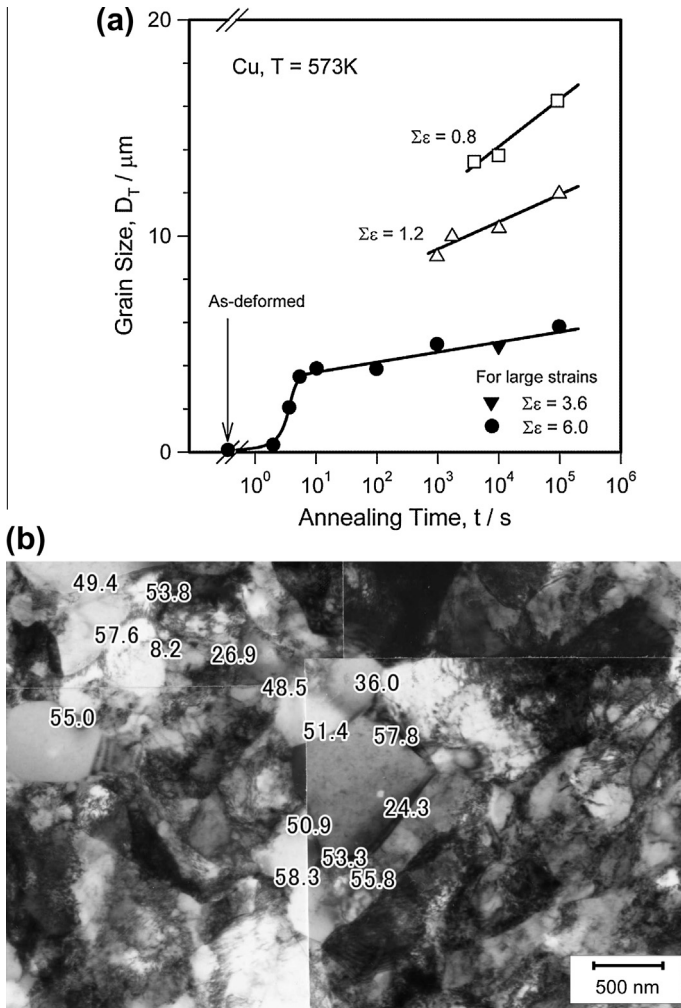


**Fig. 56.** (a) Dependence of the average grain size (including twins)  $D_T$  on annealing time at  $573\text{ K}$  in copper MDF to cumulative strains  $\Sigma\varepsilon$  of  $0.8$ – $6.0$  at  $300\text{ K}$ . (b) TEM microstructure after annealing the copper deformed to  $\Sigma\varepsilon = 6.0$  for  $2\text{ s}$ . The numbers indicate the boundary misorientations in degrees [279].

The changes in grain size with annealing time at  $573\text{ K}$  are depicted in Fig. 56a. For prior strains of  $0.8$  and  $1.2$ , only the results after full SRX are displayed; this is because the microstructures developed during SRX are mixed, being composed of both strain hardened and recrystallized grains. Here, the grain size produced by recrystallization results from conventional grain growth, after which grain coarsening takes place during prolonged annealing. By contrast, after prior strains of  $\Sigma\varepsilon = 3.6$  and  $6.0$ , the grain size changes take place *homogeneously* in space during all stages of annealing. This type of grain coarsening stands in sharp relief to the grain growth behavior observed immediately after straining to  $\Sigma\varepsilon = 0.8$  and  $1.2$ .

After large prior strains, the grain size changes take place in three stages: (1) First there is a kind of incubation period with little change. (2) Then there is rapid grain coarsening at around  $2$ – $4\text{ s}$ . (3) Finally, there is a gradual increase in grain size due to further coarsening. It is of interest that the sharp changes in the second stage are associated with the rapid drop in  $H_v$  at  $2$ – $4\text{ s}$  in Fig. 55a.

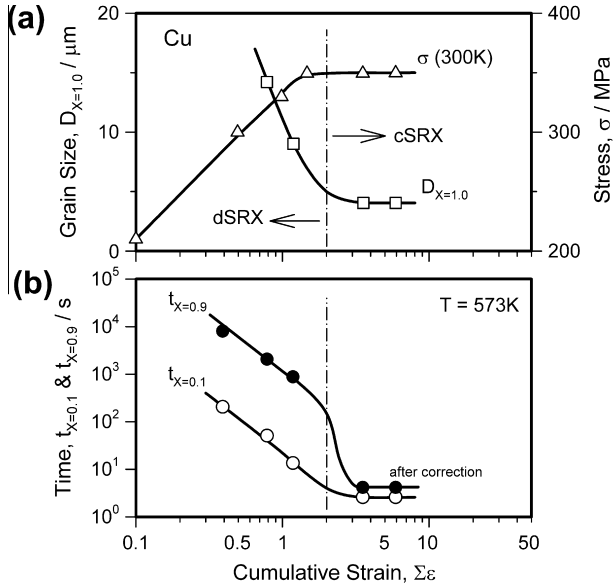


**Fig. 57.** (a) Prior strain dependence of the average grain size  $D_{X=1.0}$  after full dSRX ( $\Sigma\varepsilon < 2$ , left side of diagram), and full cSRX ( $\Sigma\varepsilon > 3$ , right side of diagram), in copper (solid line). The flow stress vs. cumulative strain relationship for MDF at 300 K is shown for reference. (b) Prior strain dependence of the times required for 10% and 90% softening,  $t_{X=0.1}$  and  $t_{X=0.9}$ . These have been corrected to show only the rapid softening produced by cSRX [279].

A TEM micrograph showing the microstructure after annealing for 2 s is illustrated in Fig. 56b [279]. This corresponds to the beginning of the second stage mentioned above. Here, fine subgrains and grains can be seen containing a range of dislocation densities; under these conditions, no new grains were observed using optical microscopy [279]. The sizes of the grains containing low dislocation densities ranged from 0.5 to 0.6  $\mu\text{m}$ ; these are larger than the average value of 0.2  $\mu\text{m}$  determined in the as-deformed sample (see Fig. 30). It should be noted that the former grains evolve in colonies and appear to have consumed their high dislocation density neighbors. Thus, the results in Figs. 55 and 56 indicate that the final microstructure is produced by a type of continuous SRX (cSRX) that is the static analog of continuous DRX or perhaps of precipitate ripening or coarsening. The process of cSRX that operates in UFG copper is clearly a mechanism that merits further study.

We turn now to the fractional softening curves of Fig. 55b and the grain size–time relationship of Fig. 56a. After large strains and long holding times, the data can be approximated by a straight line and it is evident that slow grain coarsening is taking place. According to this view, softening in the UFG copper is composed of the following components: (i) about 60% takes place by rapid cSRX; (ii) 30% is due to slow grain coarsening, and (iii) 10% remains in the material, even after long annealing times. The latter supports the view of Humphreys [280] that the UFG structures introduced by SPD are rather stable thermally. As will be shown below in more detail when the TEM results are presented for the 304 stainless steel (Fig. 59), the rapid softening (60%) stage involves the removal of the high dislocation density subgrains and the more gradual (30%) stage the removal of lower density regions and some grain coarsening. The lowest density regions persist even after long annealing times because of the low driving force for coarsening.

The prior strain dependences of some of the parameters in Figs. 55 and 56 are presented in Fig. 57 [279]. The grain size  $D_{X=1.0}$  after full SRX or cSRX in Fig. 56a is plotted against the cumulative strain  $\Sigma\varepsilon$  in Fig. 57a, together with the associated flow stress (see Fig. 28). The strain dependence of the time required for 10% and 90% softening,  $t_{X=0.1}$  and  $t_{X=0.9}$  in Fig. 55b is depicted in Fig. 57b. It can be seen that  $D_{X=1.0}$ ,  $t_{X=0.1}$  and  $t_{X=0.9}$  decrease rapidly with increasing strain during work hardening and the early stages of steady-state flow, finally leveling out at strains above 3. This indicates that the transition

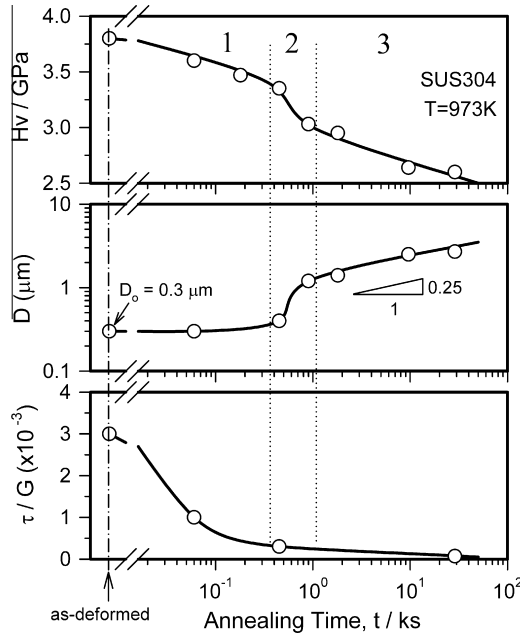


**Fig. 58.** Dependence on time of annealing at 973 K of the room temperature hardness ( $H_v$ ), grain size ( $D$ ), and internal stress normalized by the shear modulus ( $\tau/G$ ) in 304 stainless steel processed by MDF to  $\Sigma\varepsilon = 6.4$  at 873 K [201].

from SRX to cSRX behavior takes place at about  $\varepsilon \approx 3$  in UFG copper. The inverse of the logarithm of the time difference  $\Delta t_{X=0.1-0.9}$  can be taken as approximately proportional to the exponent in the JMAK equation for SRX. This is about 2 for SRX ( $\Sigma\varepsilon \ll 3$ ), and about 20 for cSRX ( $\Sigma\varepsilon > 3$ ). These values support the interpretation that SRX takes place after low prestrains and that cSRX operates in UFG structures after large strains.

We turn now to the annealing of UFG 304 stainless steel processed by MDF at 973 K. The effect of annealing time on the room temperature hardness  $H_v$  is presented in Fig. 58. This material was strained to  $\Sigma\varepsilon = 6.4$  at 873 K [201]. The dependences of the grain size  $D$ , and the internal stress normalized by the shear modulus  $\tau/G$  are also shown. (Here, the latter were determined from distortions in the diffraction patterns, as described in [193,195].) The annealing process can be subdivided into three sequential stages, as indicated by the broken lines in Fig. 58. These ranges are similar to those described above for the UFG copper in Fig. 56a.  $H_v$  first decreases gradually during the first stage; this is followed by a rapid drop in the second stage. Then, during the third stage, the softening kinetics slow down to the same low rate as in the first stage. It should be noted that there is little grain coarsening in stage 1 even though some softening is taking place. Concurrently, the high internal stresses (see below) developed in the UFG steel are rapidly released and approach zero. The main phenomenon detected during the first stage is the rapid decrease in internal stress, which is accompanied by a slight decrease in the hardness. This is analyzed in more detail below.

Some TEM microstructures in the vicinities of the grain boundaries in the UFG 304 steel are illustrated in Fig. 59 [201]. These reveal the changes brought about by annealing for 450 s at 973 K. Distorted crystallographic planes are evident in the as-processed state (Fig. 59a). The boundary is identified by the small circles. In the sample annealed for 450 s, on the other hand, the structures associated with the grain boundary regions are sharp and the crystallographic planes near the boundary are straight. This is clearly indicated in Fig. 59b and corresponds to the beginning of the second stage. It can, therefore, be concluded that high internal stresses are generated near the grain boundaries during SPD [30,195,201] and that these are removed by static recovery during the early stages of

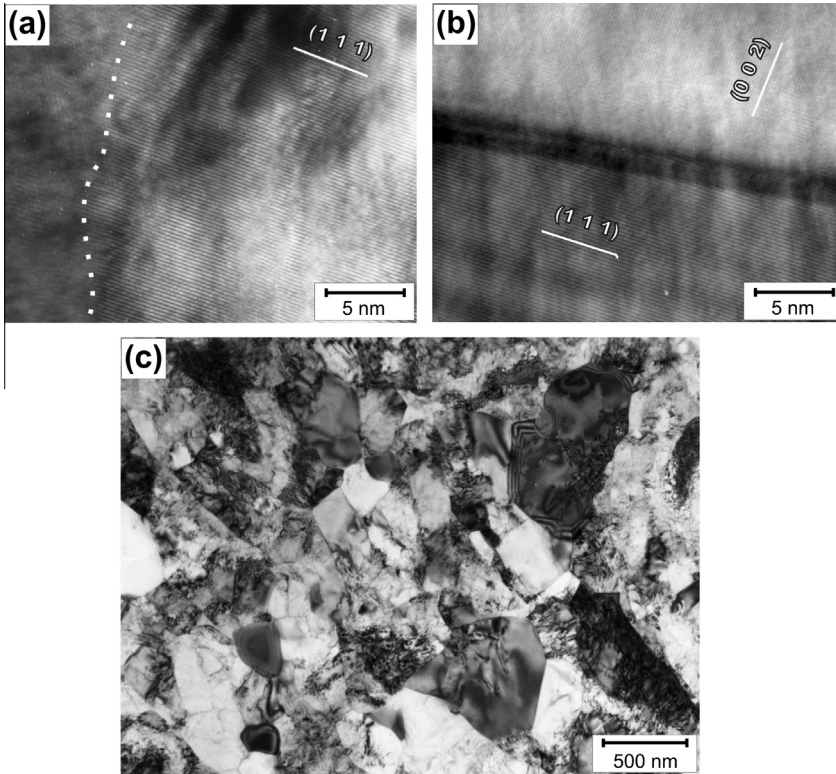


**Fig. 59.** TEM microstructures in a 304 stainless steel processed by MDF to  $\Sigma\varepsilon = 6.4$  at 873 K: (a) the as-deformed state, (b) and (c) after annealing for 450 s at 973 K [201]. The misorientations between neighboring microcrystallites are around  $60^\circ$  in (a) and  $45^\circ$  in (b). (c) A mixed grain structure composed of some UFGs with high dislocation densities and others with low densities.

annealing. Such recovery also transforms the nonequilibrium grain boundaries into equilibrium ones [30,281].

Rapid grain coarsening takes place during the second stage of annealing, driven by the grain boundary energy as well as by the removal of dislocations [4,280]. Some typical microstructures associated with the beginning of stage 2 in the 304 steel are illustrated in Fig. 59c and in the copper in Fig. 56b. Here, some of the UFGs contain high densities of dislocations and others have lower densities in their interiors. These inhomogeneities are a distinctive feature of grain coarsening in stage 2 and disappear at the beginning of stage 3 [201]. This process is accompanied by an increase in both the sub-boundary misorientation  $\theta_{AV}$  and the grain size  $D$  [195,279]. During the third stage that follows, by contrast, the relatively slow coarsening rate is driven largely by the grain boundary energy. The growth exponent for coarsening is about 4 in stage 3, Fig. 58b, which falls within the 2–10 range reported for single-phase materials [4].

We now turn to the annealing behavior of a UFG Mg alloy. The dependences on time of the grain size  $D$ , number of fine grains below 10  $\mu\text{m}$  in diameter  $N$ , and mean boundary misorientation  $\theta_{AV}$  are presented in Fig. 60a [282]. Some OIM micrographs showing the changes taking place during annealing at 503 K are illustrated in Fig. 60b. The AZ31 Mg alloy was compressed to  $\varepsilon = 1.2$  at 573 K and quenched in water; subsequently, it was annealed for various times at 503 K. It can be seen in Fig. 60b that most of the grains develop a (0001) texture, which then remains stable during annealing [283]. This process can again be separated into three stages, as was done for the copper (Fig. 56) and the 304 stainless steel (Fig. 58). The average grain size remains almost constant in stage 1, while grain coarsening takes place in stages 2 and 3, accompanied by a decrease in  $N$  as well as an increase in  $\theta_{AV}$ .

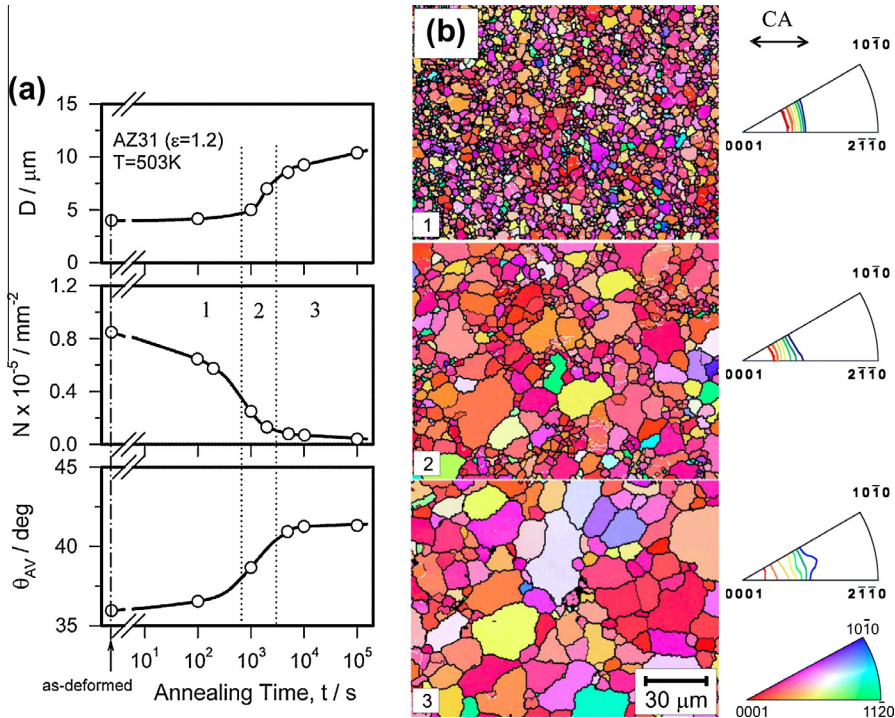


**Fig. 60.** (a) Dependence on annealing time at 503 K of the average grain size  $D$ , number of fine grains  $N$  less than 10  $\mu\text{m}$  in diameter, and sub-boundary misorientation  $\theta_{AV}$  in AZ31 alloy. The sample was compressed to  $\varepsilon = 1.2$  at 573 K. (b) OIM micrographs and inverse pole figures of AZ31 alloy compressed to  $\varepsilon = 1.2$  at 573 K and then annealed at 503 K for various times  $t$ . (1)  $t = 0$  s, (2)  $t = 10^3$  s and (3)  $t = 10^4$  s. Colors corresponding to the crystallographic orientations are indicated in the inverse pole figure. The line definitions are those of Fig. 42 [282,283].

During further annealing,  $\theta_{AV}$  remains approximately constant, while  $D$  increases gradually as a result of the grain coarsening taking place in stage 3.

The annealing behaviors of the materials reviewed above, i.e. copper, 304 stainless steel, AZ31 Mg and some UFG nickel and aluminum alloys [284,285] were shown to be remarkably similar. It can therefore be concluded that static recovery (SRV) generally takes place, accompanied by a type of grain coarsening during all 3 stages of annealing. Concurrently, the deformation texture hardly changes at all (Fig. 60b). Thus cSRX (a type of *static* recovery) takes place homogeneously in space in a manner somewhat analogous to that of cDRX during SPD, which is a type of *dynamic* recovery.

## 5.2. Post-dDRX

The annealing behavior after dDRX is reviewed briefly here for several materials. The mechanisms operating after dDRX are compared with those acting after cDRX, which were described in Section 5.1. The effects of prior strain and annealing temperature on static softening ( $X-t$ ) in copper and a 0.4% carbon steel are illustrated in Fig. 61 [286,287]. Here softening was measured by means of interrupted compression or tension testing. The degree of static softening  $X$  is defined by the equation:  $X = (\sigma_\varepsilon - \sigma_{y2}) / (\sigma_\varepsilon - \sigma_{y1})$ , where  $\sigma_{y1}$  and  $\sigma_{y2}$  are the initial and reloading yield stresses and  $\sigma_\varepsilon$  is the flow stress immediately before unloading.

A prior strain of 0.1 is less than the critical strain for dDRX (see the inset of Fig. 61a) and so only dynamic recovery (DRV) takes place during straining. On increasing the prestrain to  $\varepsilon = 0.60$  in copper and  $\varepsilon = 0.26$  in the carbon steel, dDRX has become fully developed. The flow stresses generated at

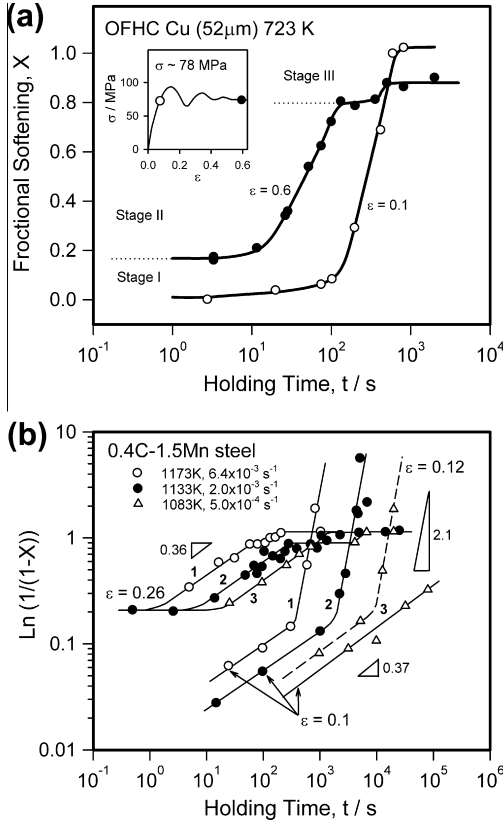


**Fig. 61.** (a) Effect of prior strain on static softening in copper at 723 K measured by means of interrupted compression testing. The microstructures developed at strains of 0.10 and 0.60 were (i) dynamically recovered and (ii) dynamically recrystallized, respectively [286]. (b) Effect of annealing temperature on the static softening  $X$  vs. annealing time  $t$  relationship plotted according to the Avrami equation in a 0.4 wt% C steel [287]. Interrupted tensile tests were carried out to prior strains of 0.10 or 0.26 at three sets of temperature and strain rate associated with the same value of the Zener–Hollomon parameter. Note that two-step softening takes place after dynamic recovery ( $\epsilon = 0.10$ ) and there is three-step softening as well as incomplete softening after dDRX ( $\epsilon = 0.26$ ).

$\epsilon = 0.10$  and  $0.60$  in the copper and  $\epsilon = 0.10$  and  $0.26$  in the steel are about equal under the three different conditions of temperature and strain rate. The latter lead to the same value of the Zener–Hollomon parameter expressed by Eq. (1), indicating that the stored energies are similar despite the different temperatures, strains, and strain rates employed.

The softening curve for  $\epsilon = 0.1$  in Fig. 61a is of sigmoidal shape and approaches full softening. By contrast, the  $X-t$  curve for  $\epsilon = 0.60$  consists of three distinct stages with three plateaus, terminating in incomplete softening within the time frame of the experiments. Some typical  $X-t$  curves for hot-deformed austenite are presented in terms of the Avrami relationship in Fig. 61b. After prestraining to  $\epsilon = 0.10$ , the initial stages of softening resulted from SRV and the second stage from SRX; these mechanisms were identified from the slopes of the Avrami plots. By contrast, the softening curves for  $\epsilon = 0.26$  consist of three stages, as in the case of the copper deformed to  $\epsilon = 0.60$  above. There is: (i) an almost instantaneous initial stage of softening, leading to a plateau at  $X = 0.2$ ; (ii) a second stage of substantial softening with an Avrami slope of 0.36 terminated by a second plateau; and (iii) finally, a third stage of softening to  $X = 0.7$  followed by a third plateau. The three stages end in incomplete softening. Note that the two sets of softening curves labeled 1, 2, 3 correspond to the annealing

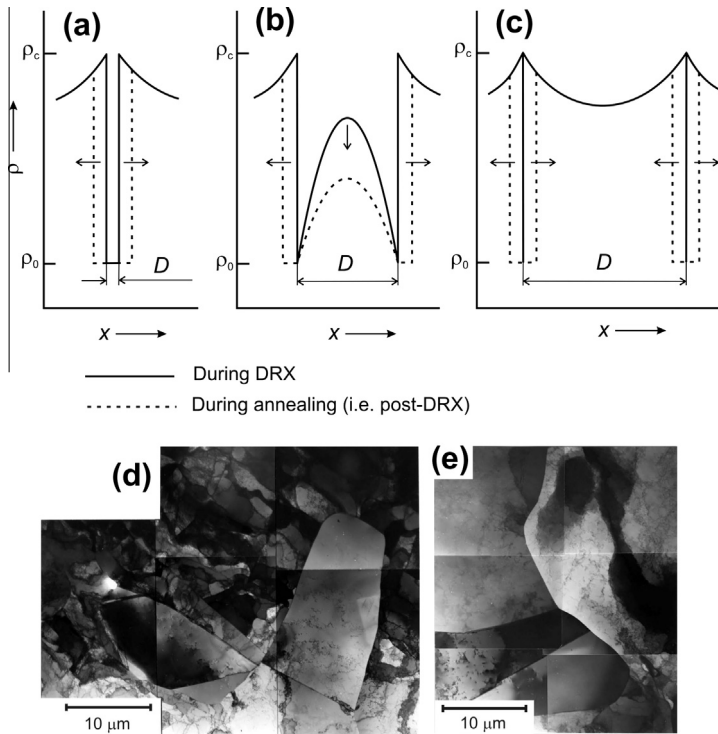


**Fig. 62.** Three types of dislocation density distribution developed in a microstructure undergoing dDRX (full lines) and the post-dynamic restoration behavior in each of the three regions (broken lines): (a) a recently nucleated dynamic grain growing into its surroundings without requiring an incubation time, i.e. mDRX, (b) a growing dynamic grain containing a dislocation density gradient, and (c) conventional SRX taking place in the fully strain-hardened dynamic grains. Here  $\rho_0$  is the initial (annealed) dislocation density,  $\rho_c$  is the critical value required for nucleation, and  $D$  is the current dynamic grain size (see Fig. 10) [288]. In the TEM micrographs at the bottom, (d) evidence for mDRX after annealing for 0.03 s, (e) grain boundary impingement occurring between a statically recrystallizing grain (lower left) and a dDRX grain containing a dislocation density gradient observed after annealing for 10 s. Here nickel was deformed to  $\varepsilon = 0.28$  at 1050 K, annealed for various times at 1050 K, and hydrogen quenched [288].

behaviors of samples deformed at the same value of  $Z$ , but at different combinations of temperature and strain rate. After both prestrains, softening is most rapid at the highest temperature even though the driving forces are identical.

Such softening behaviors in dDRX matrices result from the heterogeneous nature of the dislocation substructures developed in the grain interiors, which were discussed in detail in Section 3. These vary from grain to grain and are distributed rather heterogeneously [17]. The dynamic structures consist of the following three categories, illustrated schematically by the solid lines in Fig. 62 [288] (see also Fig. 10): (a) a freshly nucleated grain, (b) a growing dDRX grain containing a dislocation density gradient, and (c) a critically strain-hardened dDRX grain containing a fairly homogeneous and well developed substructure.

Once hot deformation has ceased, the just nucleated dDRX grains (Fig. 62a) continue to grow without requiring an incubation time, as indicated by the dashed lines in this figure. This is referred to as metadynamic recrystallization (mDRX), a term originally proposed by Jonas and co-workers [288–290]. It is also known as post-dynamic recrystallization (pDRX). The growing dDRX grains (Fig. 62b) contain few dislocations near their boundaries, so classical nucleation is not possible in the grain interiors and they can only soften by SRV. Finally, the fully strain-hardened dDRX grains (Fig. 62c) undergo SRV followed by nucleation, leading to classical SRX. Two TEM micrographs of

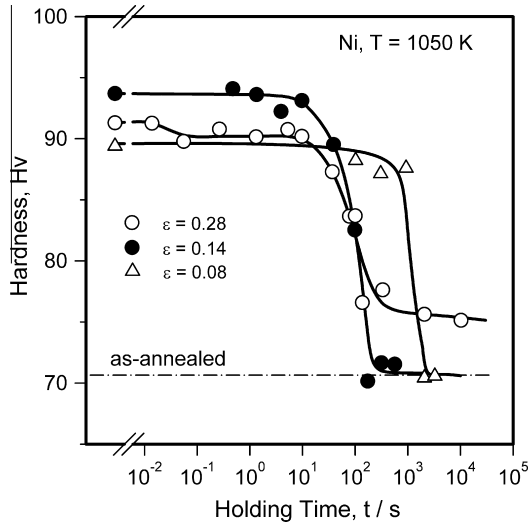


**Fig. 63.** Effect of prior strain on room temperature hardness vs. annealing time curves in nickel deformed to strains of 0.08–0.28, annealed for various times at 1050 K, and hydrogen quenched [288]. The microstructures developed at strains of 0.08 and 0.14 were dynamically recovered and that at a strain of 0.28 dynamically recrystallized [288].

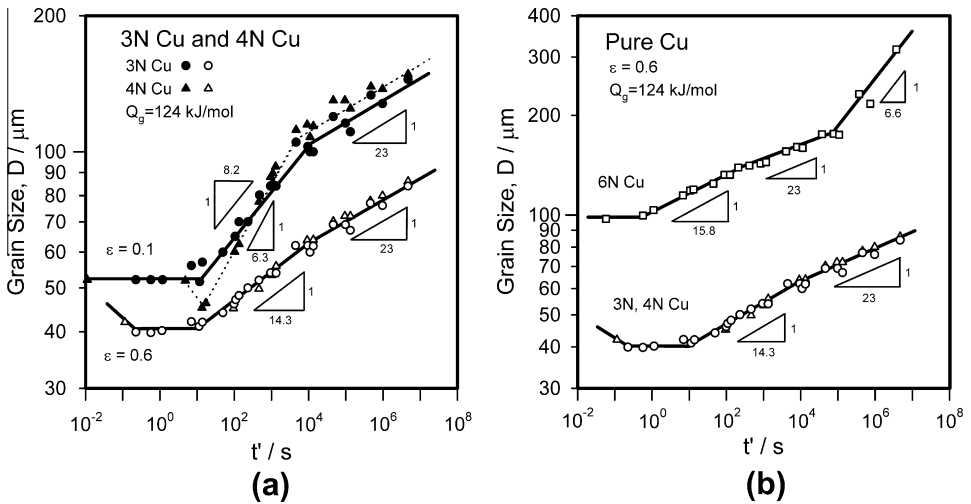


**Fig. 64.** Dependence of average grain size  $D$  on normalized annealing time  $t'$  corresponding to the average experimental temperature  $T = 873$  K. The annealing temperatures used ranged from 723 K to 1023 K. The 3N and 4N copper samples were deformed at  $2 \times 10^{-3} \text{ s}^{-1}$  to strains of 0.1 and 0.6 at 723 K and the 6N Cu at  $2 \times 10^{-2} \text{ s}^{-1}$  to a strain of 0.6. The microstructures developed at strains of 0.1 and 0.6 were dynamically recovered and dynamically recrystallized, respectively [286].

hot deformed nickel annealed at 1050 K and hydrogen gas quenched are illustrated at the bottom of Fig. 62 [288]. These provide evidence for (i) mDRX at  $t = 0.03$  s in Fig. 62d; and (ii) grain boundary impingement between a recrystallizing grain and a dDRX grain after annealing for  $t = 10$  s in Fig. 62e.

Some annealing results obtained on Ni undergoing dDRX are displayed in Fig. 63. Here polycrystalline nickel was deformed in tension at 1050 K to various strains, held at this temperature for increasing time intervals, and then hydrogen quenched [288]. After prior strains of 0.08 and 0.14, there is an incubation period of 1000 s ( $\epsilon = 0.08$ ) or 100 s ( $\epsilon = 0.14$ ) after which  $H_V$  drops rapidly due to SRX,

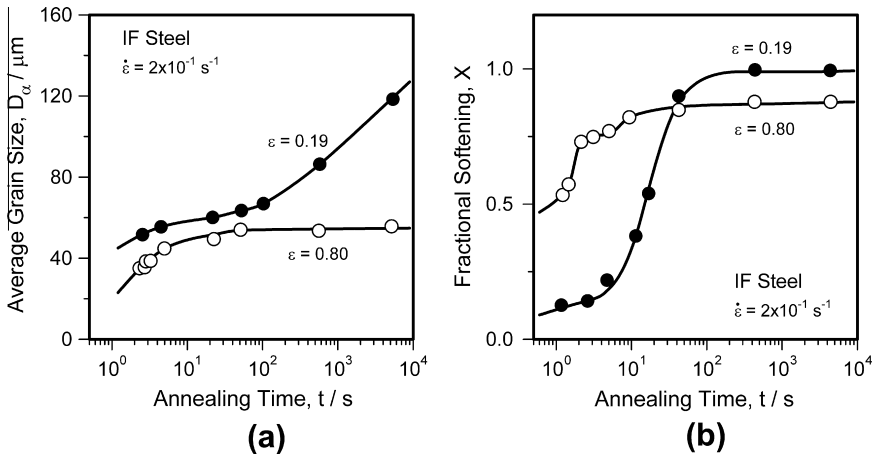


**Fig. 65.** Effect of annealing austenite deformed to strains of  $\varepsilon = 0.19$  and  $0.80$  on the average ferrite grain size  $D_\alpha$  produced by rapid cooling. The  $D_\alpha$ - $t$  curves are compared with the austenite fractional softening vs. annealing time ( $X$ - $t$ ) curves. An interstitial free (IF) steel was deformed at  $1233 \text{ K}$  and  $2 \times 10^{-1} \text{ s}^{-1}$ , annealed at  $1233 \text{ K}$ , and then rapidly cooled. The microstructures developed at strains of  $0.19$  and  $0.80$  were dynamically recovered and dynamically recrystallized, respectively [291].

attaining full softening at long times. When a dDRX microstructure (Ni deformed to  $\varepsilon = 0.28$ ) is held at temperature and then quenched, the room temperature hardness  $H_V$  does not decrease to the fully annealed value. The  $H_V$ - $t$  curve for a dDRX structure at  $\varepsilon = 0.28$  contrasts sharply with those for the lower prior strains. Here there is very rapid softening by recovery and SRX (not shown in Fig. 63) and then a sharp drop during the period from 10 to 100 s due principally to mDRX. It should be noted, however, that  $H_V$  does not approach full softening after dDRX at long holding times.

The changes in grain size  $D$  with annealing time  $t'_{873}$  normalized to  $873 \text{ K}$  are illustrated in Fig. 64 for three kinds of pure copper with purities of 99.97, 99.99 and 99.9999 mass percent. These are designated as 3N, 4N and 6NCu, respectively [287]. Here,  $t'_{873} = t \exp(-Q_{gb}/RT) / \exp(-Q_{gb}/RT_m)$  where  $T_m = 873 \text{ K}$  is the mean temperature employed in these experiments and  $Q_{gb} = 124 \text{ kJ/mol}$ . The copper samples were compressed to strains of  $0.10$  and  $0.60$  at  $723 \text{ K}$  (see Fig. 61a), after which they were annealed at temperatures from  $723 \text{ K}$  to  $1023 \text{ K}$ . The effect of prior strain on the  $D$ - $t'$  curves for 3NCu and 4NCu is shown in Fig. 64a, while that for the 6N copper is illustrated in Fig. 64b. It is evident from Fig. 64a that the rate of increase in grain size in the dDRX material ( $\varepsilon = 0.6$ ) is less than in the work hardened matrix ( $\varepsilon = 0.1$ ), although the beginning of growth in the two materials ( $\varepsilon = 0.1$  and  $0.6$ ) takes place at almost the same time of around 10 s. This is probably linked to the inhomogeneity of the dDRX microstructure illustrated in Fig. 62 above. The effect of purity on the  $D$ - $t'$  curves for dDRX copper ( $\varepsilon = 0.6$ ) is displayed in Fig. 64b. In the 3N and 4N copper, the  $D$ - $t'$  relations can be approximated by two lines of almost identical slope. The rate of coarsening in the 6NCu is nearly the same, with the important difference being that the 6N grain sizes are consistently about twice those in the 3N and 4NCu. This is in keeping with the high purity of the former material.

Some experiments carried out on an interstitial free (IF) steel deformed into the dDRX range and then annealed are illustrated in Fig. 65 [291]. Here the ferrite grain size after transformation is plotted against the time of annealing in the austenite ( $D_\alpha$ - $t$ ). The softening  $X$ - $t$  curves for the austenite are displayed in Fig. 65b. After a prestrain of  $0.19$ , there is about 20% recovery, followed by SRX after an incubation time of several seconds. Softening goes to completion in about 100 s. The austenite grain sizes produced by recrystallization were not determined in this work, but it can be surmised that there was coarsening after SRX in the time interval from 100 to 5000 s.

After a prestrain of  $0.8$ , that is, after deformation well into the dDRX region, by contrast, there is about 60% softening by recovery followed by mDRX at about 1 s. Such rapid softening is succeeded by a small amount of softening (about 10%) due to SRX, after an incubation time that is again about 5 or 6 s for a total of about 80% softening. Here it can be seen in Fig. 65a that the grain sizes resulting

**Table 7**

Deformation boundary conditions and their associated deformation microstructures and annealing mechanisms.

	Description of process	Boundary conditions	Deformation microstructure developed	Mechanism operating during annealing
1	Cold/warm deformation	$\varepsilon < 1 \sim 2, T < 0.5T_m$	Strain hardened original grains	dSRX <sup>a</sup>
2	Hot deformation	$\varepsilon < 1 \sim 2, T > 0.5T_m$	dDRX <sup>b</sup> grains	mDRX and dSRX
3	Severe plastic deformation	$\sim 3 < \varepsilon < \infty, 0 < T < T_m$	cDRX grains	cSRX

<sup>a</sup> dSRX is generally referred to as “recrystallization” or SRX.<sup>b</sup> dDRX is generally referred to as “dynamic recrystallization” or DRX.

from the austenite undergoing dDRX are somewhat finer than those formed from the work hardened austenite and also that grain coarsening in the dDRX austenite hardly takes place after long annealing times, because some recovered regions (see Fig. 62b) have dislocation densities that are too low to permit the nucleation of SRX.

### 5.3. Concluding remarks

We summarize here the annealing characteristics of conventionally strain-hardened materials (leading to SRX) and of the cDRX matrices produced during SPD. We also compare them with those observed after conventional dDRX during hot deformation. It can be concluded from the above discussion that three different types of annealing process operate depending on the nature of the deformed microstructure, as shown in Table 7. These are: (i) the discontinuous static recrystallization (dSRX) that takes place in strain-hardened materials deformed to strains of less than approx. 2; (ii) the mDRX and dSRX that follow dDRX in materials subjected to strains of less than approx. 2 during hot deformation; (iii) the cSRX that takes place in cDRX materials deformed to strains of at least 3 at ambient, warm and high temperatures. Thus the terminology associated with recrystallization processes, as shown in Table 7, has become considerably more complicated over the past fifty years. It now includes dDRX, mDRX, cDRX and cSRX, while for consistency SRX is referred to here as dSRX. The additional terms have resulted from the expansion of the boundary conditions associated with plastic deformation, in particular with those introduced in experiments on high temperature deformation and on SPD. The latter, in turn, have been driven by the scientific and technical interest in grain size reduction and control. The resulting annealing microstructures are compared in Fig. 66 in accordance with the analyses presented in Sections 3, 4 and 5.

The characteristics of the recrystallization ( $X_{\text{rex}}-t$ ) curves for the three types of deformation microstructure can be summarized as follows:

1. Conventionally strain-hardened materials recrystallize by means of nucleation and growth, leading to grain sizes in the range 10–1000  $\mu\text{m}$  after deformation to prior strains no greater than about 2. On a local scale, there are relatively high dislocation density regions and high strain (and orientation) gradients (Fig. 66a) that disappear when recrystallization is complete. The  $X_{\text{rex}}-t$  curve (see Figs. 61 and 65) is of sigmoidal shape and approaches the value  $X_{\text{rex}} = 1$  on full recrystallization. During SRX, the microstructure is composed of a mixture of recrystallized and strain hardened grains (see Fig. 1). After full recrystallization (Fig. 66d), normal grain coarsening can take place. All of these phenomena have been frequently studied and reviewed [e.g. 1–5].
2. After deformation to strains of 3 or more by SPD, the cDRX microstructure is converted homogeneously into UFGs 0.01 to 1  $\mu\text{m}$  in diameter. This microstructure contains some nonequilibrium HABs and high dislocation densities in the grain interiors (Fig. 66b). After long annealing times, softening is incomplete and falls in the range  $0.9 < X_{\text{soft}} < 1$  (Fig. 55). The UFG microstructures produced in this way only undergo limited grain coarsening, which is accompanied by transformations of the nonequilibrium boundaries into equilibrium ones. As the texture does not change during annealing, cSRX is considered to be a single-step process. Thus cSRX differs from conventional SRX (a two-step nucleation and growth process) in that it takes place homogeneously throughout the UFG microstructure produced under cDRX conditions. After full recrystallization by cSRX (Fig. 66e), normal grain coarsening can take place.

3. The microstructures developed under dDRX conditions are composed of inhomogeneous dislocation substructures that vary from grain to grain (Fig. 66c, see also Fig. 62). A typical  $X-t$  curve (see Fig. 61) is characterized by three distinct stages and remains incomplete in commercial metals and alloys even after long annealing times. Stage 1 corresponds to static recovery and the beginning of mDRX. The softening in stage 2 results principally from mDRX, i.e. the continued growth of recently nucleated dDRX grains. In stage 3, not always observed, there may be further softening by dSRX, which requires a relatively long incubation time. Long annealing times lead to the continued presence of recovered grains containing dislocation densities that are too low for the nucleation of new grains (Fig. 66f). This process produces microstructures that are finer than those resulting from SRX in conventionally strain-hardened materials, but coarser than those produced by the cSRX of cDRX microstructures.

## 6. Summary of dynamic and post-dynamic recrystallization

### 6.1. Dynamic recrystallization

At temperatures above  $0.5T_m$ , the strain hardening produced by plastic deformation is counteracted by dynamic restoration processes, such as dynamic recovery (DRV) and dynamic recrystallization (DRX). The latter leads to strain softening at high strains, as described in the previous sections. The state of understanding regarding DRX and DRV up to around 1980 was summarized above in Table 1 [13,15,20]. In materials of low to medium SFE (deformation conditions under which DRV is not particularly rapid), the dislocation density increases to a high level and eventually the local differences in density are high enough to permit the nucleation of new grains, followed by the long-range migration of high angle boundaries (HABs). Such conventional DRX is considered to be a two-step phenomenon and is therefore sometimes referred to as discontinuous DRX (dDRX). In high SFE materials, by contrast, the rearrangement and annihilation of dislocations readily take place through DRV, leading to the formation of subgrains in the pancaked original grains. Under these conditions, the deformation is controlled mainly by DRV.

Recently, it has been shown that, even when only DRV is operating, new grain structures can evolve at very large strains, not only under hot working conditions, but even during straining at warm and cold temperatures. This can occur in both low and high SFE materials. The mechanisms involved, as described in detail in Section 4, can be considered as strain-induced *continuous* reactions that essentially take place homogeneously through the whole volume. This phenomenon is therefore referred to as continuous DRX (cDRX) and is essentially a *one-step* phenomenon. The regions of deformation temperature ( $T/T_m$ ) within which cDRX and dDRX operate were summarized in Table 2 [4,25,30]. Here it was concluded that cDRX takes place in all metals and alloys irrespective of their SFE as long as  $(T/T_m) < 0.5$ . When  $(T/T_m) > 0.5$ , only dDRX operates in low to medium SFE materials and only cDRX in high SFE materials.

The characteristics of dDRX and cDRX considered in Sections 3 and 4 are summarized in Table 8. Here it can be seen that the flow behavior and the mechanism of new grain formation under cDRX conditions clearly differ from those pertaining to conventional dDRX. An important difference involves the critical strain  $\varepsilon_c$  for the nucleation of new grains. During conventional dDRX, the  $\varepsilon_c$  is located well before the strain at which the stress peak appears in the flow curve; it depends sensitively, not only on temperature and strain rate, but also on the initial grain size (e.g. Fig. 6) [13,15,20]. During cDRX, on the other hand, the  $\varepsilon_c$  corresponds to the initiation strain of the second stage in the  $\theta_{AV}-\Sigma\varepsilon$  curve (e.g. Figs. 36, 41 and 52). Here MSBs begin to appear, resulting in the formation of microcrystallites bounded by HABs at their intersections and along the bands. It should be noted that the  $\varepsilon_c$  for cDRX does not particularly depend on temperature and strain rate. The characteristics summarized in Table 8 indicate that cDRX involves the operation of both athermal and thermal processes, as discussed in Section 4. Conventional dDRX, by contrast, is essentially thermal in nature, as it is largely controlled by lattice diffusion. It is also of interest to note from Table 8 that two different annealing processes operate after deformation: continuous static recrystallization (cSRX) in the matrices affected by cDRX and mDRX in those subjected to dDRX, as discussed in Section 5.3. The annealing behavior after DRX is considered in more detail in the next section.

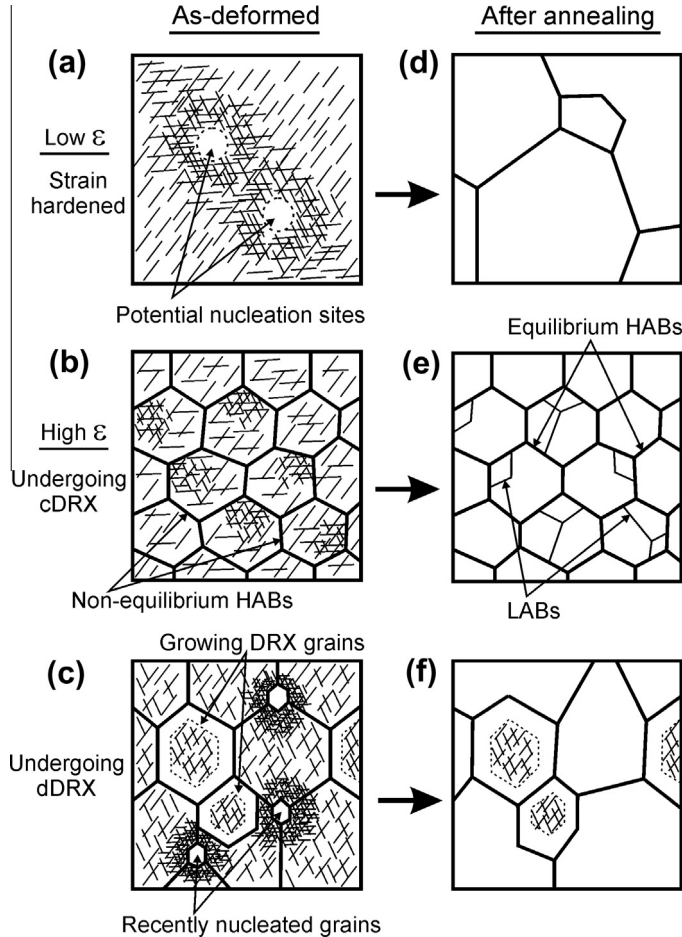


**Fig. 66.** Schematic representations of the three types of as-deformed microstructure discussed in Section 5: (a) strain-hardened microstructure produced by deformation to strains of 1 to 2, (b) UFG microstructure developed by cDRX as a result of deformation to strains above 3, and (c) dDRX microstructure produced by hot deformation. On the right hand sides, the respective microstructures developed by annealing are shown in (d)–(f). The hatched and blank regions contain dislocations and are dislocation-free, respectively. Thick and thin lines represent HABs and LABs, respectively.

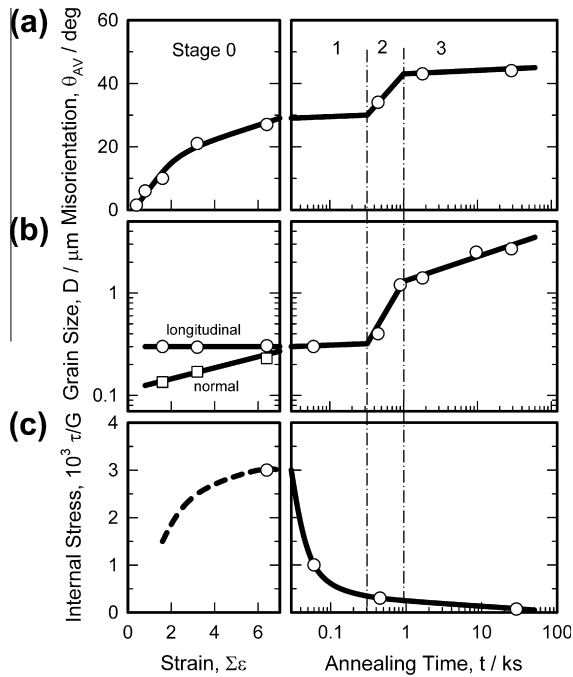
## 6.2. Post – dynamic recrystallization

The strain-hardened microstructures formed at strains below 1–2 are generally restored by static recovery (SRV) and dSRX during annealing; this leads to the formation of new dislocation-free grains after long annealing times. The process of dSRX involves the nucleation of new grains followed by the long-range migration of HABs. During the operation of this process, there are clear boundaries between the new grains and the remaining strain-hardened regions. By contrast, the ultrafine grained microstructures developed by severe plastic deformation (SPD) at strains above 3 are composed of a fairly uniform network of HABs as well as of a high density of dislocations distributed over the entire volume. This is brought about by the operation of cDRX, as discussed in Section 4. Such UFG microstructures containing HABs have the appearance of ones that have been conventionally recrystallized when examined by optical and orientation imaging microscopy (see Figs. 4, 38 and 42) even though their HABs are in a nonequilibrium state. During subsequent annealing, the nonequilibrium HABs

**Table 8**

Comparison of the characteristics of discontinuous (dDRX) and continuous (cDRX) dynamic recrystallization.

Type of dynamic recrystallization	dDRX	cDRX
<b>Conditions</b>		
Strain	Strain beyond $\varepsilon_c$ ( $<1$ )	Large strains above 3
Temperature ( $T/T_m$ )	Above 0.5	0–1
Stacking fault energy (SFE)	Low and medium	Low to high
<b>Flow behavior</b>		
Flow stress behavior	Steady-state flow following single or multiple peak flow	Pseudo steady-state flow following gradual strain hardening
Effect of temperature ( $T/T_m$ ) or strain rate ( $\dot{\varepsilon}$ )	Thermally activated flow assisted by lattice diffusion, resulting in the appearance of reversible flow	Mixed athermal and thermal behavior, resulting in the appearance of irreversible flow
<b>Microstructures</b>		
Nucleation sites and the critical strain for nucleation ( $\varepsilon_c$ )	Nuclei form mostly along grain boundaries. $\varepsilon_c$ depends on $T$ , $\dot{\varepsilon}$ and initial grain size	Microcrystallites form within MSBs. $\varepsilon_c$ does not depend on $T$ or $\dot{\varepsilon}$
Characteristics of the dislocation substructures	Substructures vary from grain to grain and develop inhomogeneously	UFGs surrounded by nonequilibrium HABs; dislocation substructures develop homogeneously
Annealing behavior	mDRX and dSRX	cSRX

**Fig. 67.** Effect of MDF a 304 stainless steel at 873 K and annealing at 973 K on (a) average sub-boundary misorientation  $\theta_{AV}$ , (b) average grain size  $D$ , and (c) internal stress  $\tau/G$  (see also Fig. 58) [201].

are transformed into equilibrium ones. This takes place by the recovery as well as the short-range migration of the boundaries over the entire volume; that is, there is no recognizable nucleation and growth of new grains (e.g. Figs. 56, 59 and 60). This type of post-deformation adjustment is essentially a type of recovery, and has been termed continuous SRX (cSRX). The features of such continuous processes suggest that there is a close connection between the operation of cDRX during deformation and that of cSRX during the annealing of strain-induced UFG microstructures, as both involve the

rearrangement of dislocations. This was considered in Section 5 where the results obtained on a 304 austenitic stainless steel that was severely deformed at 873 K and subsequently isothermally annealed at 973 K were discussed (see Figs. 58 and 59) [201,204].

The changes in grain- and sub-boundary misorientation  $\theta_{AV}$ , grain and subgrain size  $D$ , and internal stress  $\tau/G$  during deformation and subsequent annealing of an UFG 304 stainless steel are presented together in Fig. 67 [201,204]. The three annealing stages, i.e. recovery in stage 1, rapid grain coarsening in stage 2, and slow grain coarsening in stage 3, are similar to those observed in UFG Cu and Mg alloys (Figs. 56, 58 and 60). Thus the process of SPD can be considered to correspond to a prior stage 0 in the process of new grain formation, as shown in Fig. 67. During deformation,  $\theta_{AV}$  gradually increases from zero as sub-boundaries form; it finally attains a mean value of  $30^\circ$ , signifying that HABs have been developed. The fine grains that appear in this way are more equiaxed than the preceding subgrains. They are also accompanied by the development of high internal stresses. Concurrently,  $D$  does not change significantly.

During subsequent annealing, there is little change in either  $\theta_{AV}$  or  $D$  in stage 1, while the internal stresses are essentially released by the operation of SRV. This results in the transformation of the HABs from being in a nonequilibrium to an equilibrium state (Figs. 58 and 59). Stage 2 is then characterized by the rapid increase in both  $\theta_{AV}$  and  $D$  over a short interval of time. In this stage, the denser dislocation substructures including subgrains with LABs are consumed by the growing grains with HABs [201]. During stage 3, further annealing leads to further grain coarsening, but at a lower rate, while  $\theta_{AV}$  remains approximately constant.

### 6.3. Concluding remarks

Static recrystallization (i.e. dSRX here) is a phenomenon in which new dislocation-free grains appear in strain-hardened metals and alloys during annealing [e.g. 1–6]. Here, there is a distinct break between the deformation and annealing stages in the process of new grain formation. By contrast, during SPD, new grains form *during* deformation without the application of an annealing treatment. These strain-induced fine grains are surrounded by non-equilibrium HABs, which can however be transformed into equilibrium HABs if a further annealing treatment is applied. The principal distinction between new grain formation under dSRX and cDRX conditions is then that the HABs are formed *during annealing* in the former case, while they are formed *during deformation* under SPD conditions.

The above discussion regarding new grain formation as a result of plastic deformation and subsequent annealing is summarized in Table 9. As can be seen, the formation of new HABs takes place during annealing after low strain (conventional) deformation and during deformation in the high strain (SPD) case. Some further small differences are involved, which are summarized below.

**Table 9**

Effect of plastic strain on dSRX and cSRX taking place during the integrated processes of (1) deformation and (2) subsequent annealing.

Process	Range of strain	
	Low strains ( $\varepsilon < 1-2$ )	Very large strains ( $\varepsilon > 3-\infty$ )
(1) Deformation	Nucleation sites develop inhomogeneously in strain-hardened matrices as a result of DRV $\Delta X_{deform}^a \approx 0$	Microcrystallites with non-equilibrium HABs evolve relatively homogeneously as a result of cDRX $0.9 < \Delta X_{deform} < 1.0$
(2) Annealing	Nucleation of new grains with HABs by SRV followed by the long-range migration of HABs; this occurs inhomogeneously and is a two-step reaction known as <b>dSRX</b> $\Delta X_{anneal} \approx 1$	Nonequilibrium HABs transform into equilibrium ones and the short-range migration of HABs occurs homogeneously; this is a one-step reaction and is referred to as <b>cSRX</b> $0 < \Delta X_{anneal} < 0.1$

<sup>a</sup> Here  $\Delta X$  refers to the volume fraction of new grains produced during the process of interest. The sum of the two volume fractions,  $\Delta X_{deform}$  and  $\Delta X_{anneal}$ , is set equal to 1. Values of  $\Delta X_{deform}$  for the “very large strain” case, i.e. for cSRX, can be determined from experiments such as those of Figs. 4c and 67.

1. In both cases, the nuclei of new grains are introduced into materials by plastic deformation. However, their conversion into full-fledged grains is different under dSRX (low strain) and cDRX (high strain) conditions. After low strains, the nuclei develop into new grains during subsequent annealing. They are separated from each other by distances of 10–1000  $\mu\text{m}$  and are distributed inhomogeneously. During high strain deformation, the fine new grains are introduced without annealing. However, they are enclosed by non-equilibrium HABs and contain high densities of dislocations. These are developed essentially homogeneously at intervals of less than 1  $\mu\text{m}$ .
2. During dSRX, the new grain distribution is inhomogeneous and involves the long-range migration of HABs. If a material containing fine grains formed by cDRX is annealed, only the short-range migration of HABs takes place and this occurs homogeneously. The non-equilibrium HABs produced by the prior deformation are converted into equilibrium HABs.
3. In summary then, the characteristics of the new grains resulting from deformation and annealing are determined mainly by the deformation (low strain vs. high strain) and not by the annealing conditions. After low strains, the annealing treatment plays the most important role in the formation of new grains; conversely, deformation plays the dominant role in new grain formation under SPD conditions.

#### 6.4. Topics for further investigation

The microstructures and dislocation substructures developed dynamically under dDRX and cDRX conditions differ considerably from each other, as summarized in Table 8. The substructures in dDRX grains vary from grain to grain and so are distributed inhomogeneously. By contrast, those in cDRX grains are nearly homogeneous. The annealing behaviors after deformation are also quite different in the deformation microstructures developed by dDRX and cDRX, as described in Fig. 66. In spite of the considerable effort made in investigating the microstructural features produced by the two types of dynamic recrystallization reviewed here, some important aspects remain to be clarified.

1. The application of cDRX and dDRX to microstructure control should be studied more systematically, particularly in materials not subject to allotropic transformation, i.e. in most of the nonferrous metals and alloys as well as in ferritic steels and austenitic alloy steels. The microstructure control techniques employed to date in these materials have been limited almost entirely to static annealing following cold working. Specific methods of grain refinement applicable to particular alloy systems should be developed using the principles of dDRX and cDRX processing, as appropriate.
2. There are several unresolved topics requiring clarification with respect to the dynamic evolution of the strain-induced grains produced by cDRX.
  - How do MSBs control the formation of UFGs? Why do they develop and how can their characteristics be controlled?
  - How do metallurgical parameters such as grain size and second phase particles affect the formation of MSBs?
  - What is the role of deformation twinning in producing grain refinement by cDRX?
3. It is known from Table 2 that new grain formation through cDRX takes place at all values of SFE at  $(T/T_m) < 0.5$ . However, the effect of SFE on cDRX should be studied in more detail. For example:
  - In high SFE materials, new grain formation through cDRX takes place at all values of  $T/T_m$  from 0 to 1. How do the characteristics of cDRX change over this temperature range?
  - Is there a relationship between flow stress and average grain size in materials with high SFE that is analogous to those observed in materials with low SFE, e.g. in Figs. 49 and 50.

#### Acknowledgements

The authors are indebted to the following colleagues for numerous stimulating discussions: Drs. F. Musin (Ufa State Aviation Technical University, Russia), M. Ohashi (Keihin Hatsujyo Co., Japan),

E.I. Poliak (ArcelorMittal Global Research and Development, US), O. Sitdikov (Institute for Metals Superplasticity Problems, Russia), A.M. Wusatowska-Sarnek (Pratt & Whitney, USA), J. Xing (Nippon Light Metal Co., Japan), S. Zherebtsov (Belgorod State University, Russia) as well as to Professors G. Gottstein (RWTH Aachen University, Germany), N. Hansen (Technical University of Denmark, Denmark), K. Higashida (Kyushu University, Japan), P.D. Hodgson (Deakin University, Australia), Z. Horita (Kyushu University, Japan), F.J. Humphreys (University of Manchester, UK), H.J. McQueen (Concordia University, Canada), F. Montheillet (Ecole des Mines de Saint-Etienne, France), G.A. Salishchev (Belgorod State University, Russia), C.M. Sellars (Sheffield University, UK), L.S. Toth (Universite de Lorraine, France), N. Tsuji (Kyoto University, Japan), K. Tsuzaki (National Institute for Materials Science, Kyushu University, Japan), M. Umemoto (Toyoashi University of Technology, Japan), R.Z. Valiev (Ufa State Aviation Technical University, Russia), X. Yang (Central South University, China) and S. Yue (McGill University, Canada). The authors are grateful to Ms. E. Lashina (Belgorod State University, Russia) for her assistance with figure preparation. They also acknowledge with gratitude the financial support received from the following sources: the Ministry of Education, Science and Culture (Grant-in Aid for Scientific Research), the Light Metals Education Foundation, Japan (T.S. and H.M.); the Ministry of Education and Science, Russia (A.B. and R.K., project No. OK-591/0402-13); the Natural Sciences and Engineering Research Council of Canada and the Canadian Steel Industry Research Association (J.J.J.).

## References

- [1] Burke JE, Turnbull D. Recrystallization and grain growth. *Prog Met Phys* 1952;3:220–92.
- [2] Cahn RW. Recrystallization mechanisms. In: Margolin H, editor. *Recrystallization, grain growth and textures*. Ohio: ASM; 1966. p. 99–127.
- [3] Haessner F, editor. *Recrystallization of metallic materials*. Stuttgart: Dr. Riederer-Verlag, GmbH; 1978.
- [4] Humphreys FJ, Hatherly M. *Recrystallization and related annealing phenomena*. 2nd ed. Oxford: Elsevier; 2004.
- [5] Doherty RD, Hughes DA, Humphreys FJ, Jonas JJ, Juul Jensen D, Kassner ME, et al. Current issues in recrystallization: a review. *Mater Sci Eng* 1997;A238:219–74.
- [6] Bailey JE, Hirsch PB. The recrystallization process in some polycrystalline metals. *Proc Roy Soc (Lond)* 1962;A267:11–30.
- [7] Miura H, Sakai T, Belyakov A, Gottstein G, Crumbach M, Verhassel J. Static recrystallization of SiO<sub>2</sub>-particle containing {011}<100> copper single crystals. *Acta Mater* 2003;51:1507–15.
- [8] Ahlborn H, Hornbogen E, Koster U. Recrystallisation mechanism and annealing texture in aluminium–copper alloys. *J Mater Sci* 1969;4:944–50.
- [9] Hornbogen E, Koster U. Recrystallization of two-phase alloys. In: Haessner F, editor. *Recrystallization of metallic materials*. Stuttgart: Dr. Riederer-Verlag, GmbH; 1978. p. 159–94.
- [10] Dimitrov O, Fromageau R, Dimitrov C. Effects of trace impurities on recrystallization phenomena. In: Haessner F, editor. *Recrystallization of metallic materials*. Stuttgart: Dr. Riederer-Verlag, GmbH; 1978. p. 137–57.
- [11] Hardwick D, Sellars CM, Tegart WJ. Structural changes during the deformation of copper, aluminium and nickel at high temperatures and high strain rates. *J Inst Met* 1961;90:17–22.
- [12] Jonas JJ, Sellars CM, Tegart WJ, McG. Strength and structure under hot-working conditions. *Metal Rev* 1969;14:1–24.
- [13] McQueen HJ, Jonas JJ. Recovery and recrystallization during high temperature deformation. In: *Arsenault RJ, editor. Treatise on materials science and technology, vol. 6*. New York: Academic Press; 1975. p. 393–493.
- [14] Sakui S, Sakai T, Takeishi K. Hot deformation of austenite in a plain carbon steel. *Trans ISIJ* 1977;17:718–25.
- [15] Sellars CM. Recrystallization of metals during hot deformation. *Philos Trans Roy Soc Lond A* 1978;288:147–58.
- [16] Mecking H, Gottstein G. Recovery and recrystallization during deformation. In: Haessner F, editor. *Recrystallization of metallic materials*. Stuttgart: Dr. Riederer-Verlag, GmbH; 1978. p. 195–222.
- [17] Sakai T, Ohashi M. Dislocation substructures developed during dynamic recrystallization in polycrystalline nickel. *Mater Sci Technol* 1990;6:1251–7.
- [18] Sakai T. Dynamic recrystallization microstructures under hot working conditions. *J Mater Process Technol* 1995;53:349–61.
- [19] Maki T, Akasaka K, Okuno K, Tamura I. Dynamic recrystallization of austenite in 18-8 stainless steels and 18Ni maraging steel. *Trans ISIJ* 1982;22:253–61.
- [20] Sakai T, Jonas JJ. Dynamic recrystallization – mechanical and microstructural considerations. *Acta Metall* 1984;32:189–209.
- [21] Derby B. The dependence of grain size on stress during dynamic recrystallization. *Acta Metall Mater* 1991;39:955–62.
- [22] Belyakov A, Miura H, Sakai T. Dynamic recrystallization under warm deformation of a 304 type austenitic stainless steel. *Mater Sci Eng A* 1998;A255:139–47.
- [23] Gao W, Belyakov A, Miura H, Sakai T. Dynamic recrystallization of copper polycrystals with different purities. *Mater Sci Eng A* 1999;A265:233–9.
- [24] Ponge D, Gottstein G. Necklace formation during dynamic recrystallization: mechanisms and impact on flow behavior. *Acta Mater* 1998;46:69–80.
- [25] Sakai T, Jonas JJ. Plastic deformation: role of recovery and recrystallization. In: Buschow KH, Cahn RW, Flemings MC, Iilschner B, Kramer EJ, Mahajan S, editors. *Encyclopedia of materials: science and technology, vol. 7*. Oxford: Elsevier; 2001. p. 7079–84.

- [26] Solberg JK, McQueen HJ, Ryum N, Nes E. Influence of ultra-high strains at elevated temperatures on the microstructure of aluminium. Part I. *Philos Mag A* 1989;60:447–71.
- [27] Sales SJ, McNeley TR, McQueen HJ. Recrystallization and superplasticity at 300 °C in an aluminum–magnesium alloy. *Metall Trans* 1991;22A:1037–47.
- [28] Qing L, Xiaoxu H, Mei Y, Jinfeng Y. On deformation-induced continuous recrystallization in a superplastic Al–Li–Cu–Mg–Zr alloy. *Acta Metall Mater* 1992;40:1753–62.
- [29] Belyakov A, Kaibyshev R. Structural changes in a ferritic steel during hot deformation. *Phys Met Metallogr* 1994;78:91–7.
- [30] Valiev RZ, Islamgaliev RK, Alexandrov IV. Bulk nanostructured materials from severe plastic deformation. *Prog Mater Sci* 2000;45:103–89.
- [31] Tsuzaki K, Xiaoxu H, Maki T. Mechanism of dynamic continuous recrystallization during superplastic deformation in a microduplex stainless steel. *Acta Mater* 1996;44:4491–9.
- [32] Tsuji N, Matsubara Y, Saito Y. Dynamic recrystallization of ferrite in interstitial free steel. *Scripta Mater* 1997;37:477–84.
- [33] Gourdet S, Montheillet F. An experimental study of the recrystallization mechanism during hot deformation of aluminum. *Mater Sci Eng A* 2000;A283:274–88.
- [34] Galiyev A, Kaibyshev R, Gottstein G. Correlation of plastic deformation and dynamic recrystallization in magnesium alloy ZK60. *Acta Mater* 2001;49:1199–207.
- [35] Sitdikov O, Kaibyshev R. Dynamic recrystallization in pure magnesium. *Mater Trans* 2001;42:1928–37.
- [36] Gourdet S, Montheillet F. A model of continuous dynamic recrystallization. *Acta Mater* 2003;51:2685–99.
- [37] Musin F, Belyakov A, Kaibyshev R, Motohashi Y, Itoh G, Tsuzaki K. Microstructure evolution in a cast 1421Al alloy during hot equal-channel angular extrusion. *Rev Adv Mater Sci* 2010;25:107–12.
- [38] Belyakov A, Kaibyshev R. Deformation mechanisms in a high-chromium ferritic steel: I. Phenomenological analysis. *Phys Met Metallogr* 1994;78:240–5.
- [39] Belyakov A, Miura H, Sakai T. Dynamic recrystallization in ultra fine-grained 304 stainless steel. *Scripta Mater* 2000;43:21–6.
- [40] Luton MJ, Sellars CM. Dynamic recrystallization in nickel and nickel–iron alloys during high temperature deformation. *Acta Metall* 1969;17:1033–43.
- [41] Weiss I, Jonas JJ. Interaction between recrystallization and precipitation during the high temperature deformation of HSLA steels. *Metal Trans A* 1979;10A:831–40.
- [42] Sakai T, Miura H, Muramatsu N. Effect of small amount of Co on dynamic recrystallization of Cu–Be Alloys. *Mater Trans JIM* 1995;36:1023–30.
- [43] Belyakov A, Wei FG, Tsuzaki K, Kimura Y, Mishima Y. Incomplete recrystallization in cold worked steel containing TiC. *Mater Sci Eng A* 2007;A471:50–6.
- [44] Glover G, Sellars CM. Recovery and recrystallization during high temperature deformation of  $\alpha$ -iron. *Metall Trans* 1973;4:765–75.
- [45] Yamagata H. Dynamic recrystallization and dynamic recovery in pure aluminum at 583 K. *Acta Metall Mater* 1995;43:723–9.
- [46] Belyakov A, Gao W, Miura H, Sakai T. Strain induced grain evolution in polycrystalline copper during warm deformation. *Metall Mater Trans A* 1998;29A:2957–65.
- [47] Belyakov A, Sakai T, Miura H, Kaibyshev R. Grain refinement under multiple warm deformation in 304 type austenitic stainless steel. *ISIJ Int* 1999;39:592–9.
- [48] Belyakov A, Sakai T, Miura H, Tsuzaki K. Grain refinement in copper under large strain deformation. *Philos Mag A* 2001;81:2629–43.
- [49] Kuhlmann-Wilsdorf D, Hansen N. Geometrically necessary, incidental and subgrain boundaries. *Scripta Metall Mater* 1991;25:1557–62.
- [50] Belyakov A, Tsuzaki K, Miura H, Sakai T. Effect of initial microstructures on grain refinement in a stainless steel by large strain deformation. *Acta Mater* 2003;51:847–61.
- [51] Sitdikov O, Sakai T, Avtokratova E, Kaibyshev R, Kimura Y, Tsuzaki K. Grain refinement in a commercial Al–Mg–Sc alloy under hot ECAP conditions. *Mater Sci Eng A* 2007;A444:18–30.
- [52] Mazurina I, Sakai T, Miura H, Sitdikov O, Kaibyshev R. Effect of deformation temperature on microstructure evolution in aluminum alloy 2219 during hot ECAP. *Mater Sci Eng A* 2008;A486:662–71.
- [53] Sitdikov O, Sakai T, Miura H, Hama C. Temperature effect on fine-grained structure formation in high-strength Al alloy 7475 during hot severe deformation. *Mater Sci Eng A* 2009;A516:180–8.
- [54] Belyakov AN, Kaibyshev RO. Structural changes in corrosion-resistant steels during hot deformation. *Met Sci Heat Treat* 1992;34:324–9.
- [55] Zharebtsov SV, Salishchev GA, Galeyev RM, Valiakhetmetov OR, Mironov SY, Semiatin SL. Production of submicrocrystalline structure in large-scale Ti–6Al–4V billet by warm severe deformation processing. *Scripta Mater* 2004;51:1147–51.
- [56] Mironov S, Murzinova M, Zharebtsov S, Salishchev GA, Semiatin SL. Microstructure evolution during warm working of Ti–6Al–4V with a colony- $\alpha$  microstructure. *Acta Mater* 2009;57:2470–81.
- [57] Zharebtsov S, Murzinova M, Salishchev G, Semiatin SL. Spheroidization of the lamellar microstructure in Ti–6Al–4V alloy during warm deformation and annealing. *Acta Mater* 2011;59:4138–50.
- [58] Zharebtsov SV, Galeyev RM, Salishchev GA, Myshlyaev MM. Formation of submicrocrystalline structure in a VT30 titanium alloy. *Phys Met Metallogr* 1999;87:318–23.
- [59] Miura H, Aoyama H, Sakai T. Grain boundary misorientation effect on dynamic recrystallization of Cu–Si bicrystals. *J Jpn Inst Met* 1994;58:267–75.
- [60] Miura H, Sakai T, Mogawa R, Jonas JJ. Nucleation of dynamic recrystallization and variant selection in copper bicrystals. *Philos Mag* 2007;87:4197–209.
- [61] Belyakov A, Miura H, Sakai T. Dynamic recrystallization under warm deformation of polycrystalline copper. *ISIJ Int* 1998;38:595–601.
- [62] Wusatowska-Sarnek AM, Miura H, Sakai T. Nucleation and microtexture development under dynamic recrystallization of copper. *Mater Sci Eng* 2002;A323:177–86.

- [63] Belyakov A, Miura H, Sakai T. Dynamic recrystallization under warm deformation of a 304 type austenitic stainless steel. *Mater Sci Eng* 1998;A255:139–47.
- [64] Miura H, Sakai T, Andiarwanto S, Jonas JJ. Nucleation of dynamic recrystallization at triple junctions in polycrystalline copper. *Philos Mag* 2005;85:2653–69.
- [65] Montheillet F, Cohen M, Jonas JJ. Axial stresses and texture development during the torsion testing of Al, Cu and  $\alpha$ -Fe. *Acta Metall* 1984;32:2077–89.
- [66] Ohashi M, Endo T, Sakai T. Effect of initial grain size on the dynamic recrystallization of nickel. *J Jpn Inst Met* 1990;54:435–41.
- [67] Sakai T, Akben MG, Jonas JJ. Dynamic recrystallization during the transient deformation of a vanadium microalloyed steel. *Acta Metall* 1983;31:631–42.
- [68] Frommert M, Gottstein G. Mechanical behavior and microstructure evolution during steady-state dynamic recrystallization in the austenitic 800H. *Mater Sci Eng A* 2009;A506:101–10.
- [69] Xing J, Soda Y, Yang X, Miura H, Sakai T. Ultra-fine grain development in magnesium alloy AZ31 during severe large forging under decreasing temperature conditions. *Mater Trans* 2005;46:1646–50.
- [70] Yang X, Miura H, Sakai T. Dynamic evolution of new grains in magnesium alloy AZ31 during hot deformation. *Mater Trans* 2003;44:197–203.
- [71] Bowden JW, Samuel FH, Jonas JJ. Effect of interpass time on austenite grain refinement by means of dynamic recrystallization of austenite. *Metall Trans A* 1991;22A:2947–57.
- [72] Cetlin PR, Yue S, Jonas JJ, Maccagno TM. Influence of strain rate on interpass softening during the simulated warm rolling of interstitial free steels. *Metall Trans A* 1993;24A:1543–53.
- [73] Jonas JJ. Effect of interpass time on the hot rolling behaviour of microalloyed steels. *Mater Sci Forum* 1998;284–286:3–14.
- [74] Jonas JJ. Effect of interpass time on dynamic and static softening during rolling. In: Lamberigts M, editor. 2nd international conference on thermomechanical processing of steels, TMP'2004. Dusseldorf: Stahl Eisen; 2004. p. 35–42.
- [75] Jonas JJ. Effect of quench and interpass time on dynamic and static softening during hot rolling. *Steel Res Int* 2005;76:392–8.
- [76] Pussegoda LN, Yue S, Jonas JJ. Laboratory simulation of seamless tube piercing and rolling using dynamic recrystallization schedules. *Metall Trans A* 1990;21A:153–64.
- [77] Pussegoda LN, Yue S, Jonas JJ, Hunt PJ. Development of dynamic recrystallization controlled rolling schedules during seamless tube rolling. In: Tither G, Zhang Z, editors. The second international conference on HSLA steels. Warrendale (PA): TMS; 1992. p. 159–63.
- [78] Pussegoda LN, Hodgson PD, Jonas JJ. Design of dynamic recrystallization controlled rolling schedules for seamless tube rolling. *Mater Sci Technol* 1992;8:63–71.
- [79] Maccagno TM, Yue S, Jonas JJ, Dyck K. Simulated hot working, cold working, and annealing of Al-containing steels. *Metall Trans A* 1993;24A:1589–96.
- [80] Maccagno TM, Jonas JJ. Correcting for the effects of static and metadynamic recrystallization during the laboratory simulation of rod rolling. *ISIJ Int* 1994;34:607–14.
- [81] Yue S, Roucoules C, Maccagno TM, Jonas JJ. Dynamic recrystallization in rod rolling. In: Korchynsky M, editor. Microalloying '95 conference proceedings. Pittsburgh (PA): Iron and Steel Society; 1995. p. 355–64.
- [82] Maccagno TM, Jonas JJ, Hodgson PD. Spreadsheet modelling of grain size evolution during rod rolling. *ISIJ Int* 1996;36:720–8.
- [83] Yue S, Roucoules C, Maccagno TM, Jonas JJ. Dynamic recrystallization in rod rolling. In: 37th MWSP conference proceedings, October 1995. Hamilton (Canada): Iron and Steel Society, Inc.; 1996. p. 651–60.
- [84] Hodgson PD, Jonas JJ, Yue S. Growth during and after the static and metadynamic recrystallization of austenite. *Mater Sci Forum* 1992;94–96:715–22.
- [85] Boratto F, Barbosa R, Yue S, Jonas JJ. Effect of chemical composition on the critical temperatures of microalloyed steels. In: Tamura I, editor. Proc int conf on phys metall of thermomechanical processing of steels and other metals (Thermec-88). Tokyo (Japan): Iron and Steel Institute of Japan; 1988. p. 383–90.
- [86] Boratto F, Yue S, Jonas JJ, Lawrence TH. Design of schedules for the production of high strength microalloyed steel strip in a hot Steckel mill. In: Tamura I, editor. Proc int conf on phys metall of thermomechanical processing of steels and other metals (Thermec-88). Tokyo (Japan): Iron and Steel Institute of Japan; 1988. p. 519–26.
- [87] Vervynck S, Verbeke K, Lopez B, Jonas JJ. The role of the non-recrystallization temperature ( $T_{nr}$ ) in HSLA steels. *Int Mater Rev* 2012;57:187–207.
- [88] Maccagno TM, Jonas JJ, Yue S, McCrady BJ, Slobodian R, Deeks D. Determination of recrystallization stop temperature from rolling mill logs and comparison with laboratory simulation results. *ISIJ Int* 1994;34:917–22.
- [89] Samuel FH, Yue S, Jonas JJ, Barnes KR. Effect of dynamic recrystallization on microstructural evolution during strip rolling. *ISIJ Int* 1990;30:216–25.
- [90] Jonas JJ. Dynamic recrystallization in hot strip mills. In: Chandra T, editor. Proc recrystallization '90. Warrendale (PA): TMS-AIME; 1990. p. 27–36.
- [91] Debray B, Teracher P, Jonas JJ. Simulation of the hot rolling and accelerated cooling of a C–Mn ferrite–bainite strip steel. *Metall Mater Trans A* 1995;26A:99–111.
- [92] Jonas JJ. Dynamic recrystallization in strip mills – industrial fact or metallurgical fiction? In: Proc on thermomechanical processing in theory, modelling and practice. Stockholm (Sweden): The Swedish Society for Materials Technology; 1997. p. 24–34.
- [93] Jonas JJ. Dynamic recrystallization in strip mills – industrial fact or metallurgical fiction? In: Chandra T, Sakai T, editors. International conference on thermomechanical processing of steels and other materials, THERMEC '97. Warrendale (PA): TMS; 1997. p. 31–45.
- [94] Siciliano Jr F, Jonas JJ. Modeling the critical strain for the initiation of dynamic recrystallization during the hot strip rolling of niobium microalloyed steels. *Mater Sci Forum* 1998;284–286:377–84.
- [95] Karjalainen PL, Maccagno TM, Jonas JJ. Softening and flow stress behavior of Nb microalloyed steels during hot rolling simulation. *ISIJ Int* 1995;35:1523–31.

- [96] Montheillet F, Jonas JJ. Recrystallization, dynamic. In: Trigg GL, editor. Encyclopedia of applied physics, vol. 16. New York (NY): American Institute of Physics; 1996. p. 205–25.
- [97] Jonas JJ, Barnett MR, Hodgson PD. Thermomechanical processing. In: Groza JR, Shackelford JF, Lavernia EJ, Powers MT, editors. Materials processing handbook. Handbook series. London (UK): Taylor & Francis; 2007. p. 29–1–29–26.
- [98] Hodgson PD, Jonas JJ, Davies CHJ. Modeling of hot and warm working of steels. In: Hakan Gür C, Pan J, editors. Handbook of thermal process modeling of steels. London (UK): Taylor & Francis; 2009. p. 225–64.
- [99] Montheillet F, Jonas JJ. Models of recrystallization. In: Handbook ASM, editor. Fundamentals of modeling for metals processing, vol. 22A. Materials Park (OH): AMS International; 2009. p. 220–31.
- [100] Samuel FH, Yue S, Jonas JJ. Dynamic and static recrystallization in plain carbon and microalloyed steels during hot rolling. In: Chandra T, editor. Proc recrystallization '90. Warrendale (PA): TMS-AIME; 1990. p. 325–30.
- [101] Pussegoda LN, Jonas JJ. Comparison of dynamic recrystallization and conventional controlled rolling schedules by laboratory simulation. *ISIJ Int* 1991;31:278–88.
- [102] Yue S, Bai DQ, Jonas JJ. The influence of static and dynamic recrystallization on mean flow stress and grain size in steel. *Can Metall Quart* 1994;33:145–54.
- [103] Jonas JJ. Influence of dynamic recrystallization on the hot rolling behaviour of steel. In: Kuhn LG, editor. 33rd Mechanical working and steel processing conference, vol. XXIX. Warrendale (PA): Iron and Steel Society of AIME; 1992. p. 359–62.
- [104] Najafizadeh A, Jonas JJ, Yue S. Effect of dynamic recrystallization on grain refinement of IF steels. *Mater Sci Forum* 1993;113–115:441–6.
- [105] Jonas JJ. Dynamic recrystallization – scientific curiosity or industrial tool? *Mater Sci Eng A* 1994;A184:155–65.
- [106] Jonas JJ, Maccagno TM, Yue S. The role of dynamic recrystallization in industrial hot working. In: Proc int symp on phase transformations during the thermomechanical processing of steel, 34th annual conference of metallurgists. Vancouver: CIM; 1995. p. 179–93.
- [107] Jonas JJ. Dynamic recrystallization scientific curiosity or industrial tool? In: Javier F Gil Mur, editor. Proc of congress of mechanical properties, Barcelona, Spain; 1996. p. 1–22.
- [108] Jonas JJ. Dynamic recrystallization: laboratory curiosity to industrial tool. In: Palmiere EJ, Mahfouf M, Pinna C, editors. Int conf on thermomechanical processing. Chesterfield (UK): BBR Solution Ltd; 2002. p. 2–8.
- [109] Wierzbinski SL, Guillet AM, Jonas JJ. Dynamic recrystallization of Cu–30Ni during hot compression. In: 5th Conf on plasticity of metals and alloys. Podbrezová: CSSR; 1988. p. 405–10.
- [110] Jiang L, Huang G, Godet S, Jonas JJ, Luo AA. Particle-stimulated nucleation of dynamic recrystallization in AZ31 alloy at elevated temperatures. *Mater Sci Forum* 2005;488–489:261–4.
- [111] Bocher Ph, Jonas JJ, Montheillet F. Nucleation and growth during dynamic recrystallization of a 304 stainless steel. In: McQueen HJ, Konopleva EV, Ryan ND, editors. Hot workability of steels and light alloys-composites. Montreal: The Metallurgical Society of CIM; 1996. p. 443–50.
- [112] Bocher Ph, Montheillet F, Jonas JJ. Microstructural evolution during the dynamic recrystallization of a 304 stainless steel. In: McNelley TR, editor. Proc third international conference on recrystallization and related phenomena. Monterey (CA): Monterey Institute of Advanced Studies; 1997. p. 355–62.
- [113] Bocher Ph, Jonas JJ. Characteristics of nucleation and growth during the dynamic recrystallization of a 304 stainless steel. In: Sakai T, Suzuki HG, editors. The 4th international conference on recrystallization and related phenomena. Sendai (Japan): The Japan Institute of Metals; 1999. p. 25–35.
- [114] Laasraoui A, Jonas JJ. Effect of dynamic recrystallization on the constitutive relations for flow during steel rolling. In: Lowe TC, Rollett AD, Follansbee PS, Daehn GS, editors. Modelling the deformation of crystalline solids. Warrendale (PA): The Minerals, Metals & Materials Society of AIME; 1991. p. 561–78.
- [115] Hildenbrand A, Tóth LS, Molinari A, Baczynski J, Jonas JJ. Self-consistent polycrystal modelling of dynamic recrystallization during the shear deformation of a Ti IF steel. *Acta Mater* 1999;47:447–60.
- [116] Cabrera JM, Prado JM, Jonas JJ. The dynamic recrystallization kinetics of a medium carbon microalloyed steel. In: McNelley TR, editor. Proc third international conference on recrystallization and related phenomena. Monterey (CA): Monterey Institute of Advanced Studies; 1997. p. 381–8.
- [117] Cho SN, Kang KB, Jonas JJ. The dynamic, static and metadynamic recrystallization of a Nb-microalloyed steel. *ISIJ Int* 2001;41:63–9.
- [118] Cho SH, Kang KB, Jonas JJ. Effect of manganese on recrystallization kinetics of niobium microalloyed steel. *Mater Sci Technol* 2002;18:389–95.
- [119] Stewart GR, Jonas JJ, Montheillet F. Kinetics and critical conditions for the initiation of dynamic recrystallization in 304 stainless steel. *ISIJ Int* 2004;44:1581–9.
- [120] Stewart GR, Elwazri AM, Yue S, Jonas JJ. Modeling of dynamic recrystallization kinetics in austenitic stainless and hypereutectoid steels. *Mater Sci Technol* 2006;22:519–24.
- [121] Stewart GR, Elwazri AM, Yue S, Jonas JJ. A kinetic model for dynamic recrystallization in austenitic stainless and hypereutectoid steels. *Mater Sci Technol* 2006;22:519–24.
- [122] Cho SH, Kang KB, Jonas JJ. Mathematical modeling of the recrystallization kinetics of Nb microalloyed steels. *ISIJ Int* 2001;41:766–73.
- [123] Jonas JJ, Quelennec X, Jiang L, Martin E. The Avrami kinetics of dynamic recrystallization. *Acta Mater* 2009;57:2748–56.
- [124] Quelennec X, Martin E, Jiang L, Jonas JJ. Work hardening and kinetics of dynamic recrystallization during the hot deformation of austenite. *J Phys Conf Ser* 2010;240:ID No. 012003/012082.
- [125] Quelennec X, Bozzolo N, Jonas JJ, Loge R. A new approach to modeling the flow curve of hot deformed austenite. *ISIJ Int* 2011;51:945–50.
- [126] Quelennec X, Jonas JJ. Simulation of austenite flow curves under industrial rolling conditions using a physical dynamic recrystallization model. *ISIJ Int* 2012;52:1145–52.
- [127] Jonas JJ, Quelennec X, Jiang L. Modeling the flow curve of hot deformed austenite. *Mater Sci Forum* 2012;715–716:81–8.
- [128] Mavropoulos T, Jonas JJ, Ruddle GE. Effect of boron on dynamic and static recrystallization in an ultra low carbon Nb steel. In: Proc conf on 'HSLA' steels '85. Beijing, China; 1985. p. 229–34.

- [129] Le Gall R, Jonas JJ. Solute drag effects during the dynamic recrystallization of nickel. *Acta Mater* 1999;47:4365–74.
- [130] Le Gall R, Bocher P, Verlinden B, Jonas JJ. Effect of solutes on the dynamic recrystallization microstructure of nickel. *J Phys* 2001;11:Pr477–82.
- [131] Le Gall R, Jonas JJ. Effects of solutes on kinetics, grain size and texture during the dynamic recrystallization of nickel. In: Chandra T, Higashi K, Suryanarayana C, Tome C, editors. Proceedings international conference on processing and manufacturing of advanced materials. Special Issue of *J Mater Process Technol* on CD ROM; 2001, 117/3.
- [132] Jonas JJ, Akben MG. Retardation of austenite recrystallization by solutes: a critical appraisal. *Metal Forum* 1981;4:92–101.
- [133] Roucoules C, Hodgson PD, Yue S, Jonas JJ. Dynamic and post-dynamic recrystallization in a Mo–Ti steel. In: DeArdo AJ, editor. Proc international conference on processing, microstructure and properties of microalloyed and other modern high strength low alloy steels. Warrendale (PA): AIME; 1991. p. 95–104.
- [134] Roucoules C, Yue S, Jonas JJ. Microstructural changes following dynamic recrystallization in microalloyed austenite. *Mater Sci Forum* 1993;113–115:455–60.
- [135] Roucoules C, Hodgson PD, Yue S, Jonas JJ. Softening and microstructural change following the dynamic recrystallization of austenite. *Metall Mater Trans A* 1994;25A:389–400.
- [136] Roucoules C, Yue S, Jonas JJ. Effect of alloying elements on metadynamic recrystallization in HSLA steels. *Metall Mater Trans A* 1995;26A:181–90.
- [137] Roucoules C, Yue S, Jonas JJ. Effect of dynamic and metadynamic recrystallization on rolling load and microstructure. In: Beynon JH, editor. 2nd International conference on modelling of metal rolling processes. London (UK): The Institute of Materials; 1993. p. 165–79.
- [138] Jonas JJ, Poliak EI, Najafizadeh A. The strain dependence of post-deformation softening during the hot compression of 304H stainless steel. *Mater Sci Forum* 2007;539–543:100–7.
- [139] Hodgson PD, Jonas JJ, Yue S. Strain accumulation and post-dynamic recrystallization in C–Mn steels. *Mater Sci Forum* 1993;113–115:473–8.
- [140] Najafizadeh A, Jonas JJ, Stewart GR, Poliak EI. The strain dependence of post-dynamic recrystallization in 304H stainless steel. *Metall Mater Trans A* 2006;37:1899–906.
- [141] Najafizadeh A, Jonas JJ. The strain-independence of interpass softening during the hot compression of 304 H stainless steel. *Mater Sci Forum* 2007;539–543:4932–7.
- [142] Dehghan-Manshadi A, Jonas JJ, Hodgson PD, Barnett MR. Correlation between the deformation and post-deformation behaviors of hot worked austenite. *ISIJ Int* 2008;48:208–11.
- [143] Mintz B, Jonas JJ, Yue S. The influence of dynamic recrystallization on the hot ductility of steels at low strain rates. In: Chandra T, editor. Proc recrystallization '90. Warrendale (PA): TMS-AIME; 1990. p. 553–8.
- [144] Mintz B, Abushosha R, Jonas JJ. Influence of dynamic recrystallization on the tensile ductility of steels in the temperature range 700 to 1150 °C. *ISIJ Int* 1992;32:241–9.
- [145] Baczynski J, Jonas JJ. Torsion textures produced by the dynamic recrystallization of a Ti IF steel. In: Liang Z, Zuo L, Chu Y, editors. Proc of the 11th conference on textures of materials (ICOTOM-11). Textures of materials, vol. 1. Beijing (China): International Academic Publishers; 1996. p. 387–92.
- [146] Baczynski J, Jonas JJ. Torsion textures produced by dynamic recrystallization in  $\alpha$ -iron and two interstitial-free steels. *Metall Mater Trans A* 1998;29A:447–62.
- [147] Jonas JJ, Tóth LS, Urabe T. Modelling the effects of static and dynamic recrystallization on texture development. *Mater Sci Forum* 1994;157–162:1713–30.
- [148] Baczynski J, Jonas JJ. Effect of dynamic recrystallization on texture development in a Ti–Nb IF steel. In: McNelley TR, editor. Proc third international conference on recrystallization and related phenomena. Monterey (CA): Monterey Institute of Advanced Studies; 1997. p. 339–46.
- [149] Baczynski J, DeArdo I, Jonas JJ. Dynamic recrystallization textures in ferrite and ferritic stainless steels. *Mater Sci Forum* 1998;273–275:465–70.
- [150] Bocher Ph, Azar J, Adams BL, Jonas JJ. Using OIM to interpret the dynamically recrystallized texture of a low stacking fault energy FCC material. *Mater Sci Forum* 1998;273–275:249–54.
- [151] Jonas JJ. Effect of austenite recrystallization on toughness of pipeline steels. *Mater Sci Forum* 2013;753:546–53.
- [152] Jonas JJ, Tóth LS. Modelling oriented nucleation and selective growth during dynamic recrystallization. *Scripta Metall Mater* 1992;27:1575–80.
- [153] Tóth LS, Jonas JJ. Modelling the texture changes produced by dynamic recrystallization. *Scripta Metall Mater* 1992;27:359–63.
- [154] Poliak EI, Jonas JJ. A one-parameter approach to determining the critical conditions for the initiation of dynamic recrystallization. *Acta Metall Mater* 1996;44:127–36.
- [155] Poliak EI, Jonas JJ. Initiation of dynamic recrystallization in constant strain rate hot deformation. *ISIJ Int* 2003;43:684–91.
- [156] Poliak EI, Jonas JJ. The critical strain for dynamic recrystallization. In: Palmiere EJ, Mahfouf M, Pinna C, editors. Int conf on thermomechanical processing. London (UK): Institute of Metals; 2002. p. 405–12.
- [157] Jonas JJ, Poliak EI. The critical strain for dynamic recrystallization in rolling mills. *Mater Sci Forum* 2003;426–432:57–66.
- [158] Poliak EI, Jonas JJ. Critical strain for dynamic recrystallization in variable strain rate hot deformation. *ISIJ Int* 2003;43:692–700.
- [159] Najafizadeh A, Jonas JJ. Predicting the critical stress for initiation of dynamic recrystallization. *ISIJ Int* 2006;46:1679–84.
- [160] Yada H, Matsumura Y, Senuma T. Massive type transformation induced by hot deformation in low carbon steels. In: Shimizu K, Tamura I, editors. Proc of the int conf on martensitic transformation. Sendai (Japan): Japan Institute of Metals; 1986. p. 515–20.
- [161] Yada H, Matsumura Y, Senuma T. A new thermomechanical heat treatment for grain refining in low carbon steels. In: Tamura I, editor. Proc 1st conf physical metallurgy of thermomechanical processing of steels and other metals (THERMEC-88). Tokyo (Japan): Iron and Steel Institute of Japan; 1988. p. 200–7.
- [162] Sun X, Luo H, Dong H, Liu Q, Weng Y. Microstructural evolution and kinetics for post-dynamic transformation in a plain low carbon steel. *ISIJ Int* 2008;48:994–1000.

- [163] Choi JK, Seo DH, Lee JS, Um KK, Choo WY. Formation of ultrafine ferrite by strain-induced dynamic transformation in plain low carbon steel. *ISIJ Int* 2003;43:746–54.
- [164] Jonas JJ, Ghosh C, Queleennec X, Basabe VV. The critical strain for dynamic transformation in hot deformed austenite. *ISIJ Int* 2013;53:145–51.
- [165] Ghosh C, Basabe VV, Jonas JJ. Determination of the critical strains for the initiation of dynamic transformation and dynamic recrystallization in four steels of increasing carbon contents. *Steel Res Int* 2013;84:490–4.
- [166] Jonas JJ, Ghosh C, Basabe VV. Effect of dynamic transformation on the mean flow stress. *Steel Res Int* 2013;84:253–8.
- [167] Segal VM, Reznikov VI, Drobyshevskij AE, Kopylov VI. Plastic metal working by simple shear. *Metally* 1981;1:115–23.
- [168] Humphreys FJ, Prangnell PB, Bowen JR, Gholinia A, Harris C. Developing stable fine-grained microstructures by large strain deformation. *Philos Trans Roy Soc Lond A* 1999;357:1663–81.
- [169] Valiev RZ, Estrin Y, Horita Z, Langdon TG, Zehetbauer MJ, Zhu YT. Producing bulk ultrafine-grained materials by severe plastic deformation. *JOM* 2006;58:33–9.
- [170] Valiev RZ, Langdon TG. The art and science of tailoring materials by nanostructuring for advanced properties using SPD techniques. *Adv Eng Mater* 2010;12:677–91.
- [171] Shrivastava SC, Jonas JJ, Canova G. Equivalent strain in large deformation testing: theoretical and practical considerations. *J Mech Phys Solids* 1982;30:75–90.
- [172] Zhilyaev AP, Langdon TG. Using high-pressure torsion for metal processing: fundamentals and applications. *Prog Mater Sci* 2008;53:893–979.
- [173] Salishchev GA, Valiakhetmetov OR, Galejev RM. Formation of submicrocrystalline structure in the titanium alloy VT8 and its influence on mechanical properties. *J Mater Sci* 1993;28:2898–902.
- [174] Saito S, Tsuji N, Utsunomiya H, Sakai T, Hong RG. Ultra-fine grained bulk aluminum produced by accumulative roll-bonding (ARB) process. *Scripta Mater* 1998;39:1221–7.
- [175] Tsuji N, Saito Y, Lee SH, Minamino Y. ARB (accumulative roll-bonding) and other new techniques to produce bulk ultrafine grained materials. *Adv Eng Mater* 2003;5:338–44.
- [176] Richert J, Richert M. A new method for unlimited deformation of metals and alloys. *Aluminium* 1986;62:604–7.
- [177] Kimura Y, Takaki S. Microstructural changes during annealing of work-hardened mechanically milled metallic powders. *Mater Trans JIM* 1995;36:289–96.
- [178] Koch CC. Synthesis of nanostructured materials by mechanical milling: problems and opportunities. *Nanostruct Mater* 1997;9:13–22.
- [179] Takayama Y, Miura T, Kato H, Watanabe H. Microstructural and textural evolution by continuous cyclic bending and annealing in a high purity titanium. *Mater Trans* 2004;45:2826–31.
- [180] Huang JY, Zhu YT, Jiang H, Lowe TC. Microstructures and dislocation configurations in nanostructured Cu processed by repetitive corrugation and straightening. *Acta Mater* 2001;49:1497–505.
- [181] Suh DW, Torizuka S, Ohmori A, Inoue T, Nagai K. Dynamic restoration process of Ni–30Fe alloy during hot deformation. *ISIJ Int* 2002;42:432–9.
- [182] Toth LS, Arzaghí M, Fundenberger JJ, Beausir B, Bouaziz O, Arruffat-Massion R. Severe plastic deformation of metals by high-pressure tube twisting. *Scripta Mater* 2009;60:175–7.
- [183] Embury JD, Keh AS, Fisher RS. Substructural strengthening in materials subjected to large plastic strains. *Trans AIME* 1966;236:1252–60.
- [184] Langford G, Cohen M. Microstructural analysis by high-voltage electron diffraction of severely drawn iron wires. *Metall Trans A* 1975;6A:901–10.
- [185] Gil Sevillano J, van Houtte P, Aernoudt E. Large strain work hardening and textures. *Prog Mater Sci* 1980;25:69–412.
- [186] Rybin VV. Large plastic deformations and destruction of metals. Moscow: Metallurgia; 1987.
- [187] Bay B, Hansen N, Hughes DA, Kuhlmann-Wilsdorf D. Evolution of f.c.c. deformation structures in polyslip. *Acta Metall Mater* 1992;40:205–19.
- [188] Liu Q, Juul Jensen D, Hansen N. Effect of grain orientation on deformation structure in cold-rolled polycrystalline aluminium. *Acta Mater* 1998;46:5819–38.
- [189] Belyakov A, Kaibyshev R. Structural changes of ferritic stainless steel during severe plastic deformation. *Nanostruct Mater* 1995;6:893–6.
- [190] Valiev RZ, Ivanisenko YuV, Rauch EF, Baudalet B. Structure and deformation behavior of Armco iron subjected to severe plastic deformation. *Acta Mater* 1996;44:4705–12.
- [191] Belyakov A, Sakai Y, Hara T, Kimura Y, Tsuzaki K. Evolution of grain boundary assemblies in Fe–0.6%O under mechanical milling followed by consolidating rolling. *Scripta Mater* 2003;48:1111–6.
- [192] Arzaghí M, Fundenberger JJ, Toth LS, Arruffat R, Faure L, Beausir B, et al. Microstructure, texture and mechanical properties of aluminum processed by high-pressure tube twisting. *Acta Mater* 2012;60:4393–408.
- [193] Belyakov A, Kimura Y, Adachi Y, Tsuzaki K. Microstructure evolution in ferritic stainless steels during large strain deformation. *Mater Trans* 2004;45:2812–21.
- [194] Valiev RZ, Korznikov AV, Mulyukov RR. Structure and properties of ultrafine-grained materials produced by severe plastic deformation. *Mater Sci Eng A* 1993;A168:141–8.
- [195] Belyakov A, Sakai T, Miura H, Kaibyshev R. Strain-induced submicrocrystalline grains developed in austenitic stainless steel under severe warm deformation. *Philos Mag Lett* 2000;80:711–8.
- [196] Kobayashi C, Sakai T, Belyakov A, Miura H. Ultrafine grain development in copper during multidirectional forging at 195 K. *Philos Mag Lett* 2007;87:751–66.
- [197] Rosen GJ, Juul Jensen D, Hughes DA, Hansen N. Microstructure and local crystallography of cold rolled aluminium. *Acta Metall Mater* 1995;43:2563–79.
- [198] Hurley PJ, Humphreys FJ. The application of EBSD to the study of substructural development in a cold rolled single-phase aluminium alloy. *Acta Mater* 2003;51:1087–102.
- [199] Morikawa T, Higashida K, Sato T. Fine-grained structures developed along grain boundaries in a cold-rolled austenitic stainless steel. *ISIJ Int* 2002;42:1527–33.

- [200] Miura H, Nakao H, Sakai T. Enhanced grain refinement induced by deformation twinning during multi-directional forging of Cu and Cu–Zn alloy. *Trans Mater* 2007;48:2539–41.
- [201] Belyakov A, Sakai T, Miura H, Kaibyshev R, Tsuzaki K. Continuous recrystallization in austenitic stainless steel after large strain deformation. *Acta Mater* 2002;50:1547–57.
- [202] Sakai T, Belyakov A, Miura H. Ultrafine grain formation in ferritic stainless steel during severe plastic deformation. *Metall Mater Trans A* 2008;39A:2206–14.
- [203] Meyers MA, Chawla KK. *Mechanical behavior of materials*. New York: Cambridge University Press; 2009.
- [204] Belyakov A, Sakai T, Miura H. Fine-grained structure formation in austenitic stainless steel under multiple deformation at 0.5 Tm. *Mater Trans, JIM* 2000;41:476–84.
- [205] Sitdikov O, Sakai T, Goloborodko A, Miura H, Kaibyshev R. Grain refinement in coarse-grained 7475 Al alloy during severe hot forging. *Philos Mag* 2005;85:1159–75.
- [206] Higashida K, Takamura J, Narita N. The formation of deformation bands in f.c.c crystals. *Mater Sci Eng* 1986;81:239–58.
- [207] Xing J, Yang X, Miura H, Sakai T. Mechanical properties of magnesium alloy AZ31 after severe plastic deformation. *Mater Trans* 2008;49:69–75.
- [208] Miura H, Yu G, Yang X, Sakai T. Microstructure and mechanical properties of AZ61 Mg alloy prepared by multi directional forging. *Trans Nonferrous Met Soc China* 2010;20:1294–8.
- [209] Yang X, Miura H, Sakai T. Effect of initial grain size and strain path on grain refinement in magnesium alloy AZ31. *Mater Sci Forum* 2007;539–543:1632–7.
- [210] Sakai T, Miura H. Mechanical properties of fine-grained magnesium alloys processed by severe plastic forging. In: Czerwinski F, editor. *Magnesium alloys – design, processing and properties*. Rijeka (Croatia): InTech; 2011. p. 219–44.
- [211] Kaibyshev OA. *Superplasticity of alloys, intermetallics and ceramics*. Berlin: Springer; 1992.
- [212] Sakai T, Yang X, Miura H. Dynamic evolution of fine grained structure and superplasticity of 7075 aluminum alloy. *Mater Sci Eng A* 1997;234–236:857–60.
- [213] Yang X, Miura H, Sakai T. Continuous dynamic recrystallization in a superplastic 7075 aluminum alloy. *Mater Trans* 2002;43:2400–7.
- [214] Blum W, Zhu Q, Markel R, McQueen HJ. Geometric dynamic recrystallization in hot torsion of Al–5Mg–0.6Mn (AA5083). *Mater Sci Eng A* 1996;A205:23–30.
- [215] Hughes DA, Hansen N. High angle boundaries formed by grain subdivision mechanism. *Acta Mater* 1997;45:3871–86.
- [216] Romanov AE, Vladimirov VI. Disclinations in crystalline solids. In: Nabarro FRN, editor. *Dislocations in solids*, vol. 9. Elsevier; 1992. p. 191–402.
- [217] Rybin VV, Zisman AA, Zolotarevsky NY. Junction disclinations in plastically deformed crystals. *Acta Mater* 1993;41:2211–7.
- [218] Zehetbauer M. Cold work hardening in stages IV and V of f.c.c. metals – II. Model fits and physical results. *Acta Mater* 1993;41:589–99.
- [219] Les P, Zehetbauer M. Evolution of microstructural parameters in large strain deformation: description by Zehetbauer's model. *Key Eng Mater* 1994;97–98:335–40.
- [220] Estrin Y, Toth LS, Molinari A, Brechet Y. A dislocation-based model for all hardening stages in large strain deformation. *Acta Mater* 1998;46:5509–22.
- [221] Toth LS, Molinari A, Estrin Y. Strain hardening at large strains as predicted by dislocation based polycrystal plasticity model. *J Eng Mater Technol* 2002;124:71–7.
- [222] Bouaziz O, Estrin Y, Brechet Y, Embury JD. Critical grain size for dislocation storage and consequences for strain hardening of nanocrystalline materials. *Scripta Mater* 2010;63:477–9.
- [223] Estrin Y, Vinogradov A. Extreme grain refinement by severe plastic deformation: a wealth of challenging science. *Acta Mater* 2013;61:782–817.
- [224] Mughrabi H. Dislocation wall and cell structures and long-range internal stresses in deformed metal crystals. *Acta Mater* 1983;31:1367–79.
- [225] Toth LS, Estrin Y, Lapovok R, Gu C. A model of grain fragmentation based on lattice curvature. *Acta Mater* 2010;58:1782–94.
- [226] Mazurina I, Sakai T, Miura H, Sitdikov O, Kaibyshev R. Grain refinement in aluminum alloy 2219 during ECAP at 250 °C. *Mater Sci Eng A* 2008;473:297–305.
- [227] Toth LS, Beausir B, Gu CF, Estrin Y, Scheerbaum N, Davies CHJ. Effect of grain refinement by severe plastic deformation on the next neighbor misorientation distribution. *Acta Mater* 2010;58:6706–16.
- [228] Arzt E. Size effects in materials due to microstructural and dimensional constraints: a comparative review. *Acta Mater* 1998;46:5611–26.
- [229] Dudova N, Belyakov A, Sakai T, Kaibyshev R. Dynamic recrystallization mechanisms operating in a Ni–20%Cr alloy under hot-to-warm working. *Acta Mater* 2010;58:3624–32.
- [230] Beladi H, Cizek P, Hodgson PD. Dynamic recrystallization of austenite in Ni-30 Pct Fe model alloy: microstructure and texture evolution. *Metall Mater Trans A* 2009;40A:1175–89.
- [231] Mazurina I, Sakai T, Miura H, Sitdikov O, Kaibyshev R. Partial grain refinement in Al–3%Cu alloy during hot ECAP. *Mater Trans* 2009;50:101–10.
- [232] Sakai T, Miura H. Ultrafine grain formation in aluminum alloys during hot severe plastic deformation. *Mater Sci Forum* 2012;706–709:1829–34.
- [233] Duckham A, Knutsen RD, Engler O. Influence of deformation variables on the formation of copper-type shear bands in Al–1Mg. *Acta Mater* 2001;49:2739–49.
- [234] Sitdikov O, Avtokratova E, Sakai T, Tsuzaki K. Ultra fine-grain structure formation in an Al–Mg–Sc alloy during warm ECAP. *Metall Mater Trans A* 2013;44A:1087–100.
- [235] Sakai T, Miura H, Goloborodko A, Sitdikov O. Continuous dynamic recrystallization during the transient severe deformation of aluminum alloy 7475 at high temperature. *Acta Mater* 2009;57:153–62.
- [236] Sakai T, Nagao Y, Ohashi M, Jonas JJ. Flow stress and structural change during the transient dynamic recrystallization of nickel. *Mater Sci Technol* 1986;2:659–65.

- [237] Watanabe H, Tsutsui H, Mukai T, Ishikawa K, Okanda Y, Kohzu M, et al. Grain size control of commercial wrought Mg–Al–Zn alloys utilizing dynamic recrystallization. *Mater Trans* 2001;42:1200–5.
- [238] Valiev RZ, Alexandrov IV, Zhu YT, Lowe TC. Paradox of strength and ductility in metals processed by severe plastic deformation. *J Mater Res* 2002;17:5–8.
- [239] Salichshev GA, Galeev RM, Valiakhmetov OA, Zharebtsov SV, Mironov SYu, Malysheva SP, et al. Submicrocrystalline titanium and titanium alloys: structure and mechanical properties. In: Gorynin IV, Ushkov SS, editors. *Proc int conf titanium'99 science and technology*. S-Peterburg (Russia): Central Research Institute of Structural Materials; 1999. p. 651–8.
- [240] Zharebtsov SV, Salishchev GA, Galeev R.M. Formation of submicrocrystalline structure in titanium and its alloy under severe plastic deformation. *Defect Diffus Forum* 2002;208-209:237–40.
- [241] Zharebtsov S, Salishchev G, Galeev R, Maekawa K. Mechanical properties of Ti–6Al–4V titanium alloy with submicrocrystalline structure produced by severe plastic deformation. *Mater Trans* 2005;46:2020–5.
- [242] Salichshev GA, Galeev RM, Malysheva SP, Zharebtsov SV, Mironov SYu, Valiakhmetov OA, et al. Formation of submicrocrystalline structure in titanium and titanium alloys and their mechanical properties. *Met Sci Heat Treat* 2006;48:63–9.
- [243] Zharebtsov S, Kudryavtsev E, Kostjuchenko S, Malysheva S, Salishchev G. Strength and ductility-related properties of ultrafine grained two-phase titanium alloy produced by warm multiaxial forging. *Mater Sci Eng A* 2012;536:190–6.
- [244] Gholinia A, Prangnell PB, Markushev MV. The effect of strain path on the development of deformation structures in severely deformed aluminium alloys processed by ECAE. *Acta Mater* 2000;48:1115–30.
- [245] Horita Z, Fujinami T, Nemoto M, Langdon TG. Equal-channel angular pressing of commercial aluminum alloys: grain refinement, thermal stability and tensile properties. *Metall Mater Trans A* 2000;31A:691–701.
- [246] Langdon TG, Furukawa M, Nemoto M, Horita Z. Using equal-channel angular pressing for refining grain size. *JOM* 2000;52:30–3.
- [247] Hayes JS, Keyte R, Prangnell PB. Effect of grain size on tensile behavior of a submicron grained Al–3wt-%Mg alloy produced by severe deformation. *Mater Sci Technol* 2000;16:1259–63.
- [248] Kaibyshev R, Mogucheva A. Effect of ECAP on mechanical properties of an AA2014 alloy. *Mater Sci Forum* 2011;667–669:931–6.
- [249] Mogucheva A, Kaibyshev R. Effect of ECAP on microstructure and mechanical properties of an Al–Mg–Sc alloy. *Mater Sci Forum* 2011;667–669:949–54.
- [250] Kaibyshev R, Mogucheva A, Dubina A. Strategy for achieving high strength in Al–Mg–Sc alloys by intense plastic straining. *Mater Sci Forum* 2012;706–709:55–60.
- [251] Mogucheva A, Zyabkin D, Kaibyshev R. Effect of the thermomechanical processing on microstructure and properties of an Al–Ce alloy. *Mater Sci Forum* 2012;706–709:361–6.
- [252] Kamamichi M, Furukawa M, Horita Z, Langdon TG. Equal-channel angular pressing using plate samples. *Mater Sci Eng A* 2003;A361:258–66.
- [253] Raab GJ, Valiev RZ, Lowe TC, Zhu YT. Continuous processing of ultrafine grained Al by ECAP–Conform. *Mater Sci Eng A* 2004;A382:30–4.
- [254] Nikulin I, Kaibyshev R, Sakai T. Superplasticity in a 7075 aluminum alloy processed by ECAE and subsequent isothermal rolling. *Mater Sci Eng A* 2005;A407:62–70.
- [255] Etherington C. Conform and the recycling of non-ferrous scrap metals. *Conserv Recycling* 1978;2:19–29.
- [256] Belyakov A, Kimura Y, Tsuzaki K. Microstructure evolution in dual phase stainless steel during severe deformation. *Acta Mater* 2006;54:2521–32.
- [257] Zharebtsov SV, Dyakonov GS, Salem AA, Malysheva SP, Salishchev GA, Semiatin SL. *Mater Sci Eng A* 2011;A528:3474–9.
- [258] Belyakov A, Tsuzaki K, Kaibyshev R. Nanostructure evolution in an austenitic stainless steel subjected to multiple forging at ambient temperature. *Mater Sci Forum* 2011;667–669:553–8.
- [259] Shakhova I, Dudko V, Belyakov A, Tsuzaki K, Kaibyshev R. Effect of large strain cold rolling and subsequent annealing on microstructure and mechanical properties of an austenitic stainless steel. *Mater Sci Eng A* 2012;A545:176–86.
- [260] Nakao Y, Miura H. Nano-grain evolution in austenitic stainless steel during multi-directional forging. *Mater Sci Eng A* 2010;A528:1310–7.
- [261] Tikhonova M, Kuzminova Y, Belyakov A, Kaibyshev R. Nanocrystalline S304H austenitic stainless steel processed by multiple forging. *Rev Adv Mater Sci* 2012;31:68–73.
- [262] Shakhova I, Belyakov A, Kaibyshev R, Kimura Y, Tsuzaki K. Submicrocrystalline structures and tensile behaviour of stainless steels subjected to large strain deformation and subsequent annealing. *Adv Mater Res* 2012;409:607–12.
- [263] Belyakov A, Tsuzaki K, Kimura Y, Mishima Y. Tensile behaviour of submicrocrystalline ferritic steel processed by large-strain deformation. *Philos Mag Lett* 2009;89:201–12.
- [264] Chen L, Yuan FP, Jiang P, Wu XL. Mechanical properties and nanostructures in a duplex stainless steel subjected to equal channel angular pressing. *Mater Sci Eng A* 2012;A551:154–9.
- [265] Yang X, Miura H, Sakai T. Evolution of fine grained microstructure and superplasticity in warm-worked 7075 aluminum alloy. *Mater Trans JIM* 1996;37:1379–87.
- [266] Mogucheva A, Tagirova D, Kaibyshev R. Superplasticity in a 5024 aluminium alloy processed by severe plastic deformation. *Mater Sci Forum* 2013;735:353–8.
- [267] Kaibyshev R, Zhemchuzhnikova D, Mogucheva A. Effect of Mg content on high strain rate superplasticity of Al–Mg–Sc–Zr alloys subjected to equal-channel angular pressing. *Mater Sci Forum* 2013;735:265–70.
- [268] Kaibyshev R, Tagirov D, Mogucheva A. Cost-affordable technique involving equal channel angular pressing for the manufacturing of ultrafine grained sheets of an Al–Li–Mg–Sc alloy. *Adv Eng Mater* 2010;12:735–9.
- [269] Shagiev M, Motohashi Y, Musin F, Kaibyshev R, Itoh G. Superplastic response of an advanced Al–Li–Mg–Cu–Sc alloy subjected to intense plastic deformation. *Mater Trans* 2003;44:1698–701.
- [270] Vinogradov A, Ishida T, Kitagawa K, Kopylov VI. Effect of strain path on structure and mechanical behavior of ultrafine grain Cu–Cr alloy produced by equal-channel angular pressing. *Acta Mater* 2005;53:2181–92.

- [271] Xu CZ, Wang QJ, Zheng MS, Zhu JW, Li JD, Huang MQ, et al. Microstructure and properties of ultra-fine grain Cu–Cr alloy prepared by equal-channel angular pressing. *Mater Sci Eng A* 2007;A459:303–8.
- [272] Dobatkin SV, Terent'ev VF, Skrotzki W, Rybalchenko OV, Pankova MN, Prosvirin DV, et al. Structure and fatigue properties of 08Kh18N10T steel after equal-channel angular pressing and heating. *Russ Metall (Metally)* 2012;2012:954–62.
- [273] Stolyarov VV, Valiev RZ, Zhu YT. Enhanced low-temperature impact toughness of nanostructured Ti. *Appl Phys Lett* 2006;88. art.No.041905.
- [274] Kimura Y, Inoue T, Yin F, Tszuzaki K. Inverse temperature dependence of toughness in an ultrafine grain-structure steel. *Science* 2008;320:1057–60.
- [275] Divinski SV, Wilde G, Rabkin E, Estrin Y. Ultra-fast atomic transport in severely deformed materials – a pathway to applications? *Adv Eng Mater* 2010;12:779–85.
- [276] Divinski SV, Reglitz G, Rosner H, Estrin Y, Wilde G. Ultra-fast diffusion channels in pure Ni severely deformed by equal-channel angular pressing. *Acta Mater* 2011;59:1974–85.
- [277] Ferkel H, Glatzer M, Estrin Y, Valiev RZ. RF plasma nitriding of a severely deformed high alloyed steel. *Scripta Mater* 2002;46:623–8.
- [278] Salishchev G, Zherebtsov S, Malysheva S, Smyslov A, Saphin E, Izmaylova N. Mechanical properties of Ti–6Al–4V titanium alloy with submicrocrystalline structure produced by multiaxial forging. *Mater Sci Forum* 2008;584–586:783–8.
- [279] Takayama A, Yang X, Miura H, Sakai T. Continuous static recrystallization of ultrafine grained copper processed by multi-directional forging. *Mater Sci Eng A* 2008;478:221–8.
- [280] Humphreys FJ. A unified theory of recovery, recrystallization and grain growth of cellular microstructures-1. The basic model. *Acta Mater* 1997;45:4231–40.
- [281] Gertsman VY, Birringer R, Valiev RZ, Gleiter H. On the structure and strength of ultrafine-grained copper produced by severe plastic deformation. *Scripta Mater* 1994;30:229–34.
- [282] Yang X, Zhu Y, Miura H, Sakai T. Static recrystallization behavior of hot-deformed magnesium alloy AZ31 during isothermal annealing. *Trans Nonferrous Met Soc China* 2010;20:1269–74.
- [283] Yang X, Miura H, Sakai T. Isochronal annealing behavior of magnesium alloy AZ31 after hot deformation. *Mater Trans* 2005;46:2981–7.
- [284] Korznikov A, Dimitrov O, Korznikova G. Thermal evolution of the structure of ultra fine grained materials produced by severe plastic deformation. *Ann Chim Sci Mater* 1996;21:443–60.
- [285] Jazaeri H, Humphreys FJ. The transition from discontinuous to continuous recrystallization in some aluminum alloys II – annealing behaviour. *Acta Mater* 2004;52:3251–62.
- [286] Sakai T, Xu Z. Kinetics of static grain growth in dynamically recrystallized copper polycrystals with different purities. *Mater Trans JIM* 1996;37:1422–30.
- [287] Xu Z, Sakai T. Kinetics of recovery and recrystallization in dynamically recrystallized austenite. *Mater Trans JIM* 1991;32:174–80.
- [288] Sakai T, Ohashi M, Chiba K, Jonas JJ. Recovery and recrystallization of polycrystalline nickel after hot working. *Acta Metall* 1988;36:1781–90.
- [289] Djaic RAP, Jonas JJ. Recrystallization of high-carbon steel between intervals of high-temperature deformation. *Metall Trans* 1973;4:621–4.
- [290] Petkovic RA, Luton MJ, Jonas JJ. Recovery and recrystallization of polycrystalline copper after hot working. *Acta Metall* 1979;27:1633–48.
- [291] Kato S, Mori A, Miura H, Sakai T. Ferrite refinement through transformation from a dynamically recrystallized IF steel. In: Palmiere EJ, Mahfoul M, Pinna C, editors. *Thermomechanical processing: mechanics, microstructure and control*. UK: The Univ. Sheffield; 2003. p. 17–21.